MEASUREMENT OF THE CP VIOLATION PARAMETER ETA$_{+-GAMMA}$

BY JOHN N. MATTHEWS

A dissertation submitted to the
Graduate School—New Brunswick
Rutgers, The State University of New Jersey
in partial fulfillment of the requirements
for the degree of
Doctor of Philosophy
Graduate Program in Physics and Astronomy
Written under the direction of
Gordon B. Thomson
and approved by

Gordon B. Thomson
Theodore B. Williams
A. Seiberg
Thomas J. Devlin
Peter Steinberg

New Brunswick, New Jersey
January, 1996

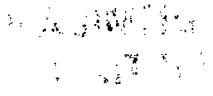

ABSTRACT OF THE D

Measurement of the CP Vi

Eta$_{+-gamma}$

by John N. Matth

Dissertation Director: Gordon

This dissertation describes the measurement of t
$\eta_{+-\gamma}$ in a neutral kaon experiment, E773, at Fer
characterizes CP violation in the decay $K_L \rightarrow$
$\pi^+\pi^-$ collected simultaneously were used for no
$|\eta_{+-\gamma}| = (2.359 \pm 0.062_{stat} \pm 0.040_{sys}) \times 10^{-3}$ wit
$3.5_{stat} \pm 1.9_{sys})°$. The prediction that $\eta_{+-\gamma}$ shoul
supported by this result.

Acknowledgements

I would like to begin by thanking my advisor, Gordon Thomson, for introducing me to the intricacies of CP Violation and problem solving in an experimental analysis. I would like to thank him, too for the abundance of advice and support which he gave me throughout my years at Rutgers. I have enjoyed working with him and have benefited much from our discussions about physics and beyond.

I am deeply indebted to all of my E773/E799 collaborators who contributed to the work presented in this thesis. Their hard work made this analysis possible. In particular, I would like to thank Erik Ramberg for sharing his insight into $\pi\pi\gamma$ decays, living life, and hunting mushrooms. Bill Hogan and Pete Haas were not only members of the core group working on E773, but also provided the necessary diversions such as the occasional Sox game or fish & cider. The dollars we bet will always bring back many memories (somehow, many of Frank). While busy working on their own analyses, Bernhard Schwingenheuer and Roy Briere were the friendly faces answering questions and pointing out potential mines. Sunil Somalwar (who has been there from monopole days), Taku Yamanaka, Bob Tschirhart, and Bob Hsiung were driving forces behind the experiment and answered many detailed questions about it. Kevin McFarland also provided me with several figures which are in this document.

I would also like to thank: Henry Frisch, Albert Erwin, and Joe Incandela who gave me my start in experimental high energy physics and showed me what great fun it was. Steve Schnetzer, Tom Devlin, and Dick Plano who provided assistance above and beyond the call of duty especially at the beginning and end of my graduate tenure. Yau Wai Wah for his continual support and advice (and skiing) and Bruce Winstein for pushing as needed and lending advice freely.

I would like to thank my friends who assisted me in the journey from "there to here" and made it enjoyable too.... Especially, Theo Alexopoulos, Kavoos Deilamain, Mark Lomperski, Lingwei Guan, Ping Gu, Jodi Lamoureux, Tsuyoshi Nakaya, and Eric Collins. Special thanks are due to Yu Zou and family for bringing me into their family on my many trips back to Jersey.

Most of all, I would like to thank my family for the support, encouragement, and patience they have given me throughout my years as a student (which as my wife, Teresa, points out - have been many).

The FNAL E773 Collaboration

- Rutgers University
  - J.N. Matthews, P. Gu, P. Haas, W.P. Hogan, S.K. Kim, S.S. Myung, S. Schnetzer, S.V. Somalwar, G.B. Thomson, Y. Zou
- The University of Chicago
  - A.R. Barker, R.A. Briere, E. Cheu, D.A. Harris, G. Makoff, K.S. McFarland, A. Roodman, B. Schwingenheuer, Y.W. Wah, B. Winstein, R. Winston
- Elmhurst College
  - E.C. Swallow
- Fermilab
  - G.J. Bock, R. Coleman, M. Crisler, J. Enagonio, R. Ford, Y.B. Hsiung, D.A. Jensen, E. Ramberg, R. Tschirhart, T. Yamanaka
- The University of Illinois
  - E.M. Collins, G.D. Gollin

Dedication

To my parents, John and Lois Matthews, and my wife, Teresa,
for all of their love and support.

Table of Contents

List of Tables

List of Figures

Chapter 1

Introduction

1.1 History

In 1964 CP violation was discovered in the $\pi^+\pi^-$ decay of the long lived neutral kaon [1] prompting a broad search for other manifestations of the phenomenon. Within a few years a second CP-violating decay ($K_L \to \pi^0\pi^0$) was identified as was a CP-violating charge asymmetry in the $K_L \to \pi e\nu$, and $\pi\mu\nu$ decays. [2, 3, 4] Although detailed investigations were pursued, no further CP violation was observed for over a quarter century.

In 1993, Fermilab experiment 731 observed interference between the K_S and K_L amplitudes in the $K \to \pi^+\pi^-\gamma$ decay. [5] Such interference is the result of mixing between the states and a clear demonstration of CP violation. In the intervening years, the parameters associated with the CP violation in the other modes have been measured to great accuracy. [6, 7] However, the first (and so far only) measurement of the CP violation parameter associated with the $\pi^+\pi^-\gamma$ decay, $\eta_{+-\gamma}$, resulted in only a coarse measurement. Here, we report on a new, more precise measurement.

Year	Decay Mode	CP Parameter
1964	$K \to \pi^+\pi^-$	η_{+-}
1966/7	$K \to \pi^0\pi^0$	η_{00}
1967	$K \to \pi e\nu,\ \pi\mu\nu$	δ_l
1993	$K \to \pi^+\pi^-\gamma$	$\eta_{+-\gamma}$

Table 1.1: History of the discovery of CP Violation

1.2 CP Violation

The production eigenstates of the neutral kaon are the strong eigenstates, K^0 and $\overline{K^0}$. However, kaons decay via the weak force and the weak eigenstates are not the same as the strong eigenstates; they are essentially eigenstates of CP, not strangeness, S. The CP eigenstates are linear combinations of the strong eigenstates:

$$|K_1\rangle = \frac{1}{\sqrt{2}}\left(|K^0\rangle + |\overline{K^0}\rangle\right), \qquad CP = +1,$$

$$|K_2\rangle = \frac{1}{\sqrt{2}}\left(|K^0\rangle - |\overline{K^0}\rangle\right), \qquad CP = -1. \tag{1.1}$$

K_1 and K_2 are distinguished by their mode of decay; the short lived K_1 decays to the 2π CP even state, while the long lived K_2 goes to the 3π CP odd state.

When Cronin, Fitch, *et al.* discovered CP violation through the observation of the $\pi^+\pi^-$ decay of the long lived kaon, this was explained by describing the states with a small amount of mixing between them (i.e. via $\Delta S = 2$ transitions like $K^0 \leftrightarrow \pi^+\pi^- \leftrightarrow \overline{K^0}$). The nomenclature to reflect

this names the kaons by their lifetimes, K_S and K_L, for the short and long lived components. The complex parameter ϵ describes the amount of CP violation due to mixing, so that

$$|K_S\rangle = |K_1\rangle + \epsilon\,|K_2\rangle\,,$$

$$|K_L\rangle = |K_2\rangle + \epsilon\,|K_1\rangle\,. \tag{1.2}$$

This CP violation occurs before the decay and hence ϵ must be independent of the decay mode.

Any CP violation not due to mixing, direct CP violation, is represented in the complex parameter ϵ'. Using isospin, the decay amplitudes are written

$$\left\langle I=0|T|K^0\right\rangle = e^{i\delta_0}A_0 \tag{1.3}$$

$$\left\langle I=2|T|K^0\right\rangle = e^{i\delta_2}A_2 \tag{1.4}$$

where δ_I are the $\pi\pi$ final state phase shifts and I is the isospin of the final state (the $I=1$ state is forbidden by the Bose symmetry of the system). CP violation is measured by $\mathrm{Im}(A_I)/\mathrm{Re}(A_I)$ and

$$\epsilon' = \frac{i}{2}e^{i(\delta_2-\delta_0)}\frac{\mathrm{Re}(A_2)}{\mathrm{Re}(A_0)}\left[\frac{\mathrm{Im}(A_2)}{\mathrm{Re}(A_2)} - \frac{\mathrm{Im}(A_0)}{\mathrm{Re}(A_0)}\right]. \tag{1.5}$$

The physical observables are independent of the choice of phase and the standard phase convention due to Wu and Yang is to choose A_0 to be real. [8] This results in

$$\epsilon' = \frac{i}{2}e^{i(\delta_2-\delta_0)}\frac{\mathrm{Im}(A_2)}{A_0}, \tag{1.6}$$

which has a phase of

$$\phi(\epsilon') = \delta_2 - \delta_0 + \frac{\pi}{2}. \tag{1.7}$$

Measurements of the $\pi\pi$ final state phase shifts by other experiments [9] have shown that ϵ' and ϵ are almost parallel. A non-zero value of ϵ' is definite evidence for CP violation in the decay amplitude.

The total measure of CP violation in the $\pi^+\pi^-$ decay mode is then described by the ratio of the CP-violating K_L decay to 2π to the CP-conserving K_S decay:

$$\eta_{+-} = |\eta_{+-}|\, e^{i\phi_{+-}} = \frac{\mathrm{Ampl}(K_L \to \pi^+\pi^-)}{\mathrm{Ampl}(K_S \to \pi^+\pi^-)} = \epsilon + \epsilon'_{+-}. \tag{1.8}$$

Meanwhile, in the $\pi^0\pi^0$ decay mode, the result is

$$\eta_{00} = \epsilon - 2\epsilon'_{00} \tag{1.9}$$

due to the different isospin states of that decay.

An arbitrary mixture of K_S and K_L will develop as a function of proper time, τ, as

$$|\psi(\tau)\rangle = a_S e^{-(1/2\tau_S + im_S)\tau} \cdot |K_S\rangle + a_L e^{-(1/2\tau_L + im_L)\tau} \cdot |K_L\rangle, \tag{1.10}$$

where $a_{S(L)}$, $\tau_{S(L)}$, and $m_{S(L)}$ are the initial amplitude, lifetime, and mass of the $K_{S(L)}$. When both the K_S and K_L decay into the same final state, one may observe interference effects between their decay amplitudes into the final state signal:

$$\begin{aligned} \langle\psi_f|T|\psi(\tau)\rangle &= a_S e^{-(1/2\tau_S + im_S)\tau}\langle\psi_f|T|K_S\rangle + a_L e^{-(1/2\tau_L + im_L)\tau}\langle\psi_f|T|K_L\rangle \\ &= \langle\psi_f|T|K_S\rangle\{a_S \cdot e^{-(1/2\tau_S + im_S)\tau} + \eta \cdot a_L e^{-(1/2\tau_L + im_L)\tau}\} \end{aligned} \tag{1.11}$$

The observed decay rate is then proportional to

$$R(\tau) \propto |a_S|^2 e^{-\tau/\tau_S} + |\eta \cdot a_L|^2 e^{-\tau/\tau_L} + 2|a_S||\eta \cdot a_L| \cos(\Delta m \tau + \phi) e^{-\tau/2(1/\tau_S + 1/\tau_L)}, \quad (1.12)$$

where $\phi = \arg(a_S) - \arg(\eta \cdot a_L)$, and $\Delta m = m_{K_L} - m_{K_S}$. is the decay rate of the $K_{S(L)}$. It is possible to measure the magnitude of η simply from the ratio of the branching ratios, B, and lifetimes, τ: [10]

$$|\eta| = \left[\frac{B(K_L)}{\tau(K_L)} \cdot \frac{\tau(K_S)}{B(K_S)}\right]^{1/2}. \quad (1.13)$$

However, by studying the interference pattern, it is possible to measure not only the amplitude, but also the phase of η.

1.3 Regeneration

In this experiment, Fermilab experiment 773 (FNAL E773), we used the phenomenon of coherent regeneration to study the interference between the K_S and K_L amplitudes. As a pure K_L beam traverses a slab of material, the K^0 and $\overline{K^0}$ amplitudes are absorbed differently. The $\overline{K^0}$ components have more channels to interact (e.g. $\overline{K^0}p \rightarrow \Lambda\pi^+$) and therefore the $\overline{K^0}$ has a greater total cross-section than the K^0. Since the $\overline{K^0}$ is more strongly absorbed, the ratio of K^0 to $\overline{K^0}$ is altered, resulting in the regeneration of a small amount of K_S. This regeneration is described by the complex parameter ρ.

The optical theorem relates the total cross-section, σ_T, to the forward scattering amplitude, $f(0)$, by Im $f(0) = (k/4\pi)\sigma_T$, where $k = p/\hbar$ is the

wave number of the kaon. Therefore, at any given momentum $|\mathrm{Im}\ \bar{f}(0)| > |\mathrm{Im}\ f(0)|$ where $\bar{f}$ designates the $\overline{K^0}$ scattering amplitude. The state emerging from the slab is described by

$$|\psi_f(\theta)\rangle = \frac{f(\theta) - \bar{f}(\theta)}{2}|K_S\rangle + \frac{f(\theta) + \bar{f}(\theta)}{2}|K_L\rangle\,. \tag{1.14}$$

In particular, in the forward direction ($\theta = 0$) the amplitude of K_S regenerated by one scattering center is proportional to $f(0) - \bar{f}(0)$.

If one considers two scattering centers, these two centers will act coherently if $d(p_S \cos\theta - p_L) \ll 1$, where $p_{S(L)}$ is the momentum of the $K_{S(L)}$. [11] Here d is the distance of the two scattering centers along the K_L direction, and θ is the scattering angle between the incoming K_L and the outgoing K_S. The coherence length is of the order of several K_S mean decay lengths and the momentum transfer of the order of 10^{-6} eV/c. [11, 12, 13, 14] This gives rise to different classes of regeneration:

1. Coherent Regeneration or "transmission regeneration" is the consequence of the coherent addition of amplitudes from an extended region. In the coherent process, $K_L X \rightarrow K_S X$, the K_S is produced along the direction of the initial K_L. The regeneration amplitude for this process, ρ, is proportional to the difference in forward scattering amplitudes of the K^0 and $\overline{K^0}$.

2. Diffractive Regeneration (elastic scattering) results when there is scattering from nuclei which causes the recoil of a nucleus. The K_S is thus regenerated at a finite angle with respect to the initial K_L. The effect

is coherent action of the nucleons within the nucleus, but incoherent addition of intensities from different nuclei.

3. Inelastic Regeneration (inelastic scattering) occurs when the momentum transfers are so big as to break up the nucleus or to transfer it to an excited state.

In the measurement of CP violation parameters, only the coherent regeneration is used as signal. The diffractive and inelastic regeneration components are treated as background since they have lost the phase information in their collisions. By examining the transverse momentum imparted to the kaon in the regenerator and searching for signs of nuclear breakup it is possible to select a coherent mixture of K_L and K_S for study of the interference effects between the CP-conserving and CP-violating components of the decay.

The connection between the "elementary" scattering amplitude $f(\theta) - \bar{f}(\theta)$ and the macroscopic observed regeneration probability for the coherent regeneration can be expressed as:

$$|\psi_f\rangle \propto |K_L\rangle + \rho(L)\,|K_S\rangle\,. \tag{1.15}$$

The expression for ρ contains two factors, a nuclear part and a geometric part depending on the length, L, of the regenerator:

$$\rho = i\pi NL\left(\frac{f-\bar{f}}{k}\right)\delta(L) \tag{1.16}$$

where

$$\delta(L) = \frac{1-\exp(-i(z_S - z_L)l)}{i(z_S - z_L)l)}.$$

Here, N is the number density of its scatterers, $l = L/(\beta\gamma)$, and $z_{S(L)} = m_{S(L)} - \frac{i}{2}\Gamma_{S(L)}$. $\Gamma_{S(L)} = 1/\tau_{S(L)}$ and β and γ are the usual Lorentz factors. A power law may be used to describe the quantity $(f - \bar{f})/k$

$$\left|\frac{f-\bar{f}}{k}\right| = 2.23A^{0.758}(p[GeV])^{-\alpha} \text{ mb} \tag{1.17}$$

$$arg\left(\frac{f-\bar{f}}{k}\right) = -\frac{\pi}{2}(2+\alpha) \simeq -125°. \tag{1.18}$$

[15, 16, 17] Equation 1.18 is known as the "analyticity condition". Note that both the magnitude and phase of ρ are momentum dependant.

1.4 Kaons and $\pi\pi\gamma$ Decay

There are two processes which contribute to the $\pi^+\pi^-\gamma$ decay amplitude: Inner Bremsstrahlung and Direct Emission. The K_S decay is dominated by the Inner-Bremsstrahlung (IB) process [18] in which a charged pion from a $K \to \pi^+\pi^-$ (Kπ2) decay radiates a photon. However, for K_L decays, the IB rate is suppressed due to the fact the Kπ2 decay mode is CP violating. This permits the CP conserving Direct Emission (DE) process to be significant. In the DE case, the photon originates in the primary decay vertex and is emitted before the hadronization of the pions. Previous experiments have found that the spectrum of photon energies in the kaon center of mass frame fits an electric dipole (E1) form for the IB term and a magnetic dipole (M1) form, modified for the effects of vector meson intermediaries, for the DE term [18, 19, 20]. The fact that the IB and DE components have different photon energy spectra allows one to determine the ratio of their contribution

to the K_L decay rate: r = (DE rate)/(IB rate) [19, 20, 21, 22]. Finally, we note that the E1 term for the K_S (K_L) is CP conserving (violating) and the modified M1 term for the K_L is CP conserving as well.

Since the terms in the multipole expansion of each decay amplitude are orthogonal, interference between K_S and K_L will occur only for like-term multipoles. The principle contribution to the interference comes from the two IB E1 decays, however higher-order multipoles contribute if present. Although direct CP violation is expected to be small, it could present itself through a DE E1 transition of the K_L interfering with the IB E1 transition of the K_S. Therefore, what one measures is the ratio of decay amplitudes:

$$\eta_{+-\gamma} = \frac{A(K_L \to \pi^+\pi^-\gamma,\ \text{CP Violating})}{A(K_S \to \pi^+\pi^-\gamma)} = \epsilon + \epsilon'_{+-\gamma}. \tag{1.19}$$

The CP-conserving M1 DE contribution, which does not interfere, shows up in Equation. 1.12 as an "extra term" of $r \cdot |\eta \cdot a_L|^2 e^{-\tau/\tau_L}$. The number of observed $\pi^+\pi^-\gamma$ decays per unit proper time observed downstream of the regenerator is then:

$$\begin{aligned}\frac{dN}{d\tau} &= \frac{N_S B_{+-\gamma}}{\tau_S |\rho|^2} \cdot \Big[|\rho|^2 e^{-\tau/\tau_S} + |\eta_{+-\gamma}|^2 e^{-\tau/\tau_L} \cdot (1+r) \\ &\quad + 2|\rho| \cdot |\eta_{+-\gamma}| \cos(\Delta m\tau + \phi_\rho - \phi_\eta) e^{-\frac{\tau}{2}(\frac{1}{\tau_S}+\frac{1}{\tau_L})}\Big],\end{aligned} \tag{1.20}$$

where N_S is the number of regenerated K_S and ϕ_ρ (ϕ_η) is the phase of ρ ($\eta_{+-\gamma}$).

One expects that the E1 IB would contribute a term of η_{+-} to $\eta_{+-\gamma}$. However, should CP be nonconserved in the Direct Emission (DE), for example through an E1 DE term then, there could be interference with the K_L

and K_S IB terms which would be demonstrated in a difference between η_{+-} and $\eta_{+-\gamma}$. [20] So far there exist only very rough estimates of the possible size of such an effect.

Donoghue, Holstein, and Valencia performed an order of magnitude estimate of $\epsilon'_{+-\gamma}$. Their calculation was based on higher order chiral Lagrangians and the fact that the ΔI = 3/2 suppression can be removed in this decay. They estimated that $\epsilon'_{+-\gamma}$ might be as large as $5\epsilon'_{+-}$. [32]

Lin and Valencia improved on the rough estimate of Donoghue *et al.* by constructing an explicit example of a higher order effective Lagrangian. [26] To maximize the effect, they looked at the highest center-of-mass photon energies. They estimated that the largest possible contribution to direct CP violation one could expect from this one term was $\epsilon'_{+-\gamma}/\epsilon \approx 0.02$. This is the result of just one of many possible terms which could be investigated. Therefore, although this estimate is based on more complete information, it is still a very rough calculation. However, there is some hope that a more complete calculation of this effect will be carried out in the near future. [27]

ϵ'_{+-} is small for two reasons. First, it suffers from the $\Delta I = 3/2$ suppression and second the two contributing penguin diagrams (the electro-weak and the gluon penguins) interfere destructively. $\epsilon'_{+-\gamma}$ is not plagued by these two suppression factors and could be considerably larger than ϵ'_{+-}. As a result of this enhancement, the $\pi\pi\gamma$ decay is an interesting place to examine CP violation for clues into its origin.

1.5 Experimental Status

The best previous measurement of the CP violation parameter $\eta_{+-\gamma}$ is still the coarse first measurement, made by E.J. Ramberg of the FNAL E731 collaboration in 1993. [5] E731 was a dual beam experiment with one pure K_L beam and one regenerator beam. The K_L beam was used to measure the $K_L \to \pi^+\pi^-\gamma$ DE and IB branching ratios, thereby determining r of equation 1.20. The regenerator beam was used for measuring the $K_S \to \pi^+\pi^-\gamma$ branching ratio and η. By fitting the distribution of decays downstream of the regenerator, $|\eta_{+-\gamma}|$ was measured to be $(2.15 \pm 0.26_{stat} \pm 0.20_{sys})\times 10^{-3}$, and $\phi_{+-\gamma}$ to be $(72 \pm 23_{stat} \pm 17_{sys})^\circ$.

Chapter 2

The Experimental Apparatus

2.1 The Principles of the Measurement

The magnitude and phase of $\eta_{+-\gamma}$ are obtained by investigating the coherent interference between the K_S and K_L decay amplitudes in the $\pi^+\pi^-\gamma$ decay mode of neutral kaons. This interference is measured by fitting the data to the hypothisis of Equation. 1.20. The first steps along the path to that goal are production of the kaons, the identification of the signal, and the separation of signal from background.

The accelerator delivers protons to the experimental area. These protons must be converted into a maximum number of neutral kaons with a minimum of other particles. The signal for this measurement consists of coherently regenerated K_S and transmitted K_L decays to $\pi^+\pi^-\gamma$. The background consists of scattered kaons decaying to $\pi^+\pi^-\gamma$ as well as non-$\pi\pi\gamma$ decays.

Each signal event is a decay containing two oppositely charged pions as well as a photon. The particles must come from a common vertex and reconstruct to a kaon. Particle identification is required to separate muons and electrons from pions. A tracking system is necessary in order to determine

the trajectories and momenta of the charged particles. An electro-magnetic calorimeter can be used both to measure the position and energy of the photon and to aid in particle identification.

In this chapter, we describe the beamline and detector in more detail.

2.1.1 The Coordinate System

The coordinate system for the experiment takes the target as the origin. The positive z-axis connects the target to the center of the lead glass array. x and y are perpendicular to the z-axis, in the horizontal and vertical directions respectively. Positive y was in the upward direction.

2.2 The Beam

Experiment 773 (E773) was performed at Fermi National Accelerator Laboratory (FNAL or Fermilab) in the Meson Center beamline. It employed a double beam technique similar to that of its predecessor, E731. The experiment had two short test runs in the summer of 1990. The data for this analysis was collected between mid-July and the end of September of 1991.

The accelerator provided 800 GeV protons on target, typically at a rate of 1.5 - 2 $\times$ 10^{12} per "spill" to the target. The experiment received about one spill per minute; each spill lasting 22 seconds. Within each spill, there was a 53 MHz bucket structure due to the accelerator RF. The protons were contained in a 2 ns "bucket" each 19 ns. Thus, a spill consisted of about 1.2 $\times$ 10^9 buckets of about 1,500 protons each. Our beams contain on the order

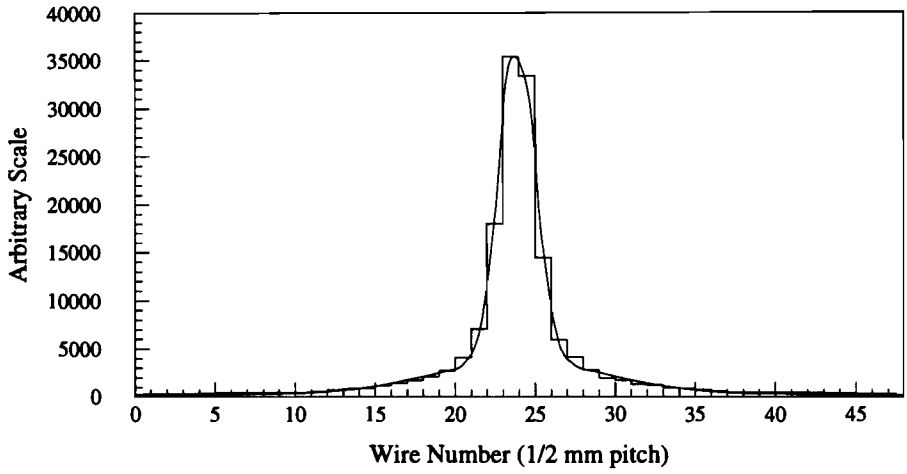

Figure 2.1: The beam profile on the target as measured by wire chambers just upstream of the target. The profile is a typical average over an hours worth of spills. The line through the histogram is a fit to the data which was incorporated into the Monte Carlo.

of one kaon, in our energy range of 20 - 160 GeV every 50 buckets.

The target was made of beryllium in the form of a rod 36 cm long and an eighth of an inch square. This rod was aligned with the proton beam and about twice its diameter. The beam position on the target was measured by two proportional wire chambers, one for each (x & y) view, with 1/2 mm pitch. In addition, the final steering dipole magnets were under experimenter control, thus allowing movement of the beam spot across the target. The sum of one chamber's scans over a typical set of spills is shown in figure 2.1.

The first step in defining the resulting secondary beams was made with

the use of a two hole collimator 9 m downstream from the target. The collimator was 5.8 meters of water-cooled copper and the holes were oriented at an angle of 4.8 milliradians in the horizontal from the direction of the proton beam. At the upstream end, the holes were 6.65 mm square and were separated vertically by 5.8 mm. The collimator was followed by two steel slabs at 24.8 m and 48.9 m which prevented beam crossover (events from one beam from scattering over into the other). Additional collimation was provided by separate sets of horizontal and vertical adjustable steel collimators at 52 m and 84 m downstream of the target.

The composition of the beam was defined through several actions. First, the targeting angle acts to reduce the ratio of neutrons and Λs to kaons. This is because the neutrons and Λs each have a stiffer P_{T} (transverse momentum) spectrum than the kaons and they tend to go more forward. Sweeping magnets removed charged particles from the beams. An absorber common to both beams was located between the collimator and the separator slabs, at 15.8 m. The common absorber was comprised of 20 in of Be, to further reduce the ratio of neutrons to kaons, followed by 3 in of Pb, to reduce the photon component. In addition to the common absorber, there was a movable absorber of 18 in of Be. This absorber moved from beam to beam in conjunction with the movement of the Downstream Regenerator (See below). Its purpose was to reduce the flux on that regenerator so that the number of decays was comparable in both beams for the downstream region. By the time the beams had passed through the sweeping magnets and collimators and reached the decay region 117 m downstream of the target, most Λ, Ξ,

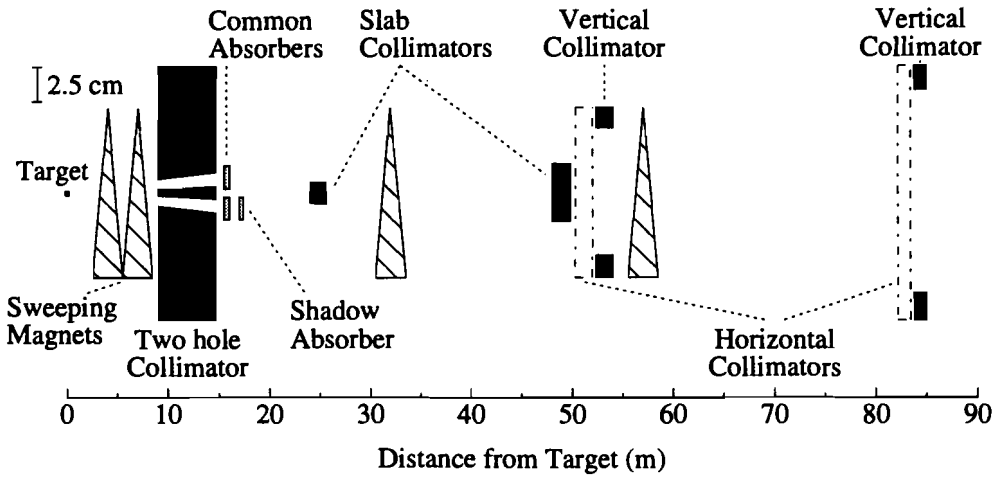

Figure 2.2: Diagram of the beam production and collimation portion of the experimental apparatus, elevation view.

and K_S particles had decayed. This left a beam composed mostly of K_L and neutrons in roughly equal numbers with a Λ and K_S content of 0.05% and 10^{-8} respectively. The Kaons decaying in our apparatus had energies typically between 20 and 250 GeV. The upstream (collimation and filtering) portion of the beamline is shown in figure 2.2.

2.3 Regeneration and Decay Volume

Starting just downstream of the copper collimator, the beam was enclosed in a vacuum pipe in order to reduce the scattering of the kaons and their decay products. There were small gaps in the vacuum pipe for each of the regenerators and the vacuum pipe ended at the first drift chamber, 159 m

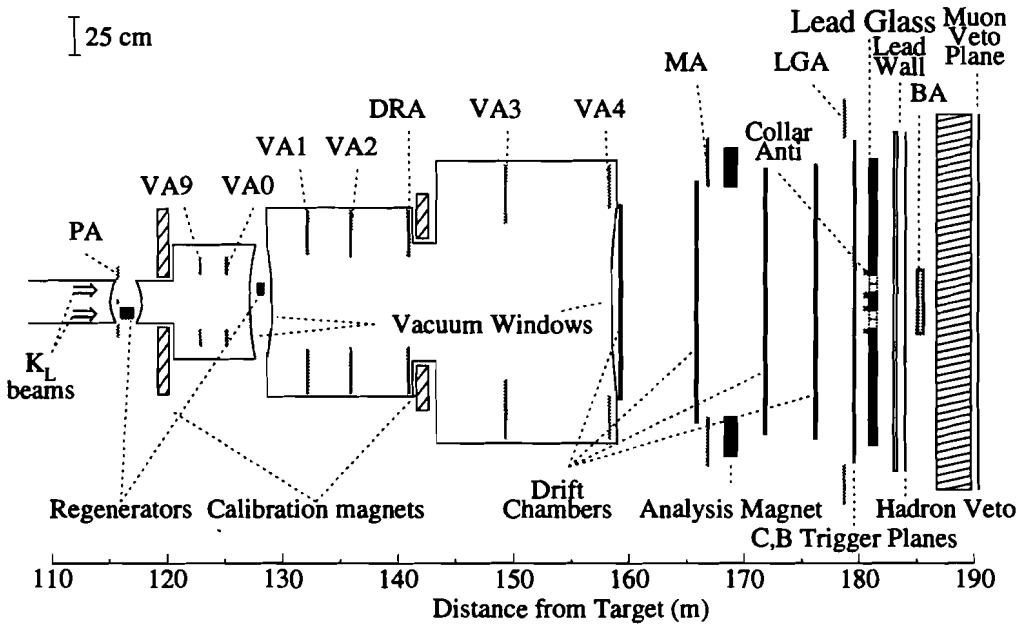

Figure 2.3: Schematic drawing of the FNAL E773 detector.

downstream of the target. At the discontinuities in the vacuum pipe, the pipe was sealed with a window of mylar (127 μm) and Kevlar-29 (584 μm). (The windows and air at these gaps was the source of some particle scattering.) The pipe grew in diameter along the length of the apparatus in order to accommodate the decay particles as they drifted apart. At the downstream end, next to the first drift chamber, the vacuum window was 122 cm in diameter. The pressure in the pipe was less than 0.015 torr throughout the run. A schematic of the vacuum decay vessel and the detector elements is shown in figure 2.3.

To return the desired amount of K_S to the beam, the phenomenon of regeneration was used. E773 employed a new technique in using fully active

regenerators. Each of the two beams contained a scintillator (hydrocarbon) regenerator which returned a K_S component to the beam. They were instrumented with photomultipliers to veto decays which occurred before passing through the entire regenerator and to search for hard scattering within the regenerators.

The Upstream Regenerator (UR) was located 117.14 m downstream of the target and had a length of 119 cm (1.2 interaction lengths). The Downstream Regenerator (DR) was about 11 m further downstream at 128.42 m and was 40 cm (0.4 interaction lengths) long. The UR was composed of 72 scintillator blocks (1.3 in $\times$ 1.5 in $\times$ 3 in) arranged into 36 planes, each 3 $\times$ 3 inches in cross-section and 1.3 in thick. Every fourth plane was instrumented with photomultipliers on one side. The seventh and ninth active planes of the UR went into the trigger as a veto. In contrast, the DR was composed of 24 of the same scintillator blocks in 12 planes and was completely active. Each plane was instrumented from both ends of each block. One set of signals from the last plane acted as a trigger veto. (The Downstream Regenerator is shown in figure 2.4.)

The regenerators alternated between the upper and lower beams between spills. They could also be removed from both beams for special runs. Their positions were monitored (as was that of the moveable absorber which shadowed the DR) and these were read out with the data for each spill.

For the first half of the run, the downstream end of the decay volume was defined by a set of scintillator planes, the T and V (trigger and veto) hodoscope planes, inside the vacuum vessel at 141 m. These planes consisted

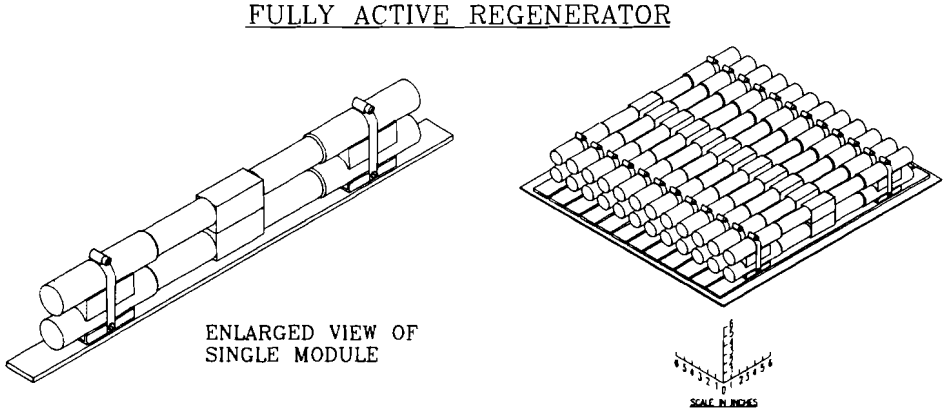

Figure 2.4: Diagram of the Downstream Regenerator with an enlarged view of a single module.

of 6 thin (1 mm) scintillator strips with vertical and horizontal segmentation. A signal was required from one of the two planes for charged mode events, thereby demanding that decays be upstream of it. For the second half of the run, the second level trigger was upgraded. This allowed these trigger planes to be removed and the decay volume was thereby extended to the end of the vacuum region 159 m downstream of the target. This also decreased the material for multiple scattering.

2.4 The Charged Particle Spectrometer

Charged particles were tracked and their momentum analyzed with a drift chamber spectrometer. The spectrometer consisted of four drift chambers, a pair of trigger hodoscopes, and an analysis magnet. The analysis magnet was located between two pairs of chambers and had 1.46 m gap between the pole faces. It had a vertical magnetic field of about 4 kG which provided a transverse momentum kick of 200 MeV to charged particles. Thin skinned vinyl bags were inflated with helium to displace the air between the chambers and thus reduce the effects of multiple scattering.

The Drift Chambers were designed to have good resolution, perform at high rates, and contain a minimum of material to diminish multiple scattering of charged particles. Each chamber contained two horizontal and two vertical planes of wires in a close packed hexagonal cell geometry. This resulted in the second plane of sense wires in each view being offset from the first by one half cell. This allowed resolution of the left right ambiguity (See figure 2.5). The total chamber gas thickness was only three inches. They were operated at atmospheric pressure, and gas flow rates were such that the chamber gas volume was exchanged twice daily. The chambers were filled with a gas of 50/50 argon-ethane with 1% isopropyl alcohol mixed in for additional quenching.

With the hexagonal cell geometry, each sense wire was surrounded by six field shaping wires. The sense wire spacing within a plane was 1.27 cm, yielding a maximum drift distance of 0.733 cm. The chambers increased in

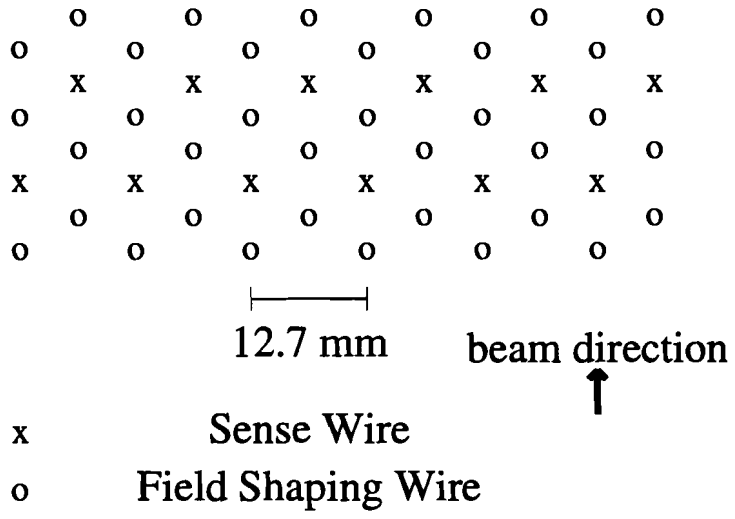

Figure 2.5: The sense and field wire geometry in half of a drift chamber (one view) is shown. Each sense wire was surrounded by a hexagonal group of six field-shaping wires.

size and wire count in the downstream direction to accommodate the diverging decay products. The smallest chamber, the most upstream, measured 1.26 m × 1.26 m and contained 101 sense wires; while the largest chamber was 1.77 m × 1.77 m with 140 sense wires. There was an additional set of field-shaping wires attached to the inside of the chamber window. The sense wires were 25 micron diameter gold plated tungsten, while the field shaping wires were made of 100 micron diameter copper-beryllium. The operating voltage for the field wires was 2.6 kV. The voltage was ramped down to

80% of its nominal value between spills to increase chamber life. The average drift velocity for electrons was approximately 50 μm/ns and the longest drift times were of the order of 150 ns.

The long drift times in the chambers made them unsuitable for use in the first level trigger. So that a charged track trigger could be formed, two planes of scintillator between the last drift chamber and the lead glass, the B and C banks, were utilized in conjunction with the T and V hodoscopes (T&V). In this way, the presence of two charged tracks in each half of the detector could be determined. The C bank was segmented horizontally and was upstream of the vertically segmented B bank. The 1 cm thick pieces of scintillator did not overlap, so that a single particle could not appear in more than one segment. This allowed the definition of simple trigger requirements based on the topology of a two charged track event. These banks are shown in figures 2.6 and 2.7.

2.5 The Calorimeter

The position and energy of photons and electrons were measured by an array of 804 lead glass blocks 181 m downstream of the target. The blocks were made of Schott F-2 lead glass, which has a radiation length of 3.21 cm. They were 5.81 $\times$ 5.81 $\times$ 60.17 cm^3 in size and were arranged parallel to the beam in a roughly circular array (R $\approx$ 0.92 m). The array had two 11.6 cm $\times$ 11.6 cm holes through it to allow the beams to pass. It is shown in figure 2.8. It was housed in its own temperature controlled, light tight room. The voltages

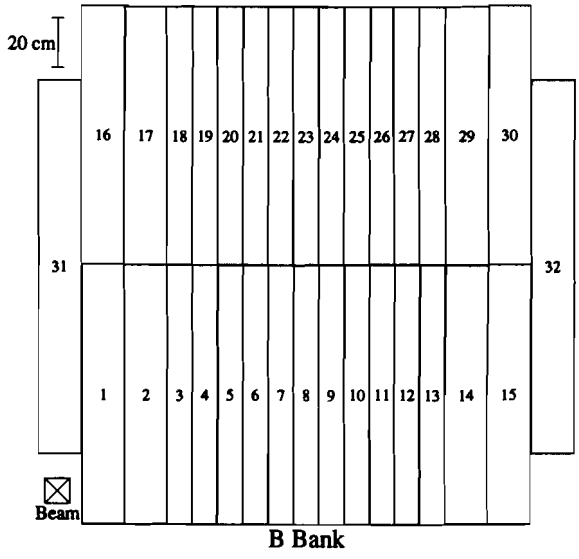

Figure 2.6: Geometry of the B scintillator bank

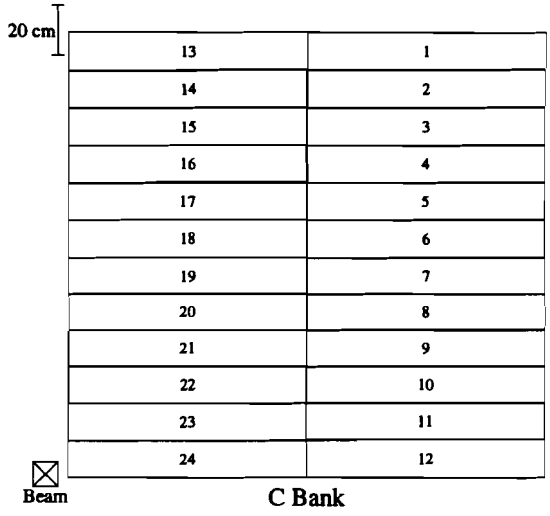

Figure 2.7: Geometry of the C scintillator bank

on the photomultipliers were typically -1200 V, which provided gains on the order of 1.2×10^5.

During the run, the lead glass, particularly those blocks near the beam holes, yellowed due to radiation damage, thus compromising the energy resolution. Changes in the lead glass were tracked with the aid of a xenon flasher lamp. The flasher lamp was a stable source and had a spectrum similar to the Čerenkov light in the glass. The lamp was connected to the upstream end of the lead glass via optical fibers and flashed during the off spill time periods. The effects of radiation damage were fought in two ways. First, voltages to the photo multipliers were adjusted periodically to compensate for the increased light absorbtion. In addition, a mercury vapor lamp was periodically used to expose the glass to intense UV light. The light helped to cure the radiation damage, bringing the transmission of blocks back to a little better than 90% of their value at the previous cure.

The optical fibers used by the flasher were also used to distribute a small amount of steady light from a diode to the front face of each block. The purpose of this light was to stabilize the photomultipliers by maintaining a small amount of anode current.

A variety of signals were formed from the lead glass photomultipliers. The main portion of the signal was formed with a long, 150 ns, ADC gate in order to accurately measure the energy deposited in the glass. A small portion of the signal ($\approx 1/8$) was tapped off and summed in groups of 9 blocks. These 92 "Adder" signals were summed to give the total energy, E_T, which was recorded and used in the trigger. The Adder boundaries are

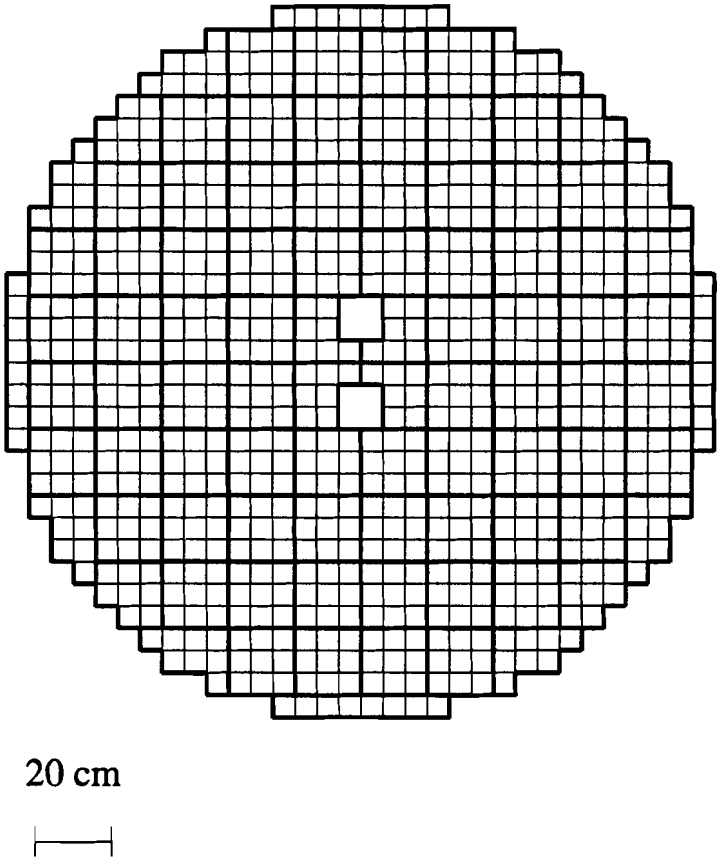

Figure 2.8: The Lead Glass Array

The Lead Glass Array. Outlined in the heavy lines are the boundaries of the Lead Glass Adders.

drawn with heavy lines in the figure 2.8. Each of the adder signals was recorded with a short, 30 ns, gate to allow offline identification of clusters "in time" with the kaon decay. Finally, a small part of each lead glass signal was also tapped off for use by the hardware cluster finder which was part of the neutral decay trigger.

2.6 Event Veto Systems

To reject events in which some decay particles missed the lead glass, (e.g. $K_L \rightarrow \pi^+\pi^-\pi^0$ with one lost photon) there were 12 different veto counters in the decay volume and spectrometer. They surrounded all critical apertures of the detector. A beam's eye view of the detectors is shown in figure 2.9.

The first of the veto counters, the Pinching-Anti (PA), was located just upstream of the Upstream Regenerator at 115.73 m. It vetoed charged particles outside of the beam pipe, thereby eliminating events which had not been subject to regeneration. Between the two regenerators, at 120.28 m, was the Sweeping-Anti (SA) which removed events with decay products that would be lost in a calibration magnet at that position. The Pinching-Anti and Sweeping-Anti were each constructed of scintillator.

The PA and SA were followed by a series of six Vacuum-Anti, VA, detectors inside the beam pipe of the decay region. These annular detectors rejected events with decay products leaving the central part of vacuum pipe. The most upstream of these, VA-1 (also sometimes called VA9), was located 122.87 m downstream of the target. They were spaced periodically to VA4

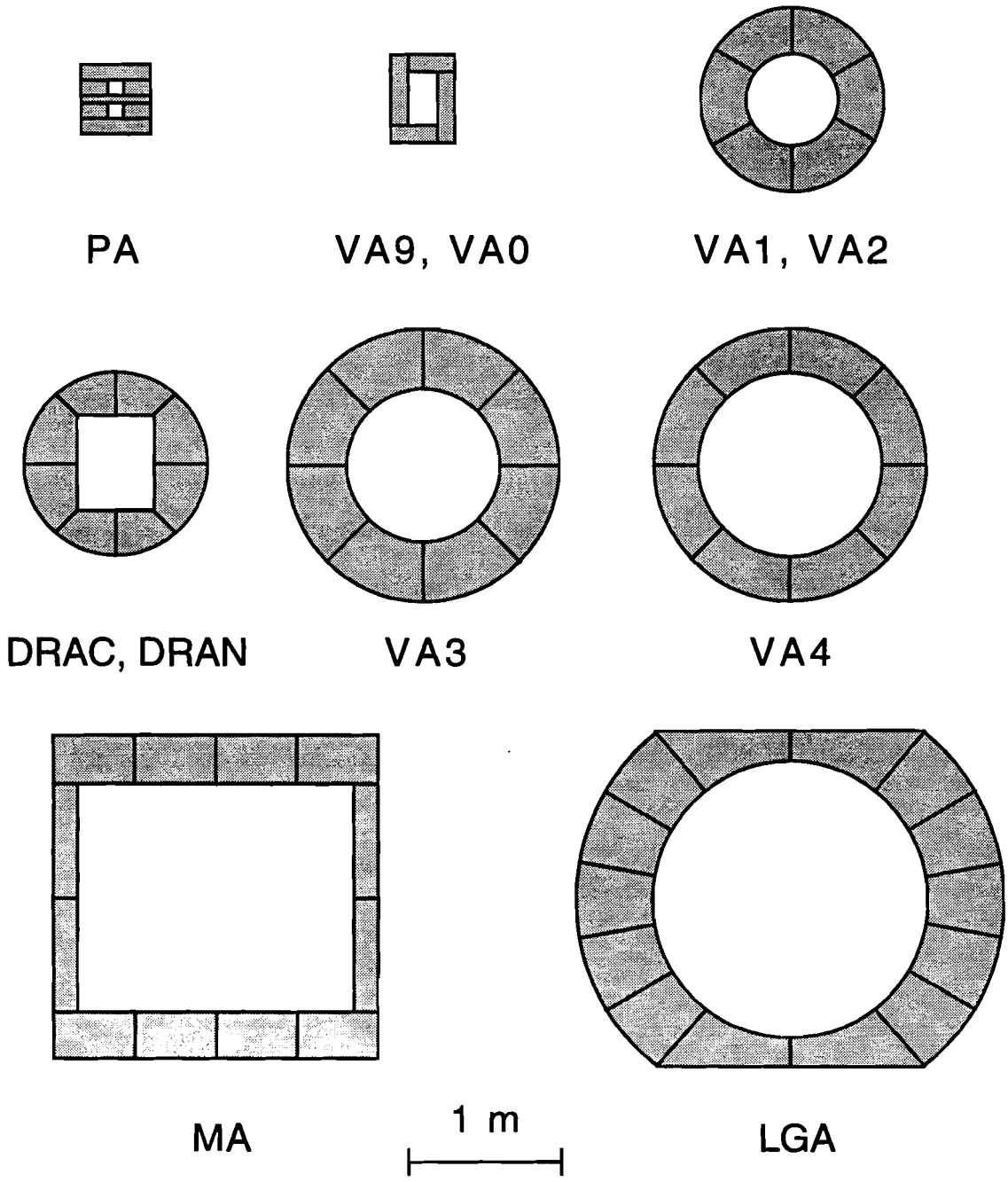

Figure 2.9: The veto counters. Each is shown as viewed by the beam. The segmentation is displayed, but overlaps between counters are not shown.

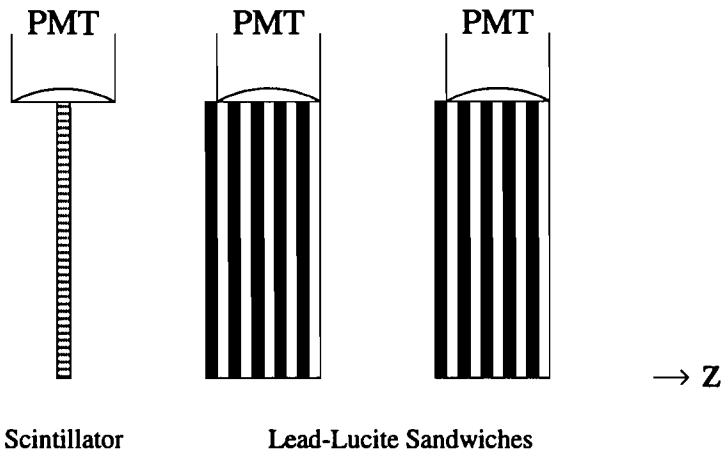

Figure 2.10: Cross-Section of a lead-scintillator photon veto counter

at 158.27 m. Each VA contained a plane of scintillator (6 mm) for charged particle identification and two layers of lead-lucite (3 mm, 6 mm) sandwiches for identifying photons. (See figure 2.10)

Two other veto counter sets, DRAC and DRAN (Decay Region Anti Charged and Decay Region Anti Neutral), surrounded the T&V trigger planes at 140.91 m and consisted of a lead-scintillator sandwich. Finally, the Magnet-Anti (MA) and Lead Glass-Anti (LGA) formed the apertures for the analysis magnet and the lead glass calorimeter. They were similar to the VAs in construction.

Photons passing close to the beam holes in the lead glass were identified by the Collar-Anti (CA). The CA contained a layer of copper and a layer

of lead followed by a layer of scintillator. It formed a collar 1/2 block wide around each of the beam holes and gave a well defined inner edge to the acceptance and vetoed photons in danger of misreconstruction (since the shower might not be completely contained in the glass).

Behind the calorimeter was a wall of lead bricks 21 radiation lengths deep. This wall had a single hole in it which allowed both beams to pass through. The combined thickness of the Lead Glass and the lead wall (in total 41 radiation lengths or 3 hadronic interaction lengths of material) was sufficient to completely contain electromagnetic showers but not hadronic showers. The MU1 scintillator bank stood downstream of the lead wall and was used to identify hadronic events. Hadronic showers, which were typically not contained, gave a large pulse height in MU1. There was also a single hole in this bank through which both beams passed. This hodoscope is shown in figure 2.11.

Photons passing through the beam holes were tagged by the Back-Anti (BA). The BA was a large, multilayered, lead-lucite sandwich counter centered on the beam holes. It was highly segmented, both longitudinally and transversely, to be able to withstand high rates and to distinguish between neutrons and photons. The BA was divided longitudinally into three modules. Each module contained 16 layers of lucite and lead. Therefore, there were in total 48 layers of lead and lucite with a total of 16 cm (28 radiation lengths) of lead. The layers alternated between horizontal and vertical segmentation. All eight segments within a module which were longitudinally aligned were linked to a single photomultiplier tube. The ratios of signals in

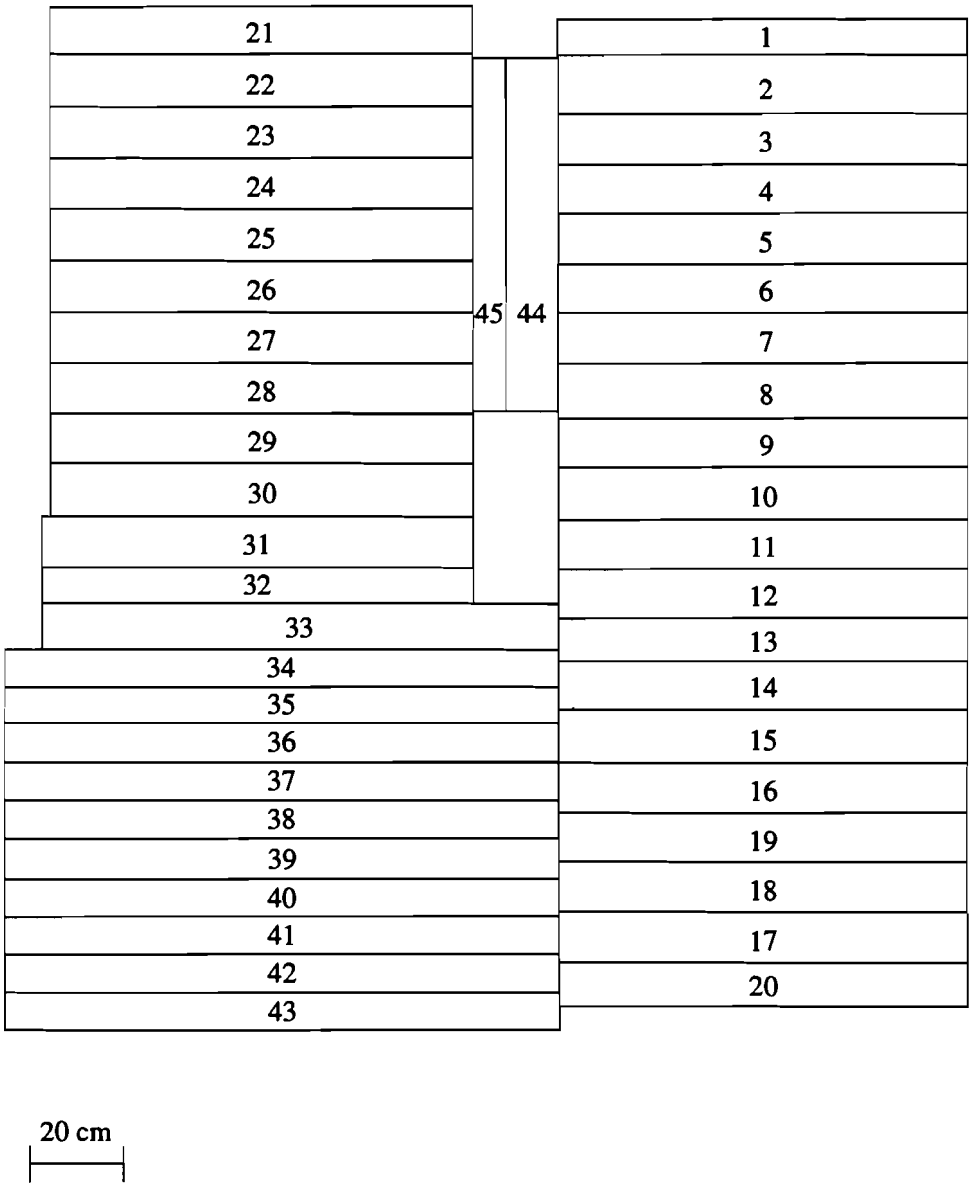

Figure 2.11: Geometry of the MU1 scintillator bank

the modules gave information on shower development.

Downstream of MU1 and the BA was a muon filter composed of 3.2 m of iron. Muons above 7 GeV/c passed through this filter with a very high probability. The filter was followed by two scintillator banks MU3 and MU2, shown in figure 2.12. MU3 was a smaller bank which covered the central beam pipe region. MU2 was downstream of MU3 and covered the whole area of the glass for vetoing $K_{\mu 3}$ ($K \rightarrow \pi\mu\nu$) decays or events with accidental muon activity.

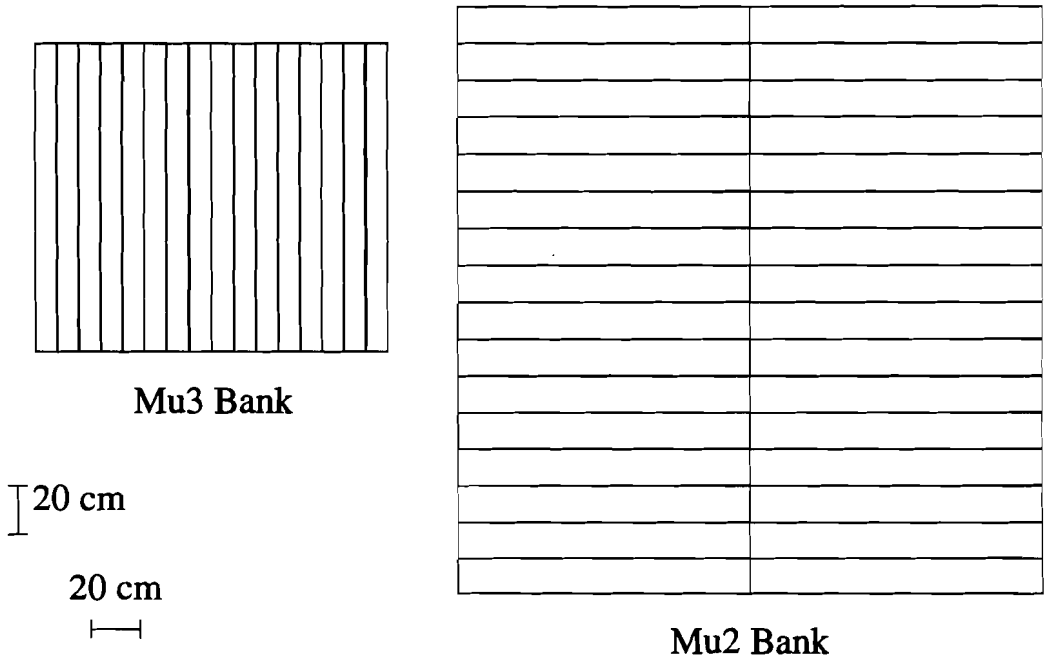

Figure 2.12: The Muon Trigger Banks

Chapter 3

Data Collection

3.1 The Trigger System

The trigger system for E773 had a two level structure. The first level was formed from the prompt signals which were available for each 19 ns "bucket" in the proton spill. When a first level trigger was received, further triggers were inhibited. The next step was dependant on the type of trigger satisfied. Events satisfying the Accidental or ADC pedestal data triggers (see below) were read out immediately, however physics triggers also had to satisfy a second level trigger requirement which further reduced the rate. The neutral mode trigger required that the calorimeter contain a specific number of isolated depositions (clusters) of energy in the calorimeter while the charged mode trigger was based on the number and distribution of hits in the drift chambers. The level 2 decision took 30 μs. It was limited by Hardware Cluster Finder which determined the number of clusters in the calorimeter. The full time was allocated even if the HCF was not used in the particular trigger in question.

If an event failed the second level requirement, an abort was sent which

resulted in a fast clearing of the Data Acquisition (DA). The ADCs were then allowed to settle for 500 ns and then first level triggers resumed as quickly as possible. Events which succeeded in passing the second level requirements initiated the readout of the event to buffers and then to tape. Upon commencement of the readout, the first level triggers were re-enabled.

3.2 Trigger Logic

The $\pi^+\pi^-\gamma$ decays were collected under the charged mode trigger which was designed to pick out $\pi^+\pi^-$ decays. The trigger for this mode demanded two charged tracks traverse the detector. The tracks were required to be in a geometry consistent with decays into two oppositely charged particles, namely that there be one track on either side of the horizontal and vertical mid-planes of the detector. No requirement was made on the energy in the lead glass array.

3.2.1 Level One Trigger

The first level provided a decision for each bucket based on information from fast detectors such as the assorted hodoscopes and veto counters as well as a quick energy sum from the Lead Glass. Because decays with products leaving through the sides of the decay volume would not be well measured, any events with hits in any of the Vacuum Anti counters were vetoed. Similarly, signals from the PA, DRAC, and LGA were used to veto the event. With the exception of the LGA, the signal used in the veto was the fast signal from

the scintillator portion of the device. In the case of the LGA, the output from the lead lucite sandwich was used. This helped reduce the rate from $K \rightarrow \pi^+\pi^-\pi^0$ with one of the photons outside the fiducial volume of the Lead Glass. To reject kaons which had decayed before passing through the entire regenerator and inelastically regenerated events, the seventh and ninth planes of scintillator in the Upstream Regenerator and the final plane in the Downstream Regenerator were used as vetos. This requirement also defined the start of the decay volume. To reject $K_{\mu 3}$ ($K_L \longrightarrow \pi\mu\nu$) triggers, events with any signal in the MU2 counters were also vetoed.

The portion of the level one trigger which acted to pick out the two charged track events consisted of requirements on the T&V and B&C hodoscope planes. The T&V hodoscopes were summed over the six counters in each of planes and discriminated at the equivalent of 1.5 minimum ionizing particles. To maintain high efficiency, since these counters were relatively thin (1 mm), a positive signal was required from only one of the two sums (T or V). At the other end of the detector, the B and C banks were each required to have two or more counters hit. In addition there was an east-west requirement on the hits in the B bank and an up-down requirement for those in the C bank (one hit on each side of the vertical and horizontal mid-planes of these detectors).

The coincidence of T/V and B/C hits assured that there were two charged tracks at each end of the detector. This was a powerful criterion in selecting a two charged track sample. It also discriminated against three body decays which were background such as $K \rightarrow \pi e\nu$, $\pi\mu\nu$, and $\pi^+\pi^-\pi^0$ since both

charged tracks could then end up on the same side of the center plane. It also discriminated against the $\pi^+\pi^-\gamma$ decay. The IB events were affected to a lesser degree since the decay started as a two body decay and the photon more or less followed the pion which emitted it. However, the DE events had a more energetic photon and more of a three body decay distribution. This is one reason why the DE events have a significantly lower acceptance than the IB events.

When the T&V hodoscopes were removed from the detector half way though the run, much of the power of the first level trigger was lost. The trigger could easily be satisfied by some combination of noise in the B&C banks and tracks from accidental muons in the rear of the detector. This burden was then shifted to the second level trigger as described below.

3.2.2 Level Two Trigger

For the first half of the run, when the T&V hodoscopes were still in use, the second level trigger employed a so called Chamber East-West (CHEW) logic. This required that each of the four chambers had at least one hit on each side of the centerline in the x view. An OR was formed of all of the wires, in both planes of the view, on each side of the center line of each chamber. The x view was chosen since both beams are centered in this view.

The CHEW requirement further strengthens the two charged track case by demanding that its topology be satisfied at more locations along the length of the detector. It also further discriminates against the three body

decays. The CHEW logic was not always imposed during the first half data taking due in part to work in progress on the second level trigger. However, to simplify the analysis, it is always imposed in software for this data set.

With the removal of the T&V hodoscopes, much of the discrimination strength was lost as mentioned above. A new second level trigger called ZUMA took its place. ZUMA involved exercising crude pattern recognition in the drift chambers. First, ORs were formed from 16 adjacent wires (8 from each view) in a chamber plane pair thereby defining a "paddle". Using a fast memory look up table, the number of potential track segments on each side of the analysis magnet was determined. A second stage applied requirements on the number and distribution of the segments.

The lookup tables used by ZUMA were determined by looking at the distribution of tracks in $K\pi 2$ decays generated by the Monte Carlo. Basically, it paired chamber 1 with chamber 2 (and chamber 3 with 4). When a hit is found in a paddle in a chamber, a hit is expected in that chamber's partner in a paddle directly in line with the first paddle or an adjacent paddle. The tracks were generally opening up as they moved downstream. The ZUMA boards used information from both the x and y views. These views were checked independently and events were required to satisfy both in order to lead to a successful trigger. It took approximately 100 ns to form this trigger from the end of the gate defining the valid time for chamber hits.

3.2.3 Other Triggers

The other major trigger in E773 was the neutral mode trigger which was designed to pick out $\pi^0\pi^0$ and $\pi^0\pi^0\pi^0$ decays. The first level trigger here was similar to the charged mode trigger. It included all of the same veto counters as well as the CA and BA. The CA vetoed events with a photon within a half block of the inner edge of the Lead Glass where reconstruction was likely to be compromised. When most of energy was deposited in the front segment of the BA and little energy was deposited in the rear, it was indicative of a photon escaping down the beam hole. The BA only vetoed events which looked like a photon (as opposed to a hadron) had gone down the beam hole.

The second level trigger for the neutral mode was based upon the Hardware Cluster Finder (HCF). This is described elsewhere in detail. [34, 35] Basically, it provided a count of the number of clusters (depositions of energy) in the Lead Glass calorimeter. The information was available 30 μs after the first level trigger was formed and it accepted events with 4 or 6 clusters. If triggers for both the charged and neutral mode were satisfied, the event was treated as a charged mode event.

It is important in the Monte Carlo simulations of the detector response to include some model of the activity in the detector not caused by the actual decay of interest. A set of three small scintillators, independent of the rest of the detector, was added to select events with muons originating in our target. The muon telescope used to form this trigger was placed well outside

of the fiducial volume of the detector, about 30 m from the target at an angle of about 25 mrad away from any active element of the detector. In this way, the activity in the accidental trigger was correlated to the instantaneous rate of the protons arriving on the target and hence to the data rate. These accidental events were overlayed with the Monte Carlo to study the effects of noise in the detector. About 1% of the events written came from this trigger.

A pedestal trigger was also formed to monitor the pedestals for all of the ADCs in the experiment. Typically, 10 pedestal events were recorded each spill cycle. These were averaged and downloaded into the ADC controllers in each FASTBUS crate for subtraction during the next beam spill.

Finally, as mentioned above a Xenon flasher lamp was used to monitor the performance of the Lead Glass. The light from the lamp was distributed to the front surface of the glass blocks by optical fibers. Between 10 and 15 such events were recorded during the off-spill time.

3.3 Electronic Readout / Data Aquisition

Once an event was accepted by the trigger, all information from the event was gathered and written to tape. The experiment used LeCroy dual-range FASTBUS ADCs. The ADC data was read out with a 5-count threshold used to sparsify the data. A PDP 11/43 communicated with the ADC modules in order to change the digitization from low to high range, for taking pedestals, and to download the updated pedestals between spills. The drift chamber

TDC system used CAMAC modules with crate controllers. In addition, all scalers and latches were CAMAC devices. They were read out via Smart Crate Controllers (SCC) into a FASTBUS module. The total readout and digitization time for the CAMAC and FASTBUS subsystems took about 800 μs/event.

Each data stream was buffered in a LeCroy FASTBUS event buffer. This allowed the data collected over the 22 second spill to be read out over the entire 1 minute long spill cycle. The data was assembled from its sub-parts and again buffered by a FASTBUS crate which contained the event builder and memory for storing events. A VME controller crate controller crate shipped the completed events to four 8mm Exabyte tape drives operating in parallel. The buffers required almost the full minute to empty. A full data run took almost six hours to complete. Runs were often ended before the tapes were full for various reasons.

3.4 Running

Over the course of the data collection, many special runs were made in order to study the detector components. In order to align the chambers, runs were made with straight through muons. For these runs the analysis magnet was turned off and the trigger simply required one hit in the B bank and one hit in MU2 (or one hit in the C bank and one hit in MU2). Use of the B and C banks was alternated so that the performance of the other bank could also be checked. Similar triggers were also used to check the performance of

other detectors such as the regenerators and VAs (Vacuum Antis).

Many special runs were also made to allow the study of various trigger elements. For example, there were runs with no VA counters, no regenerator vetos, no CHEW/ZUMA requirement in the trigger. Runs were also made with no regenerators in the beam.

At four times during the experiment, special electron calibration runs were taken to calibrate the calorimeter. During these runs the lead photon absorber in the common absorber was removed and a copper sheet was added a short distance downstream. Photons striking the copper sheet produced electron positron pairs. The trigger for these calibrations was therefore very similar to the charged mode trigger. It actually used two trigger lines one using the B and C banks to select only the tracks in the outer region of the Lead Glass. The other line was prescaled. This ensured that sufficient data was collected for all blocks not just the blocks closest to the beam. These data from these runs could be rapidly analyzed and the results used to adjust the photomultiplier voltages. In this way the gain balance between the channels was maintained.

During the E773 run, the experiment was live about 50% of the time. It collected about three times as many charged as neutral events. About 450 million triggers were written onto about 1000 8mm tapes.

Chapter 4

The Reconstruction of Charged Particles

4.1 Reconstruction of Tracks

The first task in understanding the decays was their reconstruction. The best understood part of the decays was the charged track information, hence it was the starting point. Beginning with the hits in the wire chambers, the hits belonging to each track must be identified and the resultant tracks must then be fit to determine the direction of the particle. In this task, it is necessary to be able to specify individual chambers, therefore, they are assigned numbers 1 through 4, with 4 being the most downstream.

The hits were read out from the drift chambers by TDCs operated in "common-stop" mode. The observed drift time distribution of the hits is shown in figure 4.1. The edge at 240 ns corresponds to particles passing very close to the sense wire, while the tail at short times results from particles passing close the the edge of the cell. Hit wires with drift times between 10 ns and 250 ns were considered for association with possible tracks. The drift

distance was then determined from time to distance lookup tables described below. From the drift distance and the position of the wire, the location of the hit in the plane was found. Events with more than 150 hits were discarded as too noisy to be trackable.

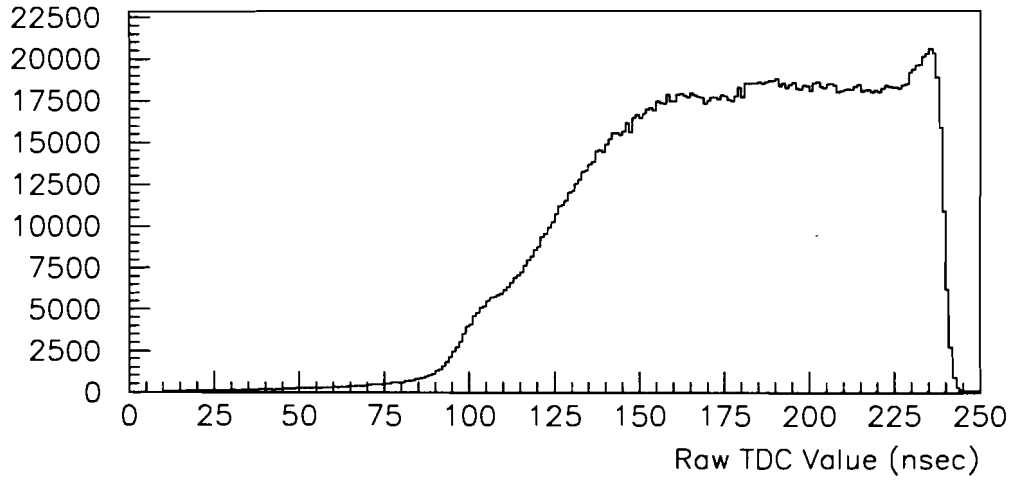

Figure 4.1: The raw distribution of TDC values for all wires in plane 16. Note the sharp edge from charged particles passing very close to a sense wire at high TDC values. The trigger provided a common stop for the TDCs.

Track finding started with the x view. The analysis magnet bent tracks in the horizontal plane, so the chambers upstream and downstream of the analysis magnet were considered separately. A pair of chamber planes, one plane each from chambers 1 and 2 (3 and 4) is taken as a "seed pair" for finding track segment upstream (downstream) of the magnet. Pairs of hits on these planes were connected with an imaginary road. Hits on the other planes

which were within the width of the road at the place where it intersected those planes were considered as associated with a possible track. All valid hits were looped over as well as all possible seed pairs. Once all hits on a segment are found, a least squares fit is performed to find the best line described by the segment.

A full segment has four hits (a pair in each chamber). To be considered valid, a segment must have at least three of the four hits. If one of the hits was missing, then there is an ambiguity in the drift direction associated with the unpaired hit. In this case, both track segments were generated and added to the list of possible segments. All segments were required to pass loose aperture cuts.

Next, the upstream and downstream segments are matched at the mid-plane of the analysis magnet to form full tracks. (The bend in the trajectory was treated as occurring at a single "bend plane" at the center of the analysis magnet.) All pairs of segments were considered and the difference in their projected position at the bend plane was calculated. This separation or miss-distance is called "offmag" and is shown in figure 4.2. Any pairing which matched to better than 1 cm was kept as a possible track.

To this point, there is no restriction on shared hits; that condition is now imposed. Tracks which overlapped with the largest number of tracks were removed first. When this was not a unique condition, then the track with the worst segment matching (at the magnet bend plane) was removed. This was repeated until no hits were shared between tracks.

The tracks in the y view were found in a similar manner except that all

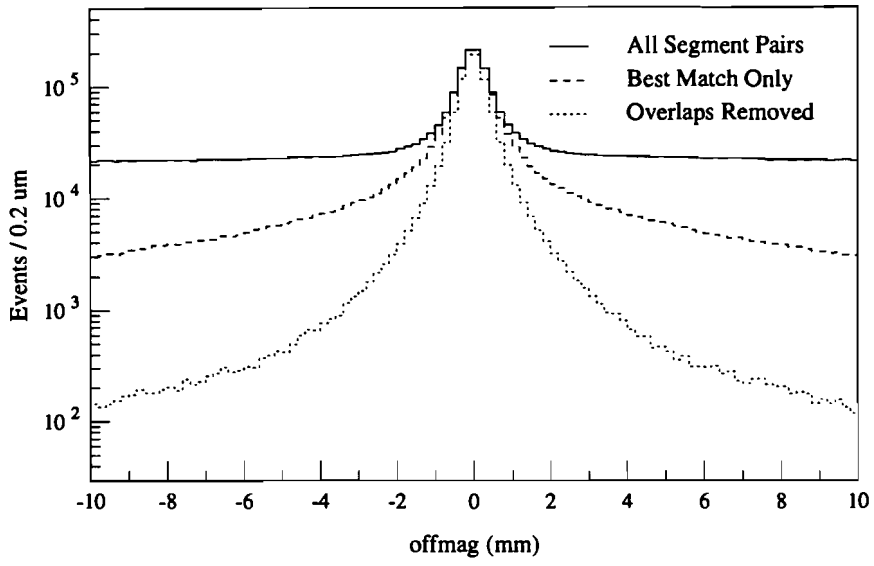

Figure 4.2: The miss-distance of track segments at the magnet during the track-finding. The solid line shows the values for all combinations of upstream and downstream segments. The dashed line shows the values of the best match to each upstream segment. The dotted line shows the values for the final tracks, after overlaps have been removed. The events are from the second half of the data (T & V hodoscopes removed).

four chambers were used simultaneously since the tracks are fairly straight in this view. The tracks had to have at least five of a possible eight hits to be considered valid. After the tracks were isolated, the vertical trajectories were refit in upstream and downstream segments. This gave more accurate trajectories since it took into account the small amount of track bending from the analysis magnet in this view.

The clusters (depositions of energy) in the calorimeter were used to find

the proper matching of the x and y tracks. The two views were matched to a cluster if the projected track came within 7 cm of the cluster center. If there were no clusters (i.e. when tracks pointed outside of the Lead Glass or down its beam holes or when pions deposited only the minimum amount of energy in the glass, resulting in failing the minimum cluster energy cut), then matching fails. Matching also fails if neither of the two tracks matches a cluster. Successful matching is required to insure the reliability of the particle ID cuts which are based on comparing the calorimeter and spectrometer information. Any cluster with an energy greater than 1.5 GeV and not matched to a track is counted as an "extra cluster".

Once the event is fully tracked, a number of corrections can be made to refine the locations of the tracks. These include accounting for the gravitational sag of the horizontal wires, correcting for small chamber rotations about the z axis (as found in the chamber calibration described below), and allowing for the propagation delay along the sense wire. Tracks were then refit to the best line.

The vertex is found by calculating the distance of closest approach of the extrapolated track segments. The vertex coordinates are then taken as the centroid of this closest approach. This preliminary vertex is used to determine what material the tracks would have passed through. A more complicated vertex fitter is then used to refine this position. It includes error in the angles and intercepts due to the multiple scattering and the resolution of the spectrometer.

4.2 Calibration, Resolution, and Efficiency

The calibration of the drift chamber system consists of two tasks: determining the time to distance relations and finding the chamber locations.

To begin, the timing offsets between wires had to be removed. These relative offsets were mostly due to small variations in the cable lengths, however there were also wire to wire differences within a cable which were on the order of a few ns. These were sufficiently large that they would dominate the resolution if left uncorrected, so individual offsets were found for each channel in order to maintain good resolution. These timing offsets were obtained by plotting the raw drift times (as in figure 4.1) and matching the sharp edge which was due to the prompt hits from tracks passing right by a wire. Now one time-to-distance relation could be formed for each sense wire plane.

Recall that a track should have two hits in adjacent planes and that sense wires in adjacent planes are offset by a half cell or 0.635 cm. Using the drift times to determine the drift distances from the wire, the sum of these distances should equal the cell size (0.635 cm) for paired hits. From the width of the peak of this distribution, the Drift Chamber single hit resolution was measured. One such distribution is shown in figure 4.3. The resolutions were all in the range of 80-100 μm and were stable as a function of time.

An additional timing concern is the time of passage of the tracks relative to the common stop signal sent to the TDCs. This stop was generated by the first level trigger which was synchronous with an accelerator RF signal.

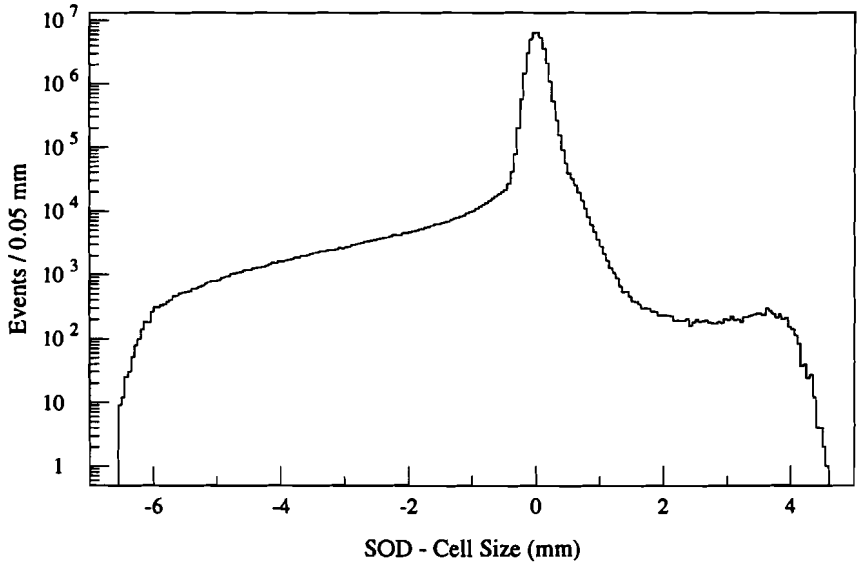

Figure 4.3: The sum-of-drift-distances minus the cell size for one wire plane pair. The cutoff at 4 mm is due to a cut in the tracking algorithm. The prominent left shoulder is due to δ-rays. This plot contains tracks from all $K \rightarrow \pi e \nu$ decays from the second half of the data (without the T&V hodoscopes). The single-hit resolution of each plane in this pair is about 82 μm; this is the best resolution achieved in the system.

The chamber single hit resolution, σ, is about 90 μm. Each pair of chamber hits measures the cell size via the sum of distances with a resolution of $\sqrt{2} \cdot \sigma \approx 125$ μm. Given the drift speed of ≈ 50 μm/ns, the pair of hit wires provide a measure of the relative stop time to about 1.3 ns. There are 16 independent pairs in a perfect two track event, so that the total time resolution in this case is four times better than that from a single pair. The time offset required to give a perfect sum of distance is determined for each

hit pair. The average offset is used to determine the apparent time shift in the stop signal. However, only those sums which are within 0.5 mm of the cell size are included in this average and at least 10 good sums are required to contribute to find the average. This time is then used to adjust the drift times of all hits in a given event.

Once the timing is well understood, the relation between the observed drift time and the actual distance between the track and the hit wire can be determined. On average, the illumination across the drift cell of a plane pair is uniform. This allows one to convert the distribution of observed times into a lookup table relating times and distances (t and d) via the relation:

$$\mathrm{d} = \mathrm{d_{max}} \cdot \frac{\int_{t_{max}}^{t'} \mathcal{N}(\mathrm{t})\mathrm{dt}}{\int_{t_{max}}^{0} \mathcal{N}(\mathrm{t})\mathrm{dt}}. \tag{4.1}$$

Here, d_{max} is the cell size (0.635 cm), $\mathcal{N}(t)$ is the number of observed events, and t_{max} = 240 ns. A typical time-to-distance relation is shown in figure 4.4 This relation is quite linear between 10 and 110 ns and has a slope of about 50 μm/ns. The time to distance conversion tables were recalculated frequently the course of the run to track changes in the distributions.

Special muon data runs were used for the alignment of the Drift Chambers. These were "straight through" muons recorded with the analysis magnet turned off. The alignment (offset and rotation) was determined separately for each plane. The positions of chambers 1 and 4 were assumed and the hits in them were used to predict the locations of hits in chambers 2 and 3. The residual between the predicted and observed values were then examined as a function of the track position within the chamber. A line was fit

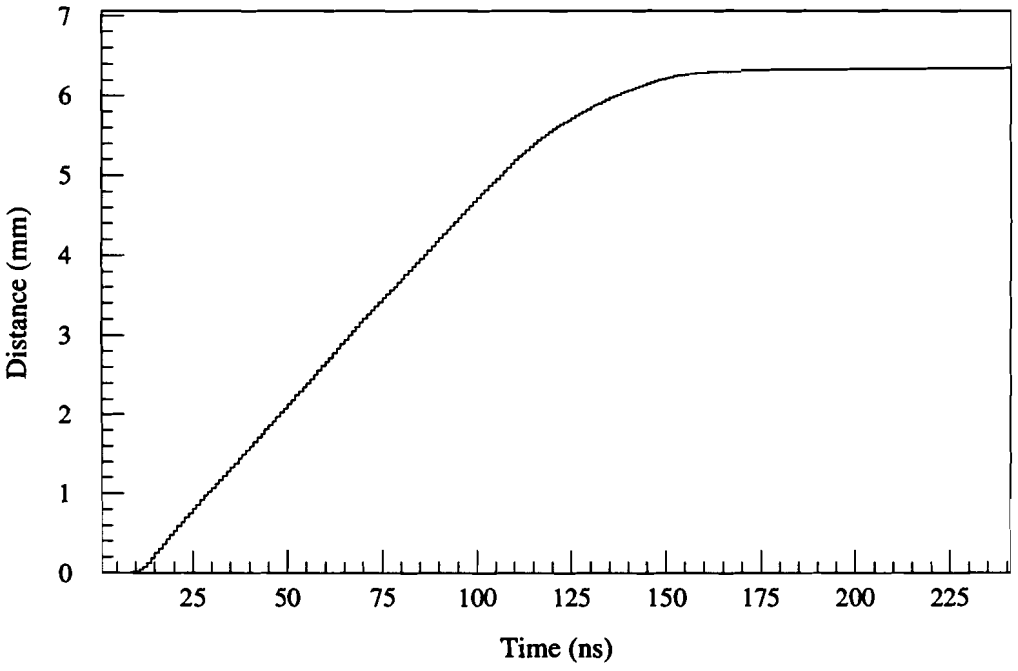

Figure 4.4: A typical time-to-distance relation for the drift chambers. We use one such relation per plane, and update them about once per day. The relation is quite linear between 10 and 110 ns, with a slope of about 50 μm/ns.

to the x-residual as a function of y for each of the four x planes in chambers 2 and 3. The slope of this line gives the rotation angle of each x sense plane and the offset at $y = 0$ gives the offset of the plane. The analogous fits were performed for the y residuals as a function of x and the process was repeated assuming the positions of chambers 2 and 3 to find the planes in chambers 1 and 4.

In this exercise, the x and y views were not assumed to be orthogonal.

The rotations of the x and y sense wire planes in a given chamber are not the same due to small non-orthogonalities arising in construction. These were determined in bench measurements of the chambers before the running of E731.

If the rotations about the z axis assumed for chambers 1 and 4 are incorrect, then the positions of chambers 2 and 3 found above may be in a "corkscrewed" frame. The fact that two-track events are planar is used to measure the corkscrew rotations. Regular data collected with the magnet on was used to perform this measurement. Two line segments were formed between the intersections of the tracks with the two chamber planes. By studying the aplanarity between these segments, one could resolve corkscrew angles of less than 1 μrad.

The chamber system must also be tied to the experimental coordinates where the target is the origin and and line connecting the target to the center of the Lead Glass is the positive z axis. This was accomplished by reconstructing Kπ2 decays and pointing the kaon back to the target. Care was made to select kaons which did not scatter in the regenerator to do this.

Finally, the efficiencies were measured for each wire in the system by analyzing a large sample of events and keeping track of the distribution of missing hits. The chambers had an average efficiency near 99% and only four wires had measured efficiencies lower than 90%.

4.3 Momentum Determination

The momentum of a track was determined from the bend angle between its upstream and downstream track segments. The momentum, p, of a track was related to its bend angle, $\Delta\theta$,

$$p = \frac{P_k}{\Delta\theta}. \tag{4.2}$$

Here, P_k is the "momentum kick" delivered by the magnet. It is given by $P_k = -e \int \vec{B} \times d\vec{l}$, where $d\vec{l}$ is taken along the path of the particle and $\vec{B}$ is the field strength of the magnet. The field of the magnet was carefully mapped for E731 at the same driving current as was employed in E773. The central field in the magnet was measured to be about 0.38 T, resulting in a momentum kick, P_k, of 200 MeV/c.

The momentum resolution of the spectrometer was limited by the measurement of the track bend angle. The root mean square uncertainty in the momentum due to the chambers themselves, based on the 90 μm hit resolution and chamber geometry was $0.013\%p$, p is in GeV/c. Additional momentum smearing arose from the multiple scattering of the tracks, which changed the apparent bend angles in the analyzing magnet. This yields a contribution to the resolution from multiple scattering of 0.45%. The momentum resolution is then

$$\left(\frac{\sigma_p}{p}\right)^2 = (0.45\%)^2 + (0.013\%p)^2, \tag{4.3}$$

with p again in units of GeV/c. For pions from a kaon decay with a momentum of 35 GeV/c, the momentum resolution was about 0.65%.

Chapter 5

The Reconstruction of Neutral Particles

5.1 Energy and Position Measurement

To complete the reconstruction of decays, more information was required, in particular a measurement of the photons. The Lead Glass calorimeter provided an energy and position measurement of each particle within its acceptance. For hadrons and muons, it typically provided a minimum energy cluster useful for matching with the tracks from the spectrometer. In the case of the photons, the calorimeter provided the only measurement of the particle. It provided both the energy and position at the calorimeter. This information, when paired with the decay vertex provided by the charged tracks in the event, was sufficient to determine the momentum vector of a photon. The calorimeter was also useful for isolating backgrounds from the data; for example through the identification and separation of electrons and pions.

The cluster reconstruction algorithm searched the Lead Glass array for

local maximum of block energies. A 3 × 3 block array surrounding that maximum was then considered as a cluster. A cluster was "found" if the central block, containing the maximum, had an energy greater than 0.25 GeV and the total cluster energy (the 9 block sum of energies) was greater than 1.00 GeV. Two clusters were distinct if there was an energy minimum between their cluster centers.

The energy of an incident particle was reconstructed from the record of ADC counts in two stages. In the first stage, the energy was estimated by summing the ADC counts from the nine block cluster and dividing by the "gain" of the central block. This estimate was good to about 30% of the incident particle energy. In the second stage, a more precise determination was made by taking into account the absorbtion of the Čerenkov light and the differences between electrons and photons.

Several small corrections were also made to the energy; some energy dependant, some not. Among the energy dependant corrections are factors to account for radial leakage outside the nine block sum and a correction for energy lost because one or more of the nine blocks in the sum was missing (as was the case when the central block was next to the beam hole or outer edge of the array). A small amount of energy was also added to adjust for blocks which probably had a small amount of energy but not the 5 ADC counts required to be written out. This correction was determined from special runs with the 5 count threshold inhibited. An example of a non-energy dependant correction was the pedestal correction. The pedestals for the Lead Glass ADCs showed a small amount of rate dependant shift which

was corrected using a function which depends on the instantaneous rate seen by the ADCs. Also, during the early part of data taking, the temperature control system of the lead glass enclosure was broken. For this data, it was necessary to multiply the energy estimate by a factor which depends on the enclosure temperature to eliminate the temperature dependence of the gains.

In addition to determining cluster energies, cluster positions are found using the calorimeter. Cluster positions were determined from the ratios of energies in the columns and rows of the 3×3 array. The shower was assumed to be centered in the central block of the cluster. The distance from the center of the block to the cluster position was determined separately in x and y. The central block and the eight adjacent blocks make 3 rows and 3 columns. In determining the x position of a cluster, the estimated energy in the side columns was compared with the estimated energy in the central column. The cluster position was assumed to be closer to the side column with greater energy. The ratio of the energy in this side column to the energy in the central column determined where between the block center and edge the cluster is. Using the observed distribution of the ratio (which was between 0.0 and 1.0) and the assumption that cluster positions are distributed evenly across the face of the block, each value of the ratio can be mapped to a distance from the center of the block. The y position was found similarly using rows. An average position resolution of 3 mm was achieved in both x and y based on a comparison of the track projections and cluster positions of electrons. Better resolutions were achieved for clusters centered near block edges due to the fact that most of the energy (90%) of

an electromagnetic shower was typically contained within a cylinder with a radius of one radiation length. (Recall that the lead glass blocks have a radiation length of 3.21 cm and are 5.81 cm×5.81 cm face on.)

5.2 Glass Calibration

The reconstruction of showers depends on three parameters, two gains (one for each ADC range) and an absorbtion coefficient, α. Each of these calibration constants must be determined for each block and changes over time. The first calibration of the lead glass was accomplished with electrons collected in periodic calibration runs. During these runs, the lead photon absorber near the target was removed and a thin sheet of copper was inserted a few meters downstream. Neutral pions produced in the target decayed into photons which then produced the electron-positron pairs on collision with the copper sheet. Using magnets upstream of the spectrometer, the momentum of the electrons could be selected and they could be directed across the face of the glass. The lead glass response was then studied by comparing its energy measurement to the momentum determined by the Drift Chamber spectrometer. Using this electron calibration data, the lead glass was investigated in detail over the energy range from 2-20 GeV.

As previously mentioned, over the course of the run, the blocks experienced radiation damage resulting in yellowing and loss of light transmission. Greater light attenuation within the blocks increased the nonlinearity of their response. Blocks near the beam pipes, which saw more radiation, were

particularly affected and exhibited noticeable changes on short time scales (on the order of days). To fine tune and keep more continuous track of the damage to the glass, the calorimeter was recalibrated using 20 million electrons from $K_L \rightarrow \pi e \nu$ (K_{e3}) decays which were collected during regular data taking. These electrons also had a broader energy spectrum which was more representative of the photon energies we wished to measure.

A clean K_{e3} electron sample was obtained after eliminating possible backgrounds. $\Lambda \rightarrow p\pi$ events were removed by cutting on the $p\pi$ mass and the ratio of the momenta of the two tracks. $K \rightarrow \pi^+\pi^-\pi^0$ decays were eliminated by cutting on the square of the longitudinal momentum of the possible π^0. This cut will be discussed in more detail when it is used to remove the same background from the $K \rightarrow \pi^+\pi^-\gamma$ data. Background from $K \rightarrow \pi \mu \nu$ ($K_{\mu 3}$) decays was cut with the muon veto system while background from $K \rightarrow \pi^+\pi^-$ was cut with a lifetime cut followed by a mass cut. To ensure a clean sample, additional cuts required the tracks be cleanly reconstructed and the pion and electron were well separated. There were also cuts on shower shape and the distance between the cluster position and the projected electron track to eliminate electrons with bremsstrahlung. Lastly, the decay had to be kinematically allowed when reconstructed as a K_{e3} decay.

The central blocks experienced the most damage and needed to have their constants updated more frequently. Since the K_{e3} electrons also hit those blocks more often than blocks near the outer edge of the array, it was possible to break the data up into subsets to accomplish this. The gains and absorbtion coefficient of each block were first found using showers from the

entire run. Next, the run was divided into an early and late half. Those blocks hit often enough in each half to determine their gain and alpha in each half were recalibrated keeping the gains and alphas of those blocks which were not hit often enough fixed at the values found with the larger data set. Only a few of the 804 blocks could not be calibrated using half the run. The ratio of the high range gain to the low range gain depends only on electronics and was constant over the course of the run once determined. Hence, only two parameters not three are fit in the smaller data sets. The run was then divided again and again, each time calibrating all blocks hit often enough, until the most damaged blocks had their gain and alpha determined about once a day.

Each block was calibrated separately using showers centered at that block and assuming the gains and alphas of the adjacent blocks were correct. After updating the gain and alpha of a block, the next block was calibrated. The calibration procedure iterated over all blocks and showers several times until changes of only a fraction of a percent were seen in the gains and alphas. The results of the calibration are shown in figures 5.1 - 5.2. Figure 5.1 shows the energy/momentum (E/p) ratio for the K_{e3} electrons. The r.m.s. width of the peak region is about 3%. The mean and width of the E/p distributions are plotted as a function of the electron's track momentum (figures 5.2 a and b).

The resolution for electron showers is limited by two effects. The first of these is the fluctuations in the showers themselves. These fluctuations are largest at low energies where statistical fluctuations in the number of shower

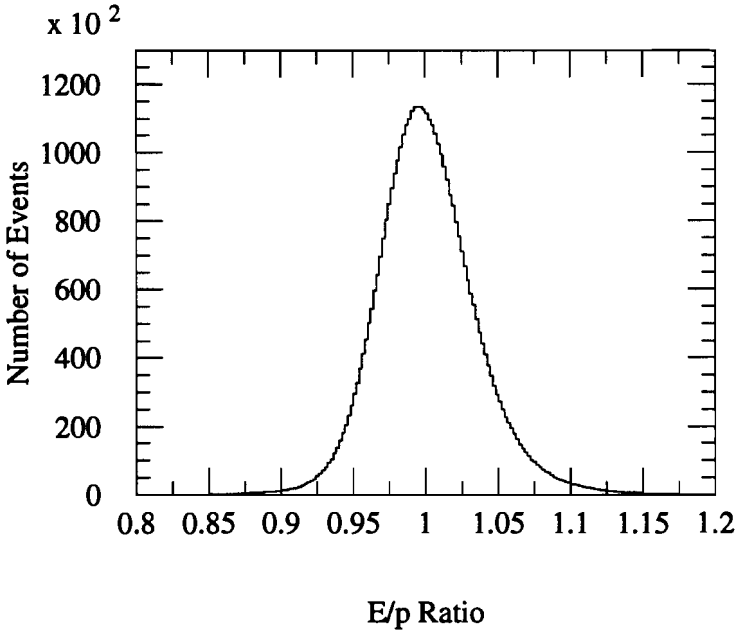

Figure 5.1: The ratio of the electron's energy, as measured by the Lead Glass, to it's momentum, as measured by the magnetic spectrometer, (E/p) for for electrons from K_{e3} decays. Though Gaussian at the peak, the whole distribution is not quite Gaussian and has a larger high side tail than low side.

particles at any given depth are large. The second limitation arises from the finite number of photoelectrons produced at the photocathode, which leads to statistical smearing of the signal. The fractional size of this smearing decreases with shower energy. The total resolution for electron showers results from adding the effects of photostatistics and shower fluctuations in quadrature. For blocks with low alphas (low absorbtion coefficients), the average

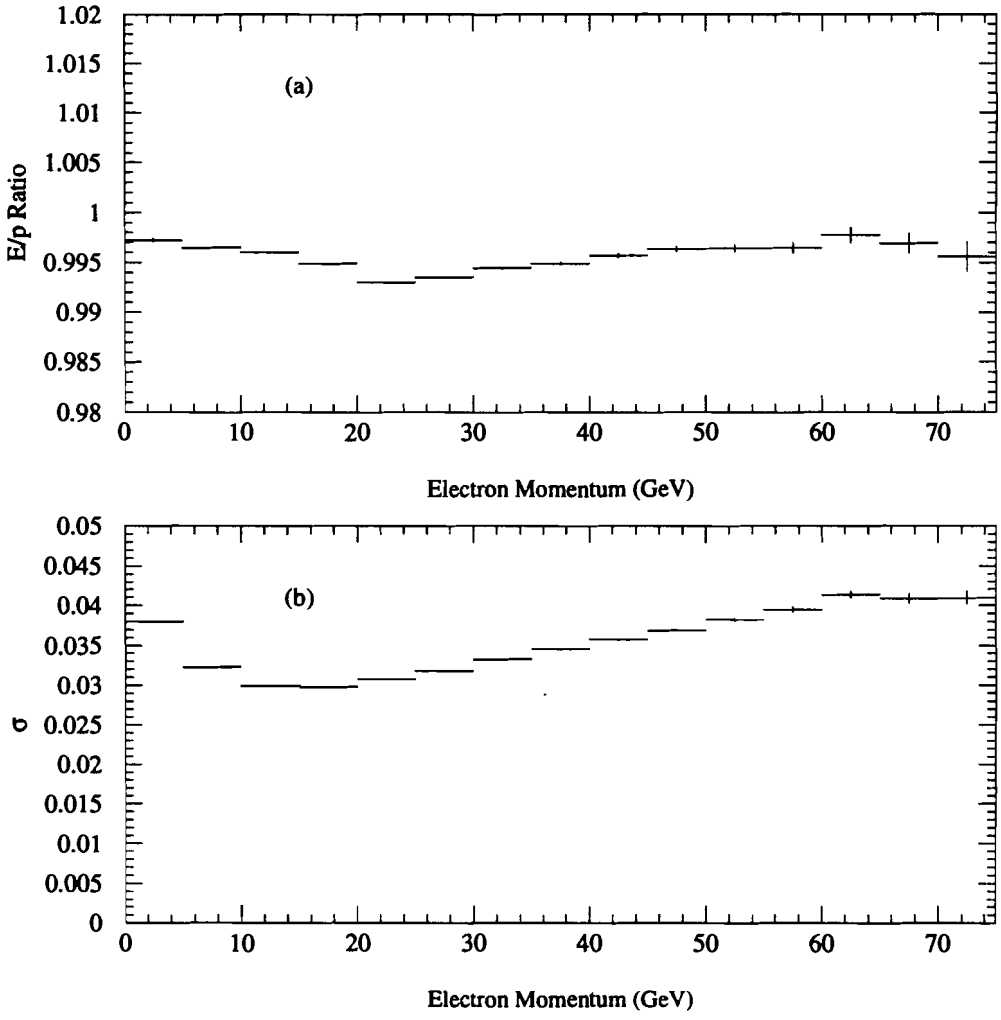

Figure 5.2: The mean and width of the E/p ratio as a function of momentum for the K_{e3} electrons. For these fits, events were restricted to the region near the peak, the apparent shift of the mean away from unity is an artifact of this restriction. (In calibration, the goal is to get the mean E/p to unity. Since the high side tail is larger than the low side tail, the peak is shifted slightly low.)

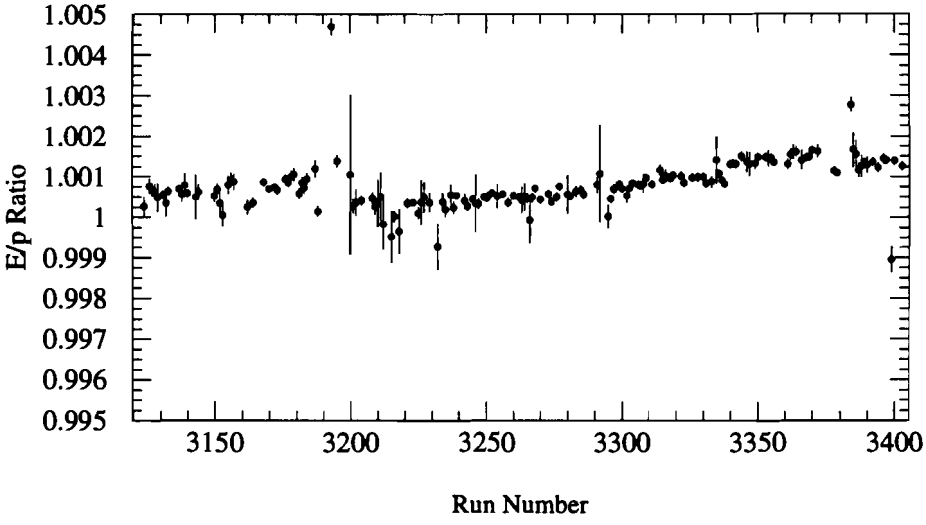

Figure 5.3: The E/p ratio of K_{e3} electrons as a function of run number. The period of time spanned by the plot represents the roughly nine weeks of E773 data collection.

energy resolution for electrons was well described by

$$1.85\% + 3.36\%/\sqrt{E}, \tag{5.1}$$

where the energy, E, was measured in GeV.

Photons travel some depth in the lead glass before converting to an electron-positron pair resulting in more light reaching the photomultiplier. The effect decreases at higher energies, because of extra leakage of shower energy out of the back of the block. Variation in conversion depth degrades

the resolution considerably and though it differed from block to block because of unevenness in the light attenuation of the blocks, the overall photon resolution was about 1% worse.

Finally, the stability of the calibration over time is demonstrated in figure 5.3 which shows the mean E/p as a function of run number. The period of time spanned by the plot is about nine weeks and represents the duration of E773 data collection.

5.3 The Energy Adders

As mentioned above, a small amount of signal from each lead glass block was siphoned off and summed in groups of nine (typically) blocks (fig. 2.8). These "Adder" signals had a short (30 ns) gate, while the Lead Glass had a much longer (150 ns) gate to ensure that the energy deposited was accurately measured. By comparing the signal in the Adder to the nine block sum, one could check the timing of the energy deposition and thereby remove accidental activity in the glass which was almost, but not quite, coincidental with the charged track portion of the event. For a cluster of energy in the Lead Glass to be considered as "in-time" with the event, the ratio of the energy measured by the Adder containing the central block of that cluster to that Adder's nine block sum had to be greater than 75%.

The same electron-positron data used to do the initial calibration of the Lead Glass was also used in calibrating the Lead Glass energy Adders. The goal in this case was to compare the sum of the ADC counts from all of the

blocks contained within the given Adder to the ADC for the Adder itself and to find a gain constant for the Adder to make these two measurements equal. Gain constants for the Adders were determined by plotting the ratio of the two quantities for Adders with blocks hit by calibration electrons. The Adder gains were adjusted so that this ratio was centered at 1.0 for each Adder.

Chapter 6

Analysis

6.1 Selection of the Data

In the offline analysis, the first test of an event was trigger verification based on the hits that were part of the reconstructed tracks. This check confirmed that the event was not written out simply on the basis of accidental hits that might have been recorded coincidentally. This included passing the ZUMA or CHEW logic for path finding within the chambers as well as the trigger hodoscope (B&C banks) and MU2 checks.

Each event was required to have two good tracks of opposite charge and at least one in-time neutral cluster. The χ^2 for each track segment was required to be less than 3×10^{-7} m^2 in both views. (Note that this "χ^2" was not normalized to the expected resolution.) A neutral cluster was one with no associated track. As previously mentioned, while the Lead Glass had a long (150 ns) gate to ensure the accuracy of its measurement, the Adders had a short (30 ns) gate and were used to check the timing of the cluster. Once the Adders were calibrated into units of Lead Glass ADC counts, the ratio of the "energy" in the Adder to that in the Lead Glass had to be greater

than 75% for the cluster to be considered "in-time" with rest of the event.

6.1.1 Fiducial Cuts

Many Fiducial cuts were necessary to assure that the decay products were in a region of the detector where they would be well measured. This was important as a precise understanding of the acceptance is required. The apertures were determined with the high statistics K_{e3} ($K \rightarrow \pi e \nu$) decay mode and then applied to the other analyses.

The VA-0 counter was a limiting aperture for decays occurring just downstream of the UR. The counter was inadvertently placed into the beam line with a small rotation around the z-axis. The edges of the active material were easily located with data, however, since the inner edge of the detector was formed of a thin sheet of inactive aluminum. Hence, it was necessary to cut away from the edges. For decays upstream of VA-0, all three decay products were constrained to the region -0.070$< x <$0.080 m and -0.146$< y <$0.152 m at that z-location.

The DR and its support structure cast a shadow for events in the UR beam decaying upstream of the DR. Events with particles which passed through that mass were less well understood. To keep the event pool clear of such events, it was demanded that the tracks and photons from all such events remain on the same side of the horizontal midplane as the UR in the region upstream of the DR.

An additional aperture was formed by the large circular steel flange supporting the vacuum window at the downstream end of the decay volume (at about 159 m). Any particle more than 0.59 m from the centerline (z-axis) was in danger of scattering in that flange and those events were removed.

The helium bag between the first two drift chambers was supported on four sides by an aluminum box. This box was misaligned during part of the first half of the run (the half with the T&V hodoscopes) and it acted to limit the acceptance. Therefore, a cut was made when any decay product had a projected x coordinate less than -0.62 m at a z midway between the two chambers.

The remainder of the aperture cuts concern the location of the tracks at the calorimeter and muon system. These cuts ensured proper measurement of the particles by those detectors which were necessary for particle identification. At the inner edge of the Lead Glass, the CA covered the inner halves of all lead blocks adjacent to the beam holes. Showers in this device were not well measured and particle ID was compromised. In addition, near the edges of the Lead Glass array, significant energy could be lost by portions of the shower exiting the side of the edge block. All particles were required to be within the Lead Glass and more than half a block away from either beam hole and the outer edge of the array.

Finally, the hodoscope behind the steel muon filter (MU2) was large enough to detect most tracks accepted by the rest of the spectrometer. However, a small fraction of the events had tracks extrapolating outside of the instrumented region. The counter bank was 2.54 m (x) by 2.44 m (y) in size.

To allow for the effects of multiple scattering in the steel filter, tracks were required to project within the region ± 1.2 m (x) by ± 1.1 m (y).

6.1.2 Particle ID and Rejection

Next, various sources of backgrounds were identified for rejection. Λ decays in our decay volume came from two sources, the primary target and the regenerators. To search for these Λs, the higher momentum track is assumed to be a proton while the Λ mass and energy are reconstructed. Λs from the primary target which decay in the decay volume were primarily of relatively high energy. To eliminate these events, decays with a reconstructed lambda mass between 1.110 and 1.122 GeV/c, a lambda energy greater than 100 GeV, and a proton to pion momentum ratio greater than 3 were taken out of our sample. The regenerator Λs, on the other hand, have lower energy and a much broader distribution in P_T^2. These events are widely removed by the cut on P_T^2 described below. The Λ mass distribution for the second half of the data is shown (before and after the P_T^2 cut) in figure 6.1.

To eliminate background from $K_{\mu 3}$ ($K \rightarrow \pi \mu \nu$) decays, tracks were required to point within the MU2 hodoscope and to have a momentum greater than 7.0 GeV/c. Above this momentum, muons would have a high probability of surviving the steel muon filter and leave a hit in the hodoscope. To remove K_{e3} ($K \rightarrow \pi e \nu$) decays, the energy of each track as measured by the Lead Glass was compared to the momentum measured in the spectrometer. Tracks with an energy to momentum ratio, E/p, greater than 85% were

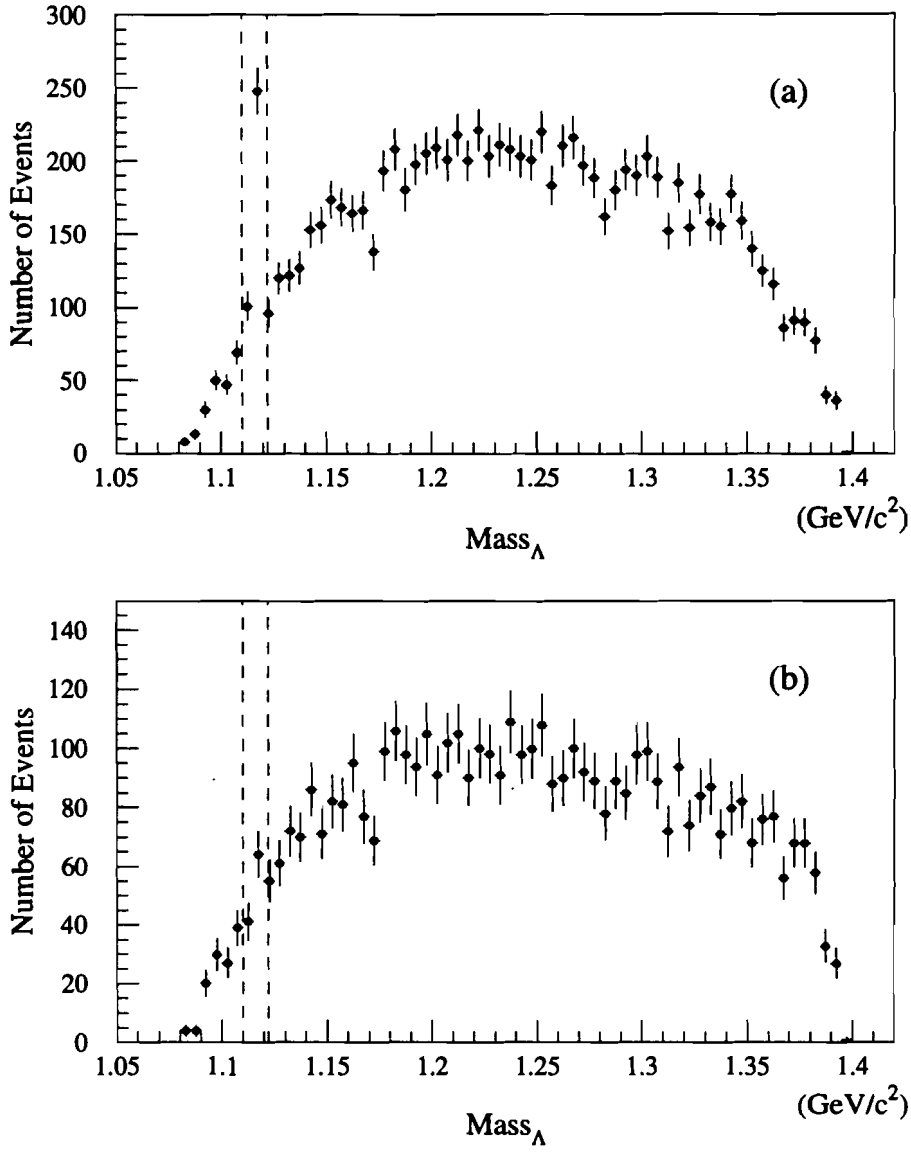

Figure 6.1: The Λ mass distribution is shown (a) after making all cuts except the $M_{\pi\pi\gamma}$ and P_T^2 cuts. Some residual "regenerator Λs" can still be seen between the dashed lines which mark the Λ mass cut. After making the P_T^2 cut, this peak is virtually eliminated (b). A handful of Λs may yet reside there, but not enough to justify cutting all events within that mass region. The number is further reduced after the $M_{\pi\pi\gamma}$ cut is made.

assumed to be electrons.

The Kπ2 ($K \rightarrow \pi^+\pi^-$) mass resolution is about 3 MeV/c^2. Therefore, these events were easily removed by cutting events with a $\pi^+\pi^-$ mass greater than 484 MeV/c^2. To suppress background from Kπ3 ($\pi^+\pi^-\pi^0$) decays, where the two photons fused in the Lead Glass or where one of the photons was lost, a cut was made on the variable:

$$P_{\pi^0}^2 = \frac{\left[(M_K^2 - M_{\pi^0}^2 - M_c^2)^2 - 4M_{\pi^0}^2 M_c^2 - 4M_K^2 \cdot (P_T^2)_c\right]}{4\left[(P_T^2)_c + M_c^2\right]}, \qquad (6.1)$$

where M_c is the invariant mass of the two charged tracks and $(P_T^2)_c$ is their transverse momentum. This quantity is found by assuming that the decay is a kaon going to $\pi^+\pi^-\pi^0$. Using the charged track information (and assuming the kaon and π^0 masses) the square of the longitudinal momentum of the hypothetical π^0 is calculated. For true $K \rightarrow \pi^+\pi^-\pi^0$ events, this must be non-negative. [29, 30] To accommodate resolution effects, events with $P_{\pi^0}^2 >$ –0.01125 were cut. Events with $P_{\pi^0}^2 <$ -0.025 were also cut as these events were largely found to reconstruct with high mass. Figure 6.2 shows the distribution of the data in the $(M_{\pi\pi\gamma}, P_{\pi^0}^2)$ plane. In this plot, an artificial ceiling at 1500 events has been imposed so that the scattered $\pi^+\pi^-\pi^0$ events in the lower right could be more easily seen. Figure 6.3 shows the same distribution for the DE and IB components of the Monte Carlo.

6.1.3 Kinematic Cuts

As detailed above, the charged mode trigger included a cut on activity in the last couple of planes of scintillator. To further curtail the contamination

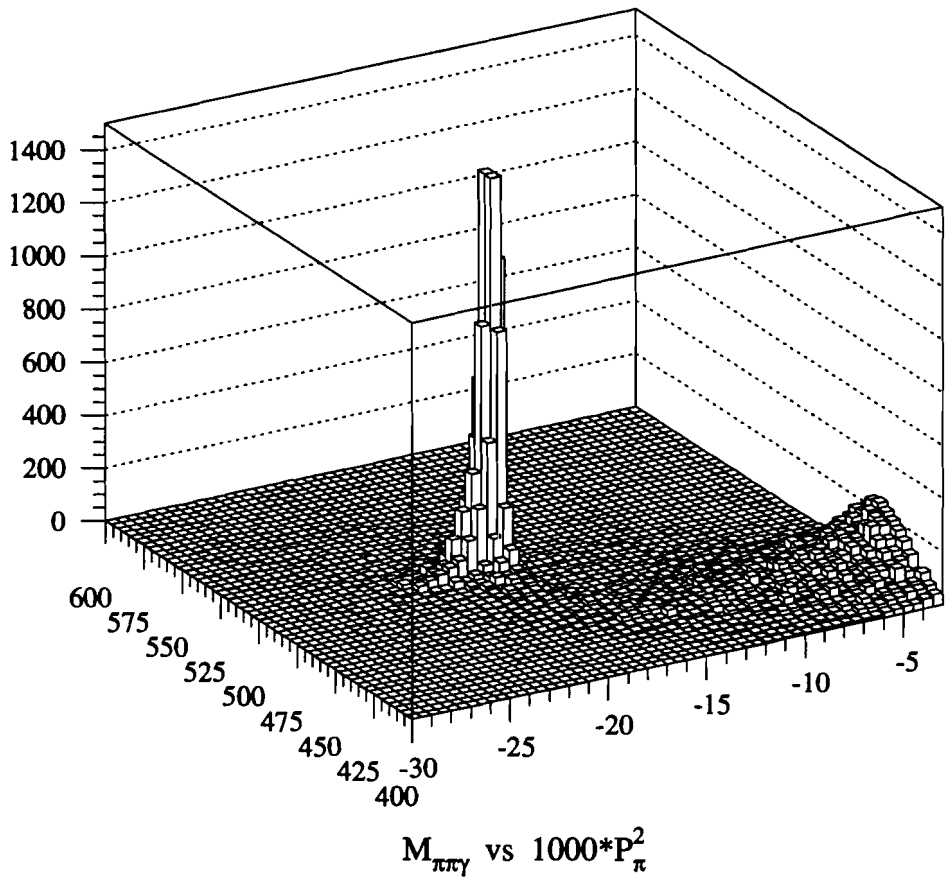

Figure 6.2: The ($M_{\pi\pi\gamma}$, $P^2_{\pi^0}$) distribution of the data. The data is from the second half of the run and not all cuts have yet been made. The $\pi\pi\gamma$ mass is in units of MeV/c^2, while $P^2_{\pi^0}$ is in units of $(GeV/c)^2$. An artificial ceiling at 1500 events has been imposed so that the scattered $\pi^+\pi^-\pi^0$ events in the lower right could be more easily seen.

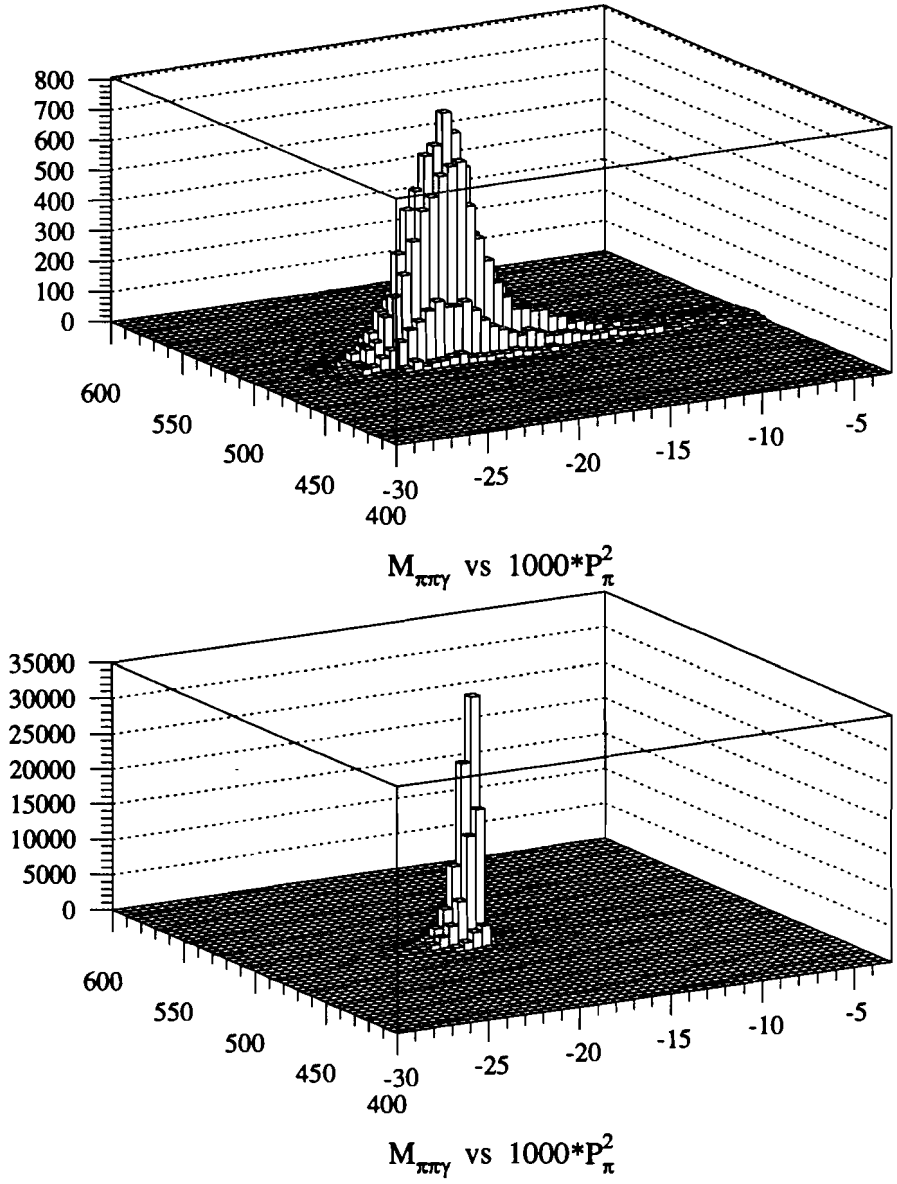

Figure 6.3: The $(M_{\pi\pi\gamma}, P^2_{\pi^0})$ distribution of the Monte Carlo. The top plot is the distribution of the DE events and the IB events are below. The Monte Carlo is from the second half of the run and not all cuts have yet been made. The $\pi^+\pi^-\gamma$ mass is in units of MeV/c^2, while $P^2_{\pi^0}$ is in units of $(GeV/c)^2$. Note the different distributions and scales.

of the data set by diffractive and inelastic scattered kaons which could decay to $\pi^+\pi^-\gamma$, a cut was made on regenerator activity beyond the trigger level. The sum of activity from all photomultipliers on a regenerator was formed and events were excluded if the DR had more than 0.2 or the UR had more than 0.8 muon equivalents of activity.

Each neutral cluster was paired on a trial basis with the charged tracks. Of those trials that remained after passing all cuts, the one which reconstructed with the best $\pi\pi\gamma$ mass was selected. The neutral cluster was required to deposit a minimum energy of at least 1.5 GeV in the Lead Glass (0.5 GeV above the cluster finding threshold). In the center of mass of the decay, this photon was compelled to have an energy greater than 20 MeV. This latter requisite had the twofold effect of excluding events where the acceptance was turning off sharply and of tying our data to the E731 measurements of Ramberg *et al.* [19] The acceptance is turning over quickly below 20 MeV due to intrusion by the $\pi^+\pi^-$ mass cut as can be seen in figure 6.4. This figure shows the $(E(\gamma)_{CM}, M_{\pi^+\pi^-})$ distribution from a small subset of the data before many of the final cuts were made. The connection to E731 allows the use of the $K_S \rightarrow \pi^+\pi^-\gamma$ branching ratio and the K_L DE/IB ratio which were measured there.

The reconstructed energy of kaons decaying within our decay volume peaks at about 68 GeV and drops off more steeply in the direction of lower energies. Kaons between 25 and 155 GeV were used for fitting. The z regions of the decay volume used in the fit depended upon the subset with regenerator location setting the limit at one end of the decay volume and the

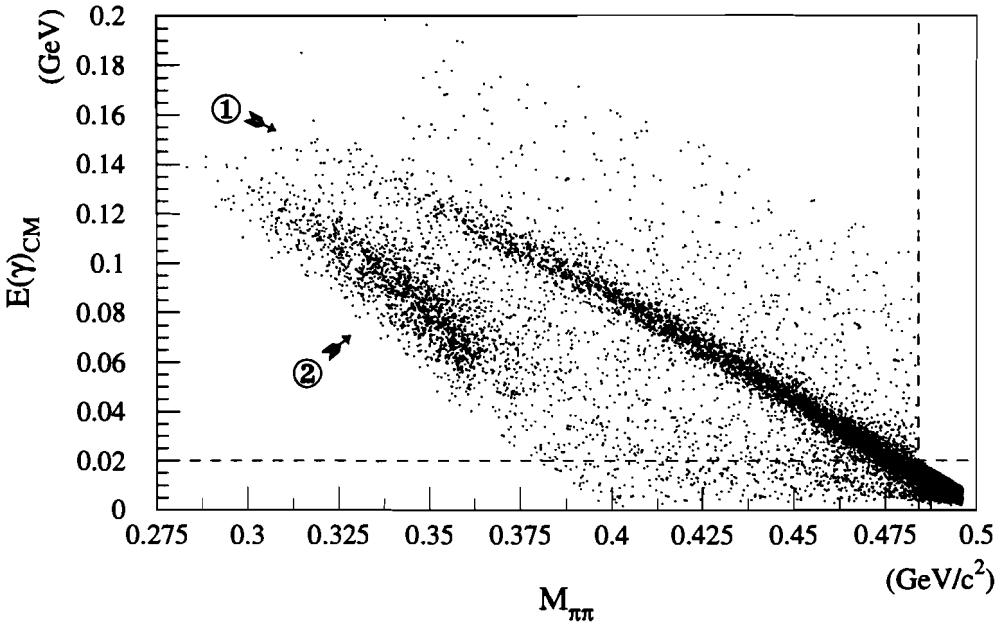

Figure 6.4: The $(E(\gamma)_{CM}, M_{\pi^+\pi^-})$ distribution of the data. $K\pi 2$ $(\pi^+\pi^-)$ events reside primarily in the lower right of the plot, however most have already been removed by a cuts on $E(\gamma)_{CM}$ and $M_{\pi^+\pi^-}$. Other features on the plot are (1) the band diagonally crossing the plot, these are the $\pi^+\pi^-\gamma$ events, and (2) the darkened region below the $\pi^+\pi^-\gamma$ band which are $\pi^+\pi^-\pi^0$ decays. The dashed lines mark the final cuts which were made.

T&V trigger hodoscope or vacuum window setting the other. In addition, the vacuum windows caused bremsstrahlung and mass smearing so decays were also required to occur at least 3 cm away from them. The regions fit are listed in table 6.1. For UR decays upstream of the DR, the regions around the two windows at the DR were also excluded.

Finally, to select coherently regenerated $\pi^+\pi^-\gamma$ decays, each event was

Decay Volume		
	With T&V	Without T&V
Upstream Regenerator	117.33< z <139.33 m	117.33< z <157.33 m
Downstream Regenerator	128.63< z <140.63 m	128.63< z <158.63 m

Table 6.1: The allowed decay volume for $\pi^+\pi^-\gamma$ events to be included in fitting

required to have a total reconstructed mass between 484 and 512 MeV/c^2 and the square of the measured momentum component transverse to the incident kaon's direction (P_T^2) was required to be less than 150 (MeV/c)^2. This is a tight cut on P_T^2, however for this data, the region between 150 and 250 (MeV/c)^2 contains roughly equal contributions from coherent decays to $\pi^+\pi^-\gamma$ and the various backgrounds.

6.2 The Data

The data separated naturally into four subsets, one set for each of the two regenerators and two sets in time to mark the removal of the pair of scintillator planes (the T&V hodoscopes) which determined the end of the decay volume for the first half of the run. After analysis, 9,045 $\pi^+\pi^-\gamma$ decays were found. The data is split roughly half and half between the first and second halves of the run and comes mostly (roughly 75%) from the Upstream Regenerator.

The distribution of events is shown in table 6.2. The events for each subset were put into separate (p, z) distributions with bins 10 GeV/c by 2 m

Distribution of Events			
	With T&V	Without T&V	Whole Run
Upstream Regenerator	3,511	3,437	6,948
Downstream Regenerator	960	1,137	2,097
Both Regenerators	4,471	4,547	9,045

Table 6.2: Data surviving after all cuts

wide for fitting. The momentum bins were apportioned between 25 and 155 GeV/c for all four subsets, while the zone of interest in the decay volume was different for each. Each subset had z bins starting just downstream of the vacuum window downstream of its regenerator and continuing further downstream as far as possible with two meter bins completely contained within the decay volume.

6.3 Background

Two questions needed to be answered about the background. The first being what is the level or quantity of background events underneath the signal. The second question is what is the distribution of these background events in (p, z) space. This distribution is important since this is the space in which final fitting is done.

The $(M_{\pi\pi\gamma}, P_T^2)$ distribution of events which had passed all cuts (except those on mass and transverse momentum) was used to determine the level of background (See figure 6.5). The events considered were those with $M_{\pi\pi\gamma}$

between 465 and 550 MeV/c^2 and P_T^2 less than 2000 (MeV/c)^2; with the exception of a region slightly larger than, and centered on, the signal box. The reason that this range is not centered on the kaon mass is to exclude the band of scattered $\pi^+\pi^-\pi^0$ decays which eluded our other analysis cuts. Most of these events reconstruct with $M_{\pi\pi\gamma}$ between 420 and 465 MeV/c^2. These events do not come down into the signal box when they are simulated in Monte Carlo and they would only complicate the fit. A region larger than the signal box is excluded from the center in order to keep from being influenced by the tail of the coherent decays to $\pi^+\pi^-\gamma$. (Between 150 and 400 (MeV/c)^2, there is still a significant contribution from from coherent decays.)

For each subset, the ($M_{\pi\pi\gamma}$,P_T^2) distribution was fit simultaneously with a broad gaussian in mass and an exponential in P_T^2. Due to the low statistics, a likelihood fit was performed. The results of one of the fits are shown in figure 6.6. This fit was then used to interpolate into the signal region to estimate what the level of background would be there. The backgrounds were found to be less than 2.5% and the estimates for each subset are listed in table 6.3. As a consistency check, the $M_{\pi\pi\gamma}$ and P_T^2 distributions were also each fit separately. These checks yielded similar results.

The (p, z) shape of the background subtracted was taken from events with a total $\pi\pi\gamma$ mass between 484 and 512 MeV/c^2 and P_T^2 between 400 and 2000 (MeV/c)^2. The (p, z) distribution found from events to the left and right of the signal box in $M_{+-\gamma}$ was the same (within uncertainties) as the distribution of events at high P_T^2. The selected events for each subset

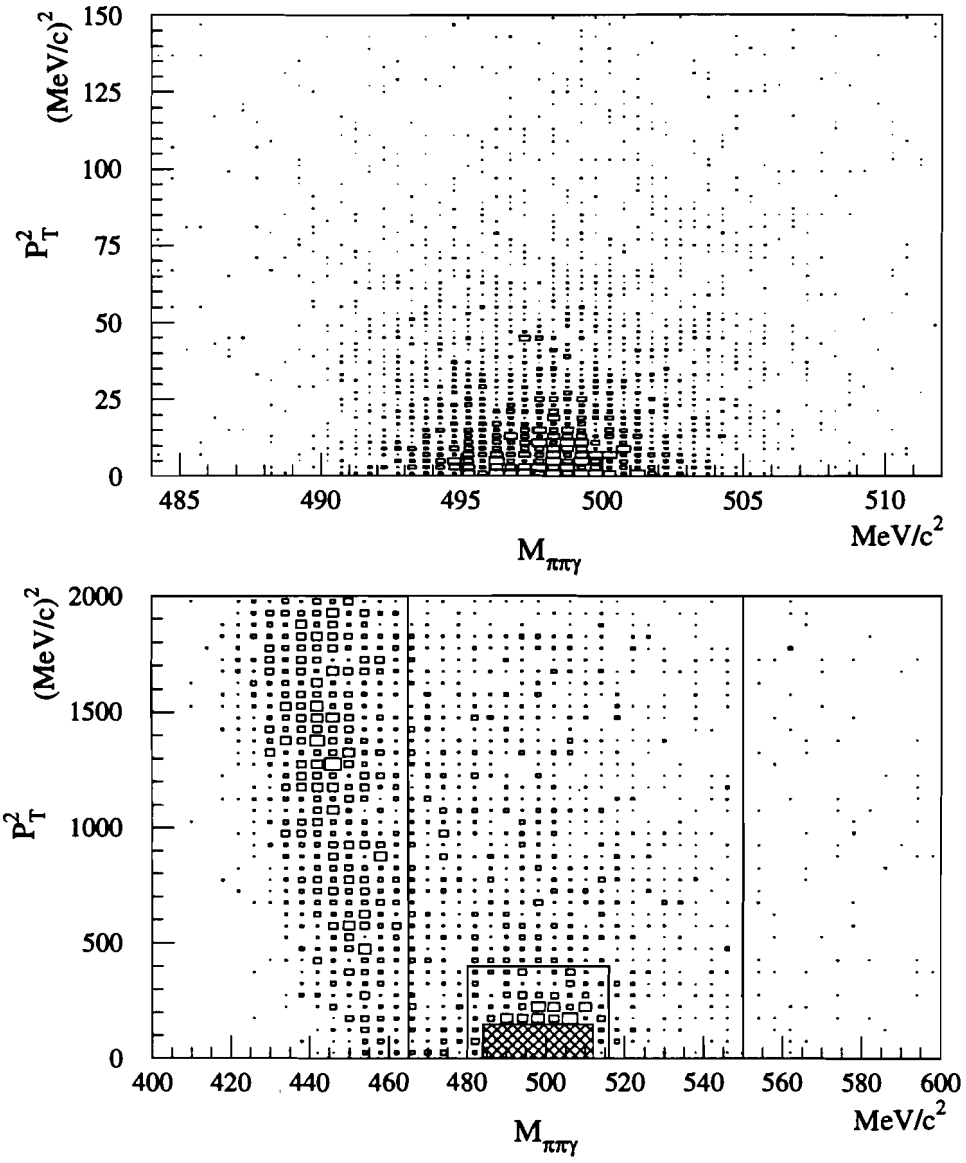

Figure 6.5: The ($M_{\pi^+\pi^-\gamma}$,P_T^2) distribution of the signal and background for the UR, No T&V (second half of the run) data set . Above is the signal distribution, note that it drops off quickly in all directions. Below is the distribution for the background (the signal box is hatched). The lines mark off the region used to fit for the volume/level of the background. To the left of the 465 line are the $\pi^+\pi^-\pi^0$ events. With good mass and high P_T^2 are diffractive and inelastic decays to $\pi^+\pi^-\gamma$. There is also a relatively broad distribution of other (non-$\pi^+\pi^-\gamma$) decays.

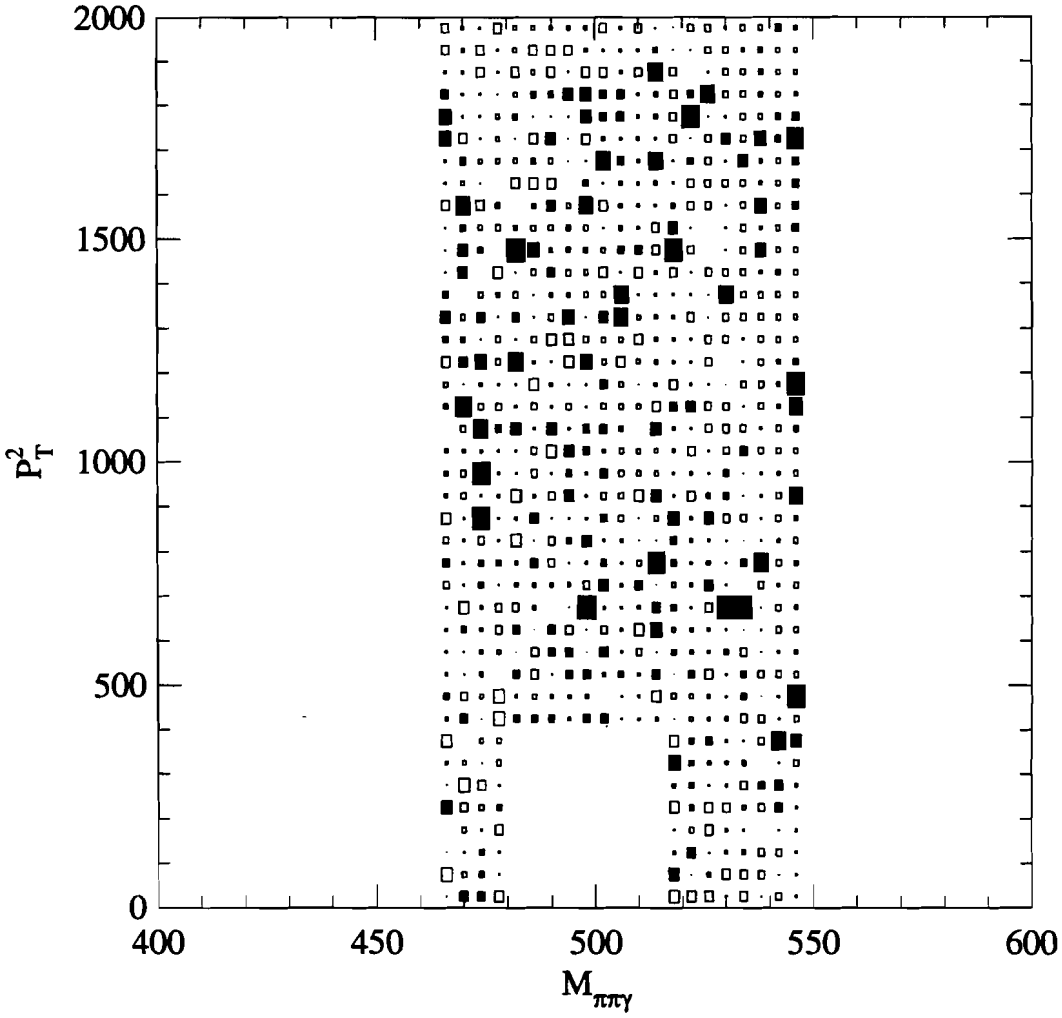

Figure 6.6: The fit (for the UR, No T&V subset of the data) to the ($M_{\pi\pi\gamma}$,P_T^2) background to determine the background volume. The horizontal (vertical) scale is in units of MeV/c (MeV/c)^2. The plot shows the difference between the data and the fit. The box is white (black) when the difference is positive (negative). The area is proportional to the size of that difference. The fit has a χ^2 of 749.1 for 826-4 d.o.f. The relative quality of the fit is also apparent in the flatness of the plot.

Distribution of Events		
	With T&V	Without T&V
Upstream Regenerator	80.5 ± 11.0	76.6 ± 9.1
(as a % of data)	2.3 %	2.2 %
Downstream Regenerator	22.9 ± 5.0	28.9 ± 6.3
(as a % of data)	2.4 %	2.5 %

Table 6.3: Estimate of Background

were plotted in (p, z) binnings identical to those of the signal. This shape was then scaled to the volume/quantity determined by fitting the $(M_{\pi\pi\gamma}, P_T^2)$ distribution and subtracted from the signal before fitting. The fit to the data proved insensitive to the details of the background subtraction.

6.4 Selection of the $\pi^+\pi^-$ Data

The analysis of the $\pi^+\pi^-$ data used many of the same cuts as the $\pi^+\pi^-\gamma$ analysis and has been described elsewhere in great detail. [7] Some minor variation between the two analyses existed, and the differences fell into two categories: those which affected the normalization (and had to be corrected for) and those which were "self-correcting". Some of the differences (such as the cuts on photon energy) were due to the inherent dissimilarity of the two modes, however others are the result of trying to preserve as many events as possible for fitting.

For a difference which affects the normalization, the extent of the change

must be ascertained and a correction, with uncertainties, must be accounted for. Such is the case for the tighter E/p cut (E/p <80% as compared to 85%) used on the tracks in the $\pi^+\pi^-$ analysis. The Monte Carlo does not simulate pion showers in the Lead Glass, so this cut has a different effect on Monte Carlo events and good data. The effect of the difference was measured by changing the cut in the analysis and was observed to be 1.64%. It also introduces an uncertainty in the normalization which is the square root of the difference.

Meanwhile, the differences which are "self-correcting" are so because they affect the data and the Monte Carlo in the same way. An example of this type of cut is the so called "Yswap" cut which the $\pi^+\pi^-$ analysis makes, but the $\pi^+\pi^-\gamma$ analysis does not. This cut removes events where one track fell within the central two columns of the Lead Glass array and the two tracks were within two cm of each in the x dimension. The distribution of particles at the Lead Glass was well modeled by the Monte Carlo and the data and Monte Carlo events should be affected in the same way. Therefore, no correction was necessary.

Another such difference was in the lambda cuts. In the $\pi^+\pi^-$ analysis, all events which reconstructed within 6 MeV/c^2 of the Lambda mass are eliminated. However, as detailed above, in the $\pi^+\pi^-\gamma$ analysis, different cuts were relied upon to remove the target and regenerator Λs. These cuts spare events which happen to reconstruct with the Lambda mass unless they also meet other criteria. There were also differences in the final kinematic cuts of the Kπ2 analysis. All events were kept out to a P_T^2 of 250 MeV/c^2. (For

the $\pi^+\pi^-\gamma$ data, the region between 150 and 250 MeV/c^2 contained roughly equal amounts of coherent decays and background and so was removed.) A slightly broader energy range (20 to 160 GeV) was used in fitting as was a slightly different z decay vertex region (the reconstructed decay vertex was required to lie in the regions 118.5-127 m or 129-154 m for the UR and 130-154 m for the DR). These differences were again well modeled by the Monte Carlo simulation. Therefore, data and Monte Carlo events were affected in the the same manner and no correction was necessary.

After all cuts, 1,130,090 events survived within the signal region. The ($M_{\pi^+\pi^-}$,P_T^2) distribution of events after all cuts except $M_{\pi^+\pi^-}$ and P_T^2 is shown in figure 6.7. In the $K\pi 2$ analysis the quantity of background was estimated by fitting the P_T^2 distributions near the peak, and extrapolating under it. The level of background in the $\pi^+\pi^-$ signal is estimated to be very small; 0.2% (0.6%) for the UR (DR) beam. It was subtracted in the same fashion as described above.

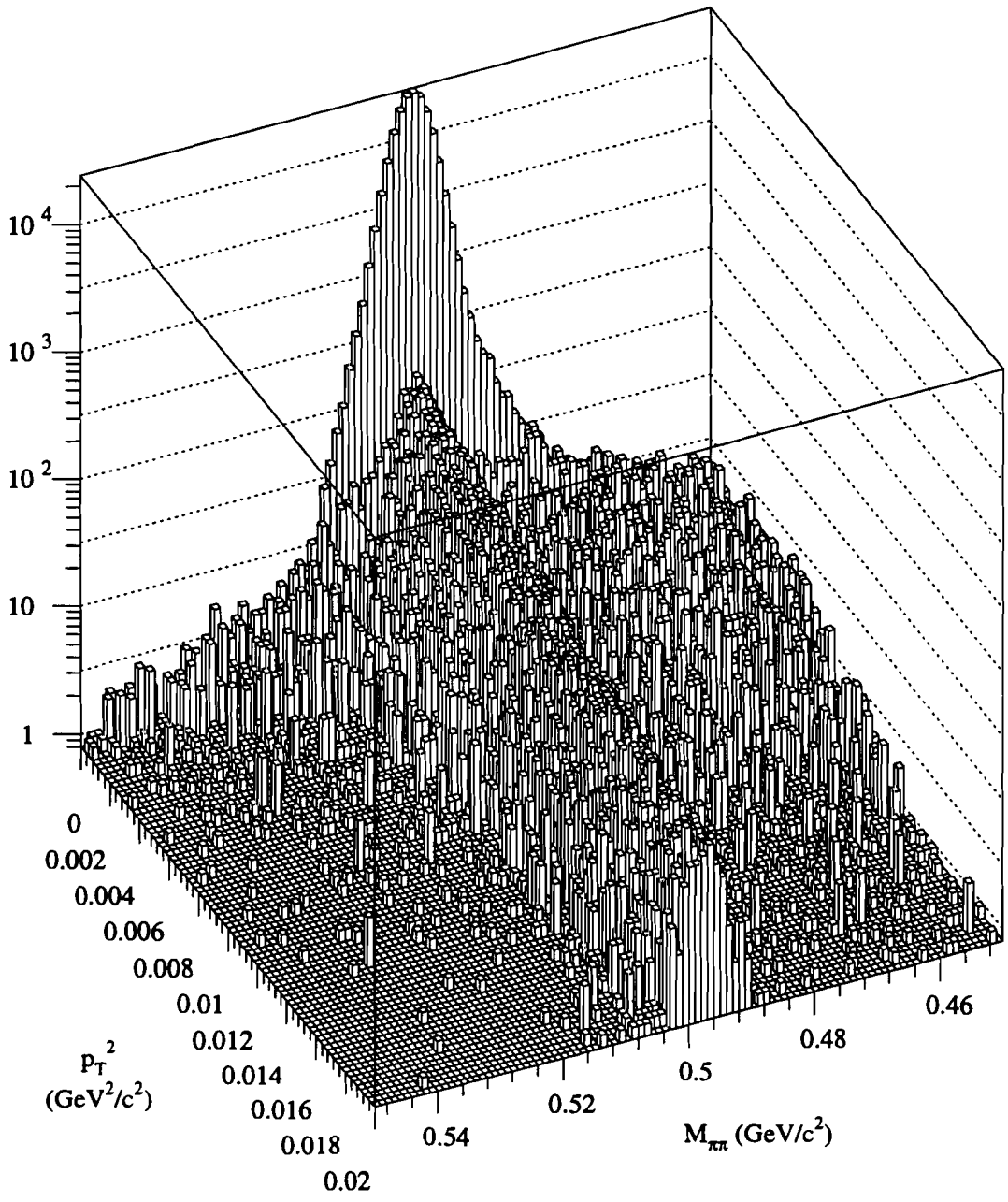

Figure 6.7: The $\pi^+\pi^-$ mass vs. kaon P_T^2 in the $K \to \pi^+\pi^-$ sample; events are from the DR beam of the No T&V data set. The first bin in P_T^2 corresponds to the analysis cut $(0 - 250\ (MeV/c)^2)$ used to select coherent events. Note the large coherent peak and long diffractive tail. A broad distribution of residual K_{e3} $(K \to \pi e \nu)$ decays is also visible.

Chapter 7

Acceptance Correction

In this experiment, the detector acceptance is calculated by a Monte Carlo simulation. The Monte Carlo includes:

- the geometry of the detector,
- the measured efficiencies of the components, and
- the known characteristics of kaon decays.

In this chapter the Monte Carlo is first sketched out and then tested via comparison to the data.

7.1 Kaon Production and Collimation

The first task is to determine the flux of kaons as a function of energy, transverse position, and direction. The correct superposition of K_S and K_L must also be maintained as the kaon evolves after production.

Starting from the protons on the Beryllium target, the kaons are assumed to be produced according to a "Malensek Spectrum" [33, 36]. The "Malensek Spectrum" describes the production of K^+ and K^- by 400 GeV/c protons

on Beryllium. In the Monte Carlo, $K^0/\overline{K^0}$ production is related to that of the K^+ and K^- by quark-counting arguments which yield:

$$N_{K^0} = (N_{K^+} + N_{K^-})/2 \quad (7.1)$$

$$N_{\overline{K^0}} = N_{K^-}. \quad (7.2)$$

A small correction to this spectrum was obtained by E731 [34] through the study of unscattered $K_L \to \pi^+\pi^-$ decays. That correction function is

$$1 + a_1 p + a_2 p^2 + a_3 p^3 + a_4 p^4, \quad (7.3)$$

where

$$a_1 = 6.03315 \times 10^{-3},$$

$$a_2 = -4.28304 \times 10^{-6},$$

$$a_3 = -1.01624 \times 10^{-7}, \text{ and}$$

$$a_4 = 1.80224 \times 10^{-10}.$$

This function is used as a multiplicative correction to the Malensek parameterization and only the dependence of the flux on kaon's momentum is changed. The correction is assumed to be the same for K^0 and $\overline{K^0}$. The beams striking the regenerators are almost purely K_L beams, the flux of which is proportional to the sum of K^0 and $\overline{K^0}$ production. Absorption of the primary proton is included when choosing the z of production.

Once the kaons are produced, they must still propagate through the remainder of the target, the beam absorbers, and collimators. Aside from these objects, most of the flight path of the kaons to the regenerator is in vacuum

(with a short distance of air at the outset). As the kaon states propagate, they decay as well as undergo absorption and transmission regeneration in any material. These effects are easily treated with a transfer-matrix method. Here a matrix is used to describe the evolution of the kaon through any fixed arrangement of material. In the K_L-K_S basis, we write

$$\begin{pmatrix} a'_S \\ a'_L \end{pmatrix} = \begin{pmatrix} T_{SS} & T_{SL} \\ T_{LS} & T_{LL} \end{pmatrix} \begin{pmatrix} a_S \\ a_L \end{pmatrix}, \tag{7.4}$$

where the initial state characterized by the (K_S, K_L) amplitudes (a_S, a_L) is transformed into the final state characterized by the amplitudes (a'_S, a'_L). The transfer matrix, T, is diagonal for vacuum propagation. However, in the presence of material, the off-diagonal elements are non-zero and describe regeneration. The matrix is also energy-dependent.

Since the beam spot is smaller than the target, as is the target length times the production angle, the bulk of the kaons traverse the remainder of the target fully (as opposed to exiting the side). The absorption and transmission regeneration of the exiting kaon are treated with a transfer matrix. No finite-angle scattering is included; since the production spectrum is adjusted to match the data, this scattering can be effectively treated as smearing in the production itself.

The absorption and transmission regeneration in the common and movable absorbers are also treated with the transfer matrix technique. In addition, the absorbers also cause a large amount of elastic scattering. This scattering is very forward-peaked, and many of the scattered particles remain in the beam. Since the mean P_T^2 of scattering is roughly constant with

energy, the mean angle of scattering varies with kaon energy. This causes the fraction of the events staying within the beam to be energy-dependent and hence affects the kaon spectrum seen at the regenerators. Only single elastic scatters are simulated. Double elastic scatters are less frequent by an order of magnitude and are ignored as are inelastic interactions.

The final complication arises from the edges of the steel collimator jaws. There are three regimes of interaction possible. Particles not hitting the jaws at all are simply evolved in vacuum. Particles which encounter the full length of the collimators, about 7 interaction lengths, are treated as completely absorbed. The remaining case involves particles at grazing incidence on the collimator faces; this occurs mostly due to imperfect alignment of the collimators.

For the grazing particles, the amount of material traversed is calculated and converted into the number of kaon interaction lengths, X. The particles then have one of three fates: a fraction e^{-X} of the particles are transmitted with no interaction, a fraction $\alpha X e^{-X}$ of them are elastic scattered once, and the remainder of the particles are treated as lost.

At the end of E773 data collection, a detailed survey of the collimators was performed. These positions provided an excellent starting point for the Monte Carlo simulation of our kaon beam. As mentioned above, the target can be located in the detector coordinate system quite easily. Unfortunately, the construction of the target pile and dump makes precise surveying of the collimation elements relative to the target very difficult. As a result, small adjustments must be made by comparing data and Monte Carlo beam

profiles.

Using fully-reconstructible events, such as $K \rightarrow \pi^+\pi^-$, one can determine the beam profiles by projecting unscattered events. However, with no vacuum beam available in E773, there are always large tails in the profiles from events where the kaon scatters in the regenerators.

For some elements, there was a noticeable tilt in the collimator edges; thus there was a region where kaons saw only part of the full collimator length. This was due to reliance upon external fiducial marks to adjust the collimator jaws, which were enclosed in a vacuum pipe. The end-of-run survey measured the actual jaws and the observed tilts are used without tuning in our simulation. Such scattering occurs further upstream than the regenerator scattering and is distinguishable by the wider spread in the beam profile tails. A comparison of the data and Monte-Carlo target-to-decay-vertex angles for K_{e3} ($K \rightarrow \pi e \nu$) decays is shown in figure 7.1; the scattering tails are reproduced quite nicely.

The collimator geometry was tuned independently in three data periods to allow for small variations in the positions over time. Originally, the geometry was determined separately for the first and second halves of the run. Later, however, the second half of the run was further split into two segments due to an apparent settling of the floor near the calorimeter. Since the coordinate system is tied to the target and calorimeter, such a settling causes an apparent motion of the collimation elements. The motion is small and is coincident with the movement of a heavy new detector into the beamline area in preparation for E799.

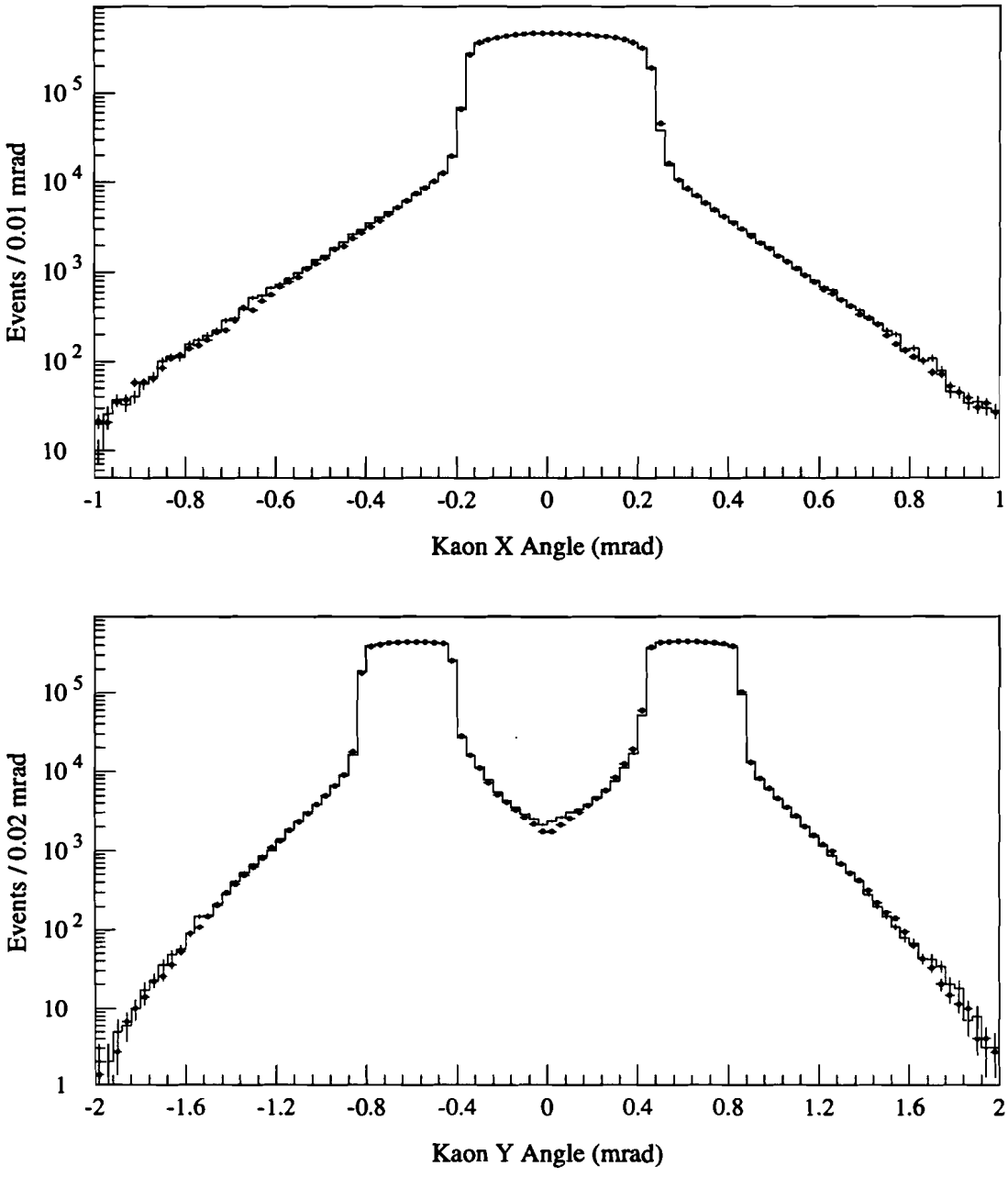

Figure 7.1: The x and y angles of the apparent kaon direction in K_{e3} decays for the UR beam in the second half of the run. The histograms are data and the dots are Monte-Carlo.

Table 7.1: Values of the forward slope parameters describing regenerator scattering. A represents any nucleus.

Scattering	Slope $[(\mathrm{GeV/c})^2]$
Diffraction	
$K_L C \to K_L C$	-58
$K_L C \to K_S C$	-90
$K_L H \to K_L H$	-6
$K_L H \to K_S H$	-8
Inelastic	
$K_L A \to K_S X$ (UR)	-4.9
$K_L A \to K_S X$ (DR)	-6.0

7.2 Kaon Regeneration, Decay

We next discuss the simulation of kaon interactions in the regenerators. The upstream regenerator is treated as a solid block of scintillator with an effective length that includes the contribution from the materials used to wrap the blocks. The downstream regenerator is treated as 12 identical units with 11 uniform gaps. The units have an effective length which includes the wrapping. We note here that the wrappings are a 3% correction to the amount of material for the DR and much smaller for the partially-instrumented UR.

The P_T^2 dependence of scattering is approximated by an exponential, $\exp(-bP_T^2)$ for each particular scattering process. The slopes employed are given in table 7.1. The hydrogen diffractive slopes are taken from the literature; the others are fit to with the $\pi^+\pi^-$ data.

For diffraction, we distinguish regenerative from non-regenerative scattering. We treat single scattering from carbon and hydrogen, and double

scattering where as least one scatter is from carbon. Triple scattering is a small correction and is ignored. We use the same diffractive slope parameters for the UR and DR. The ratio of carbon to hydrogen scattering is taken from the known forward scattering amplitudes. The normalization of the diffractive to coherent events for the UR and DR are separately determined from the data. The normalizations determined from the data are consistent with the expectations calculated from first principles, given the approximations used. The ratio of single to double scattering is approximately that given by the theory, but is adjusted slightly to match the data; the need for this tuning is not surprising, since we have neglected higher-order scatterings.

The key difference with respect to coherent forward regeneration is that regeneration may occur during the finite-angle scattering itself as well as due to the forward propagation before and after scattering. A proper accounting shows that the effective regeneration at finite angle, for single scattering in our relatively short regenerators, is larger than and opposite in phase to the regeneration in the exact forward direction. This leads to dramatic differences in the z distribution of such events as compared to the coherent events in the signal. Thus, despite the small size of the background, it must still be properly accounted for in a precise measurement.

The inelastic slopes are naively expected to be of the order of the kaon-nucleon slopes, since an inelastic process is basically an interaction with a single nucleon in a nucleus. However, the slopes are also affected by the particular vetoes employed by the regenerators, and they also absorb

some the effects of other approximations. For these reasons, the empirically-determined values are different for the UR and DR. We observe no evidence of K_L in the inelastic region; the data are consistent with a pure K_S exponential decay. Although inelastic K_L must exist in principle, the amount is quite small and hence we have ignored such a term. The normalizations of the inelastics for the UR and DR are determined from the data.

In the Monte Carlo, the $K(p^K) \to \pi^+(p^+)\pi^-(p^-)\gamma(q,\varepsilon)$ decay is modeled by a CP-violating E1 IB term and a CP-conserving M1 DE term which do not interfere. The amplitude of the first term, which has a pole at zero energy, is completely predicted by QED in terms of the $K \to \pi^+\pi^-$ amplitude. Its matrix element is:

$$\left(\frac{p^+ \cdot \varepsilon}{p^+ \cdot q} - \frac{p^- \cdot \varepsilon}{p^- \cdot q}\right) \tag{7.5}$$

where $p^\pm$ and q are the $\pi^\pm$ and γ four-momenta, and ε is the photon polarization. In the center-of-mass of the kaon, the IB photon energy falls characteristically as $1/q$. [20]

For the Direct Emission (DE) decays, the matrix element is given by: [26]

$$\epsilon_{\alpha\beta\gamma\delta} p^+_\alpha p^-_\beta q_\gamma \varepsilon_\delta. \tag{7.6}$$

The center-of-mass DE photon energy rises as q^3 before turning over due to phase space limitations. In both cases (DE and IB), events are generated down to a photon center-of-mass energy of 5 MeV. The matrix elements are shown in figure 7.2

The K_L DE to IB ratio, r, was measured by E731. There the $K_S \to$

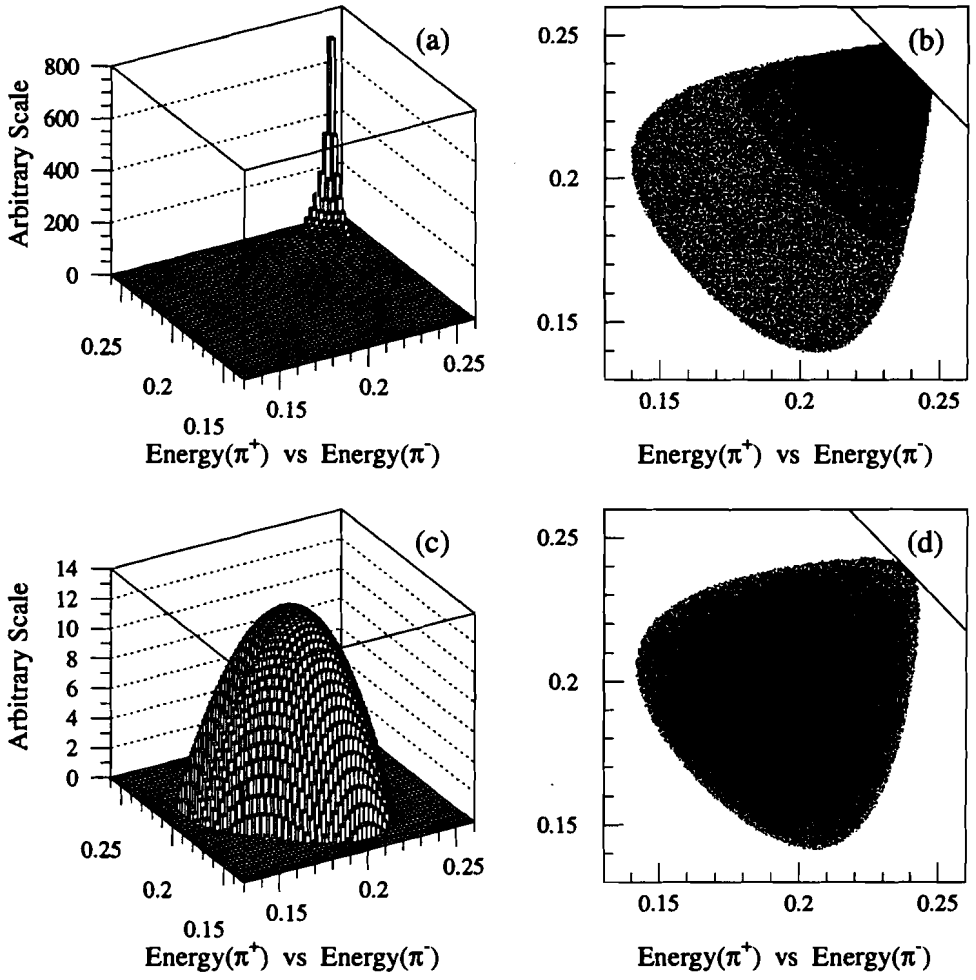

Figure 7.2: The IB and DE matrix element distributions. Figures (a) and (b) show the IB matrix elements as a function of the π^+ and π^- energies, while (c) and (d) show the DE matrix elements. Pion energies are plotted in GeV. Figures (a) and (c) show the distributions generated, down to a center-of-mass photon energy of 5 MeV (however, the binning is much coarser than is actually used in the Monte Carlo). Figures (b) and (d) show the effect of the 20 MeV center-of-mass photon energy cut later imposed.

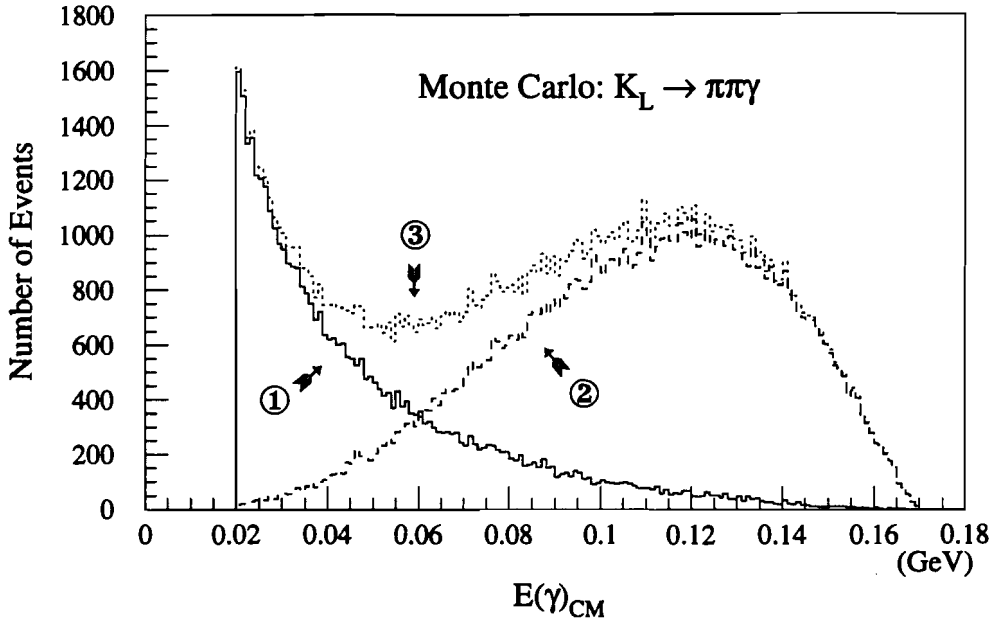

Figure 7.3: The generated DE and IB components of $E(\gamma)_{CM} = q$ for K_L decays; a 20 MeV minimum energy cut has been imposed. The IB spectrum, shown solid (1), falls characteristically as $1/q$. Meanwhile, the DE distribution (dashed, 2) rises as q^3 before turning over due to phase space limitations. Finally, the dotted line (3) is the combination of the two.

$\pi^+\pi^-\gamma$ center of mass photon spectrum was scaled to match the IB peak in the $K_L \rightarrow \pi^+\pi^-\gamma$ center of mass photon energy spectrum. The remaining high energy peak was from the DE contribution (See figure 7.3). Using this method, the IB and DE contributions of the K_L decay were separated and their respective branching ratios found [19]. The Monte Carlo was tuned so that $r = 2.175$ for generated events decaying in the high z region with a minimum photon energy of 20 MeV in the center of mass photon energy.

The $K \rightarrow \pi^+\pi^-$ decay is trivial; the decay axis is randomly chosen in the kaon center-of-mass. After generation, the events are randomly rotated and then boosted from the center-of-mass frame to the lab frame.

Multiple scattering of charged particles in material is included in the simulation. A list of the thicknesses of the relevant detector components is shown in table 7.2. We note that the vacuum window radiation length used is actually too large; the packing fraction of 56% for the Kevlar weave was inadvertently ignored. The correct value is 1.6×10^{-3}. However, the packing fraction was correctly used when treating the regeneration due to the windows. The drift chamber wires are approximated as square in cross section, with the size fixed to give the correct total material. A mean probability of hitting a wire is used, independent of particle trajectory.

The rms multiple scattering angle used is

$$\theta_{rms} = (14.1/p)\sqrt{X_r}\ [\ 1 + (\log_{10} X_r)/9\ ], \tag{7.7}$$

where θ_{rms} is in mrad and p is in GeV/c. X_r is the thickness of the material in radiation lengths. A non-Gaussian tail due to hard scattering is also added; the final distribution is shown in figure 7.4.

Bremsstrahlung from electrons and photon conversions were included in the Monte Carlo and also utilized the data listed in table 7.2. A realistic bremsstrahlung energy spectrum was used; the photons generated were taken to be collinear with the electrons. Conversions were allowed for all photons with energy greater than 0.1 GeV. The electron and positron energies were chosen according to the Bethe-Heitler spectrum; no opening angle was used

Table 7.2: Thickness of sources of scattering in radiation lengths. Air near the vacuum windows (not listed) is also included.

Detector Element	Location (m from Target)	Thickness X_r (Radiation Lengths)
Vacuum Window	117.330	2.50×10^{-3}
Vacuum Window	127.641	2.50×10^{-3}
Vacuum Window	128.623	2.50×10^{-3}
V hodoscope	140.913	3.32×10^{-3}
T hodoscope	140.936	3.30×10^{-3}
Vacuum Window	158.946	2.50×10^{-3}
Drift Chamber 1	159.287	4.31×10^{-3}
Drift Chamber 2	165.861	4.49×10^{-3}
Drift Chamber 3	171.856	4.20×10^{-3}
Drift Chamber 4	176.197	2.34×10^{-3}
Chamber Field Wires[a]	—	5.70×10^{-3}
Chamber Sense Wires[b]	—	6.43×10^{-3}
C Hodoscope	179.502	4.0×10^{-2}
B Hodoscope	179.520	4.0×10^{-2}

[a]This is the average material seen by the 9.9% of tracks, per chamber, which hit a field wire.

[b]This is the average material seen by the 0.7% of tracks, per chamber, which hit a sense wire.

between the tracks.

A particle was considered lost if it left the active detector volume. This meant striking outside the aperture of one of the detector elements or extrapolating outside of the large vacuum window. Particles from UR decays upstream of the DR were also lost if they hit the DR. If any decay products from the decay was lost in tracing, the generation of that event was terminated. Any externally radiated photons, and e^+e^- pairs from their

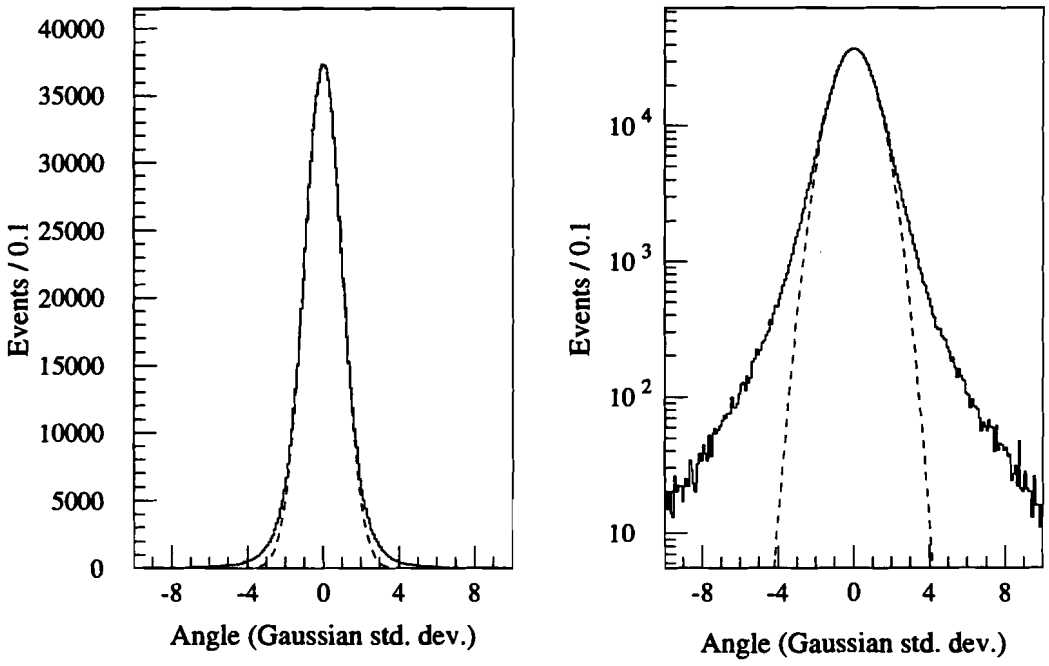

Figure 7.4: The distribution of the multiple scattering angle used in the Monte-Carlo simulation. The angle is normalized to the RMS scattering angle in the Gaussian approximation. The dashed line shows a normal Gaussian for comparison. Both figures show the same curves; the scales are changed for clarity.

conversion, were allowed to be lost without terminating generation. The chance of an accidental track replacing a lost track and successfully forming a good vertex and passing all other cuts, was negligible.

7.3 Detection of the Decay Products

We briefly describe some aspects of the conversion of the physical parameters of the events into detector signals recorded by the experiment.

For the z of each drift chamber plane a particle passed, the transverse position was noted. These positions were then smeared to account for chamber resolution. Next the nearest wire was determined and the wire's efficiency was taken into account. Finally, the drift distance was converted to a drift time using the time-to-distance relation corresponding to the current plane and data run. Wire sag and propagation times in the sense wires are not included in the simulation nor corrected for when analyzing MC. No attempt was made to simulate δ-rays in the MC. This leads to some inconsequential differences in the Monte-Carlo prediction of the mass and P_T^2 resolutions and those in the data.

Hadronic showers from charged pions are not simulated in the Lead Glass. Instead, a fixed energy deposit of 0.7 GeV, corresponding to a minimum-ionizing particle is used. Thus, a cluster is potentially always available for matching to the pion's track. For electromagnetic particles, the energy is smeared according to a parameterization of the resolution function which includes a central Gaussian, and low- and high-side tails. The pattern of energy deposition in a 5×5 array of blocks centered on the struck block was determined with a library of EGS showers. The library includes showers of various energies and incident positions on the block face. The energies in each block are then converted to ADC counts, using the measured gains

from the appropriate calibration, and a readout-threshold is applied. No direct attempt is made to simulate pedestal shifts in the ADCs. The data is not sensitive to these small effects. No attempt is made to simulate the temperature dependence observed in the data; for Monte-Carlo events, no correction is applied during reconstruction.

For each particle traversing the B and C banks, the hit counter, determined using the positions measured from special muon runs, is fired.

For the Mu2 bank, it was not necessary to simulate the particular counter hit. All such hits were from $\pi \rightarrow \mu$ decays in flight; it was sufficient to simulate the trigger veto only. The trigger latch was set if the muon projected to within the boundaries of the counter bank. A very rough treatment of μ scattering in the muon filter steel was implemented.

The latches of the photon veto scintillator detectors were set when particles traversed them. Energy was deposited in the lead-lucite portion of the vetoes. The energy deposits in the photon vetoes were not crucial, since the majority of the lead-lucite counters were not used in the trigger, and none was used in the off-line analysis of the charged triggers.

7.4 Data - Monte Carlo Comparison

It is important to compare the data and Monte Carlo distributions of various parameters in order to test our understanding of the system and hence of the acceptance. As the decay contains both neutral and charged particles, both

aspects of the Monte Carlo must be investigated. Below are some representative histograms, typical of many, which demonstrate that the features of the data are accurately reproduced by the Monte Carlo simulation.

We begin by displaying figure 7.5 which contains two plots; the energy of the photon as measured by the Lead Glass calorimeter and the momentum spectrum of pions measured by the magnetic spectrometer.

Figure 7.6 shows the data/Monte Carlo comparison for the photon energy in the center of mass of the kaon. Note that the acceptance is rapidly turning over below the 20 MeV cut. This is mostly due to the 1.5 GeV cut on photon energy in the lab and the $\pi^+\pi^-$ mass cut (as demonstrated in figure 6.4).

Some of the more important distributions to examine are the kaon energy spectrum and longitudinal (z) decay vertex distribution. This is due to the fact that the actual fitting of the data occurs in the (p,z) space of the decays. Figures 7.7 and 7.8 compare the kaon energy spectrum of the data to that of the Monte Carlo. Meanwhile, figures 7.9 and 7.10 are the comparisons of the decay vertex distributions.

From the comparisons above, it can be seen that the Monte Carlo does a very good job of reproducing the features of the data. However, it is also interesting to look at comparisons involving the $\pi^+\pi^-$ data. This is relevant for two reasons, first this analysis uses the $\pi^+\pi^-$ data for normalization and second it allows a deeper look into the data/Monte Carlo match for the charged portion of the simulation.

Figure 7.11 shows the locations of tracks at the HDRA and the magnet bend plane for the first half of the $\pi^+\pi^-$ data (Data Set 1, with the T&V

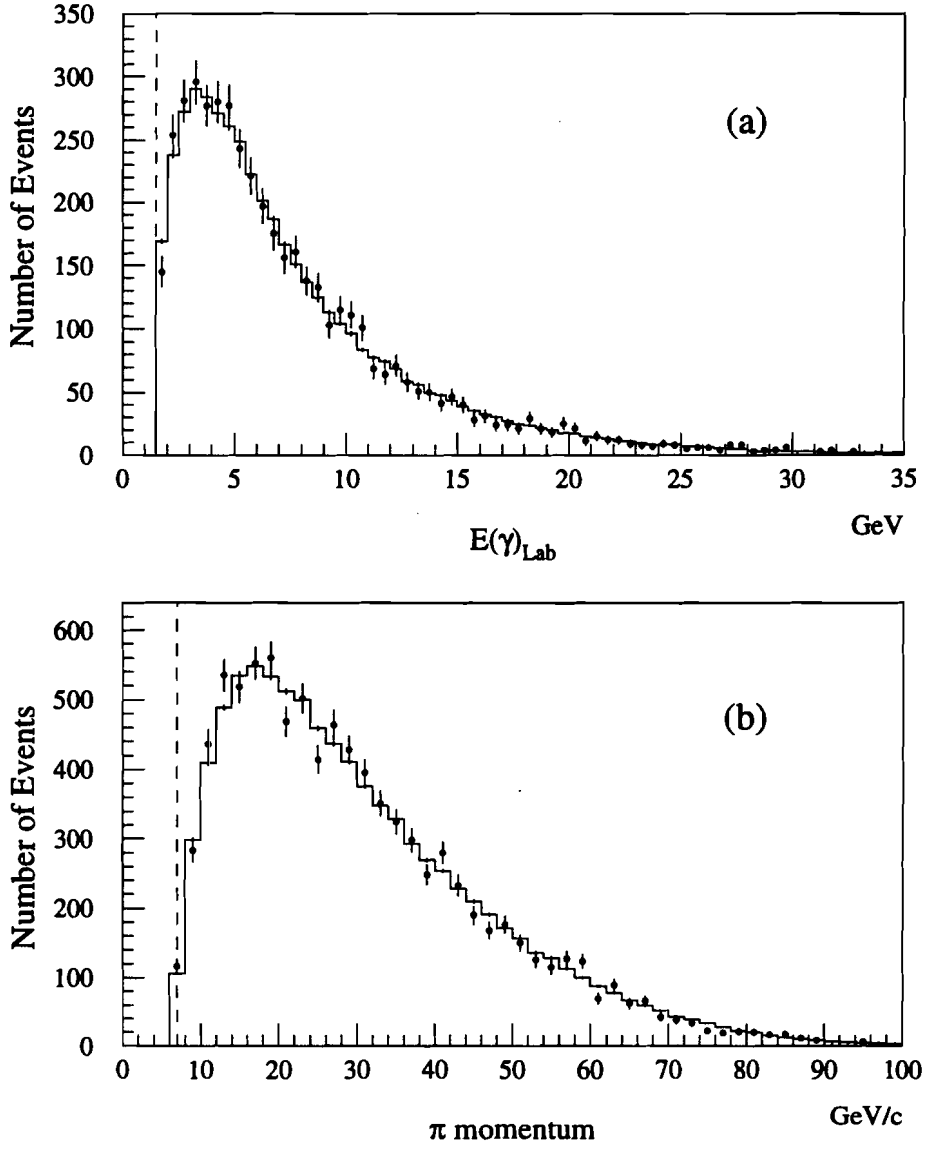

Figure 7.5: Data-Monte Carlo comparisons for $K \to \pi\pi\gamma$ of the measured photon energy and pion momentum. The histograms represent the Monte Carlo, while the data is shown as points. Above (a) is the comparison for the photon energy as measured in the lab for data from the second half of the run (Data Set 2, without the T&V hodoscopes). Below (b) is the comparison for the momentum of the two pions from the same data. The dashed lines mark the cuts made on the variables.

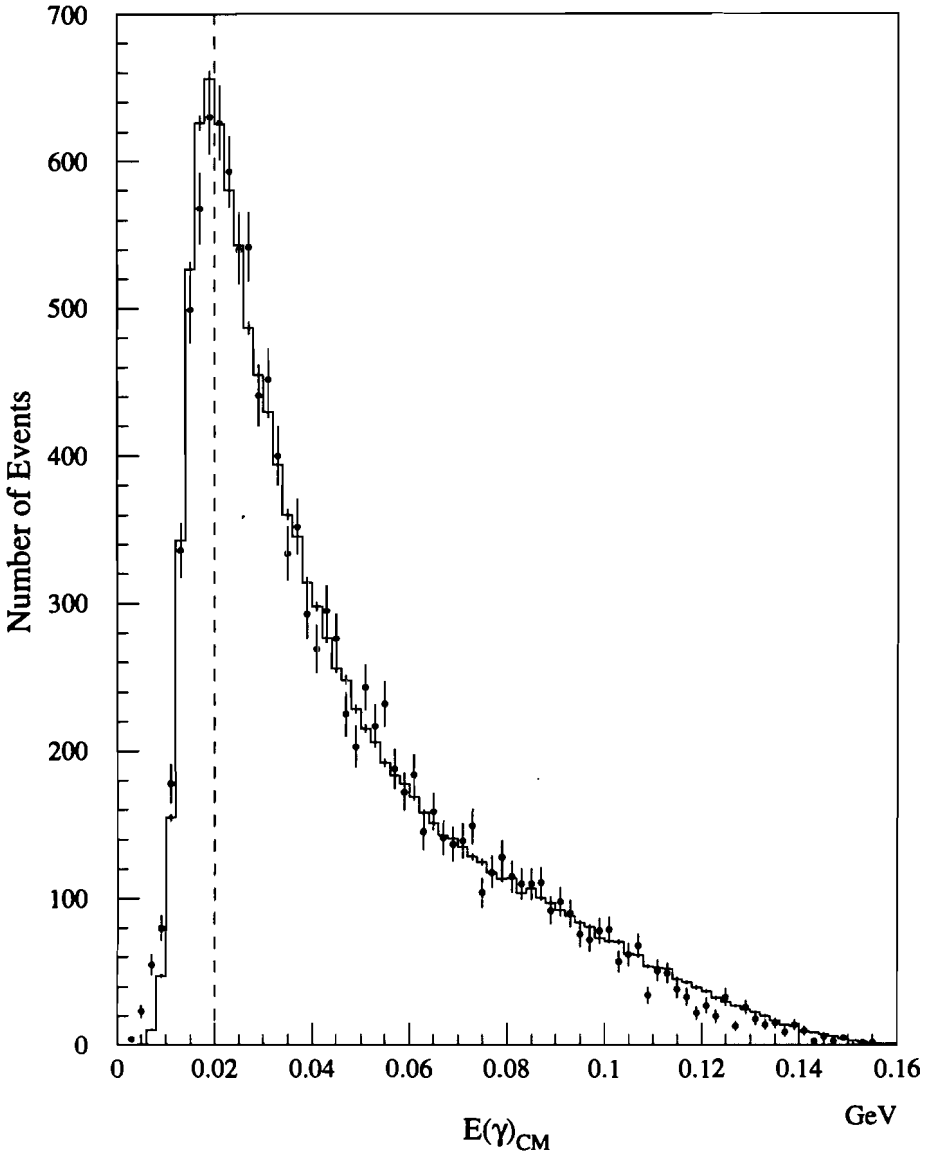

Figure 7.6: The Data-Monte Carlo comparison for $K \rightarrow \pi\pi\gamma$ of the photon energy in the kaon center of mass. The histogram represents the Monte Carlo, while the data is shown as points. and there is a cut at 20 MeV. The dashed lines mark the cuts made on the variables.

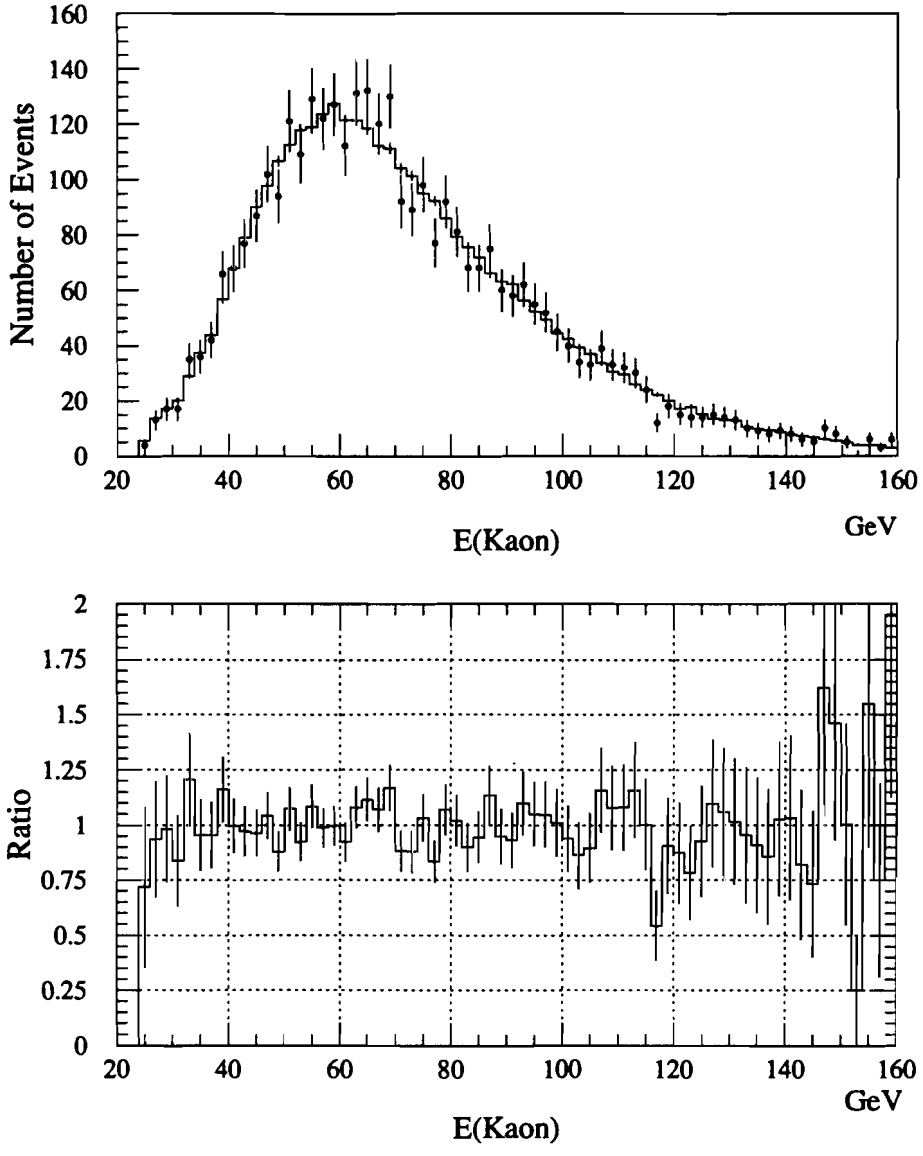

Figure 7.7: The Data-Monte Carlo comparison for $K \rightarrow \pi\pi\gamma$ of the kaon energy (UR, Data Set 2). The histogram represents the Monte Carlo, while the data is shown as points.

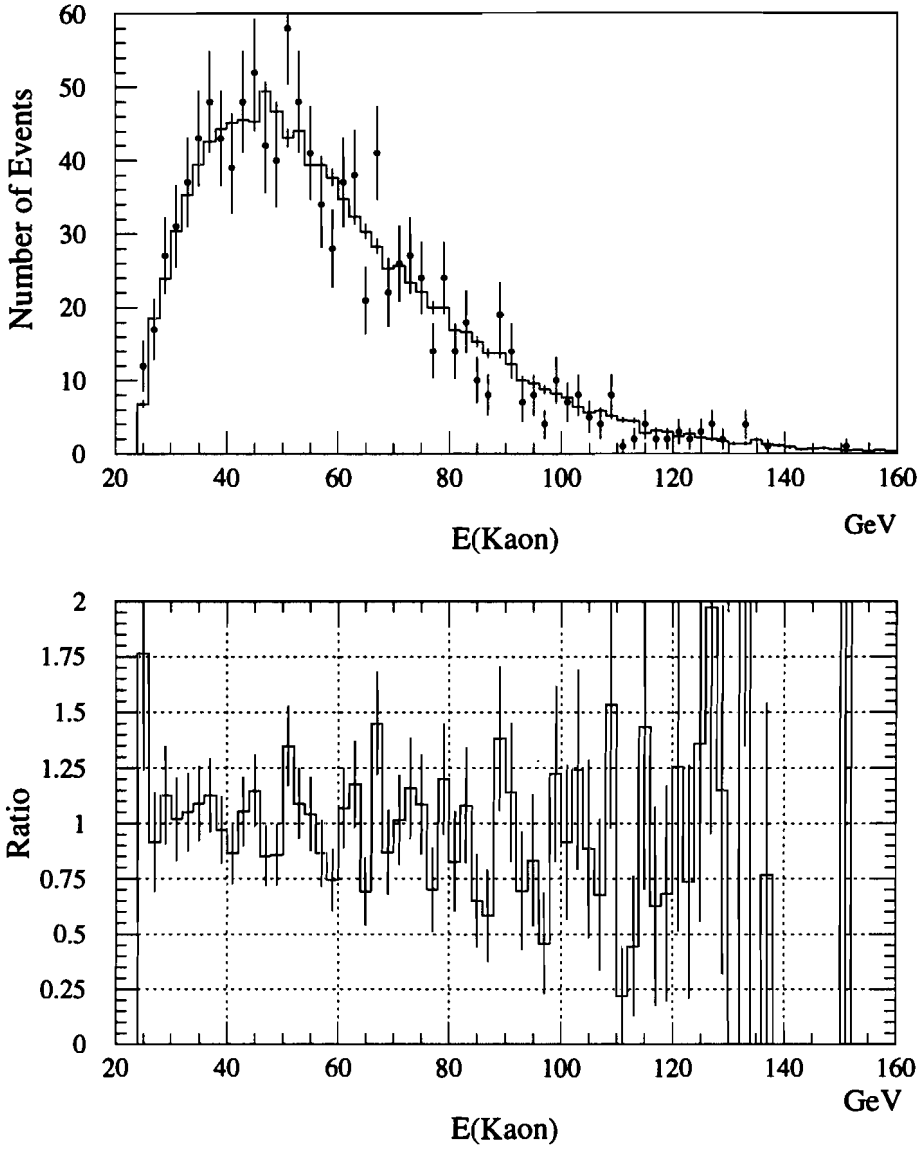

Figure 7.8: The Data-Monte Carlo comparison for $K \rightarrow \pi\pi\gamma$ of the kaon energy (DR, Data Set 2). The histogram represents the Monte Carlo, while the data is shown as points.

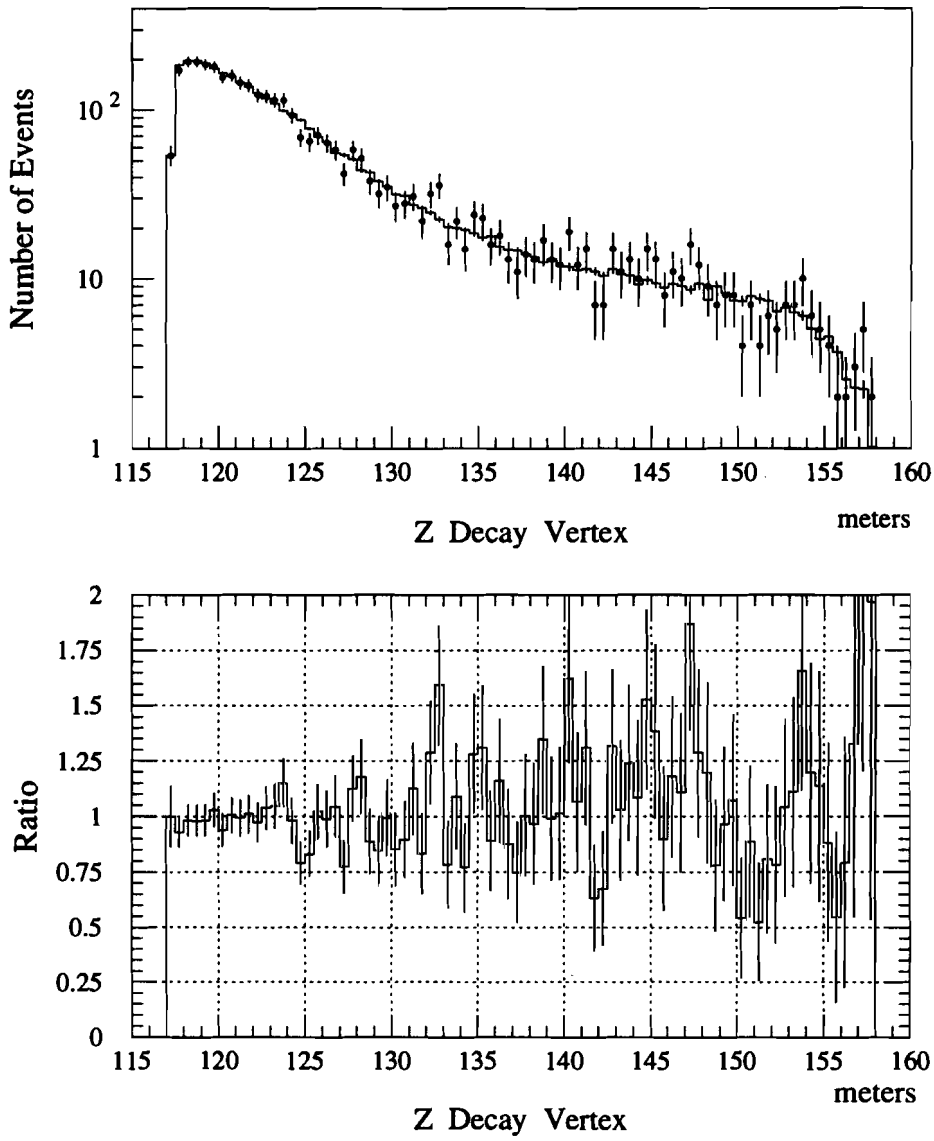

Figure 7.9: The Data-Monte Carlo comparison for $K \rightarrow \pi\pi\gamma$ of the longitudinal kaon decay vertex (UR, Data Set 2). The histogram represents the Monte Carlo, while the data is shown as points.

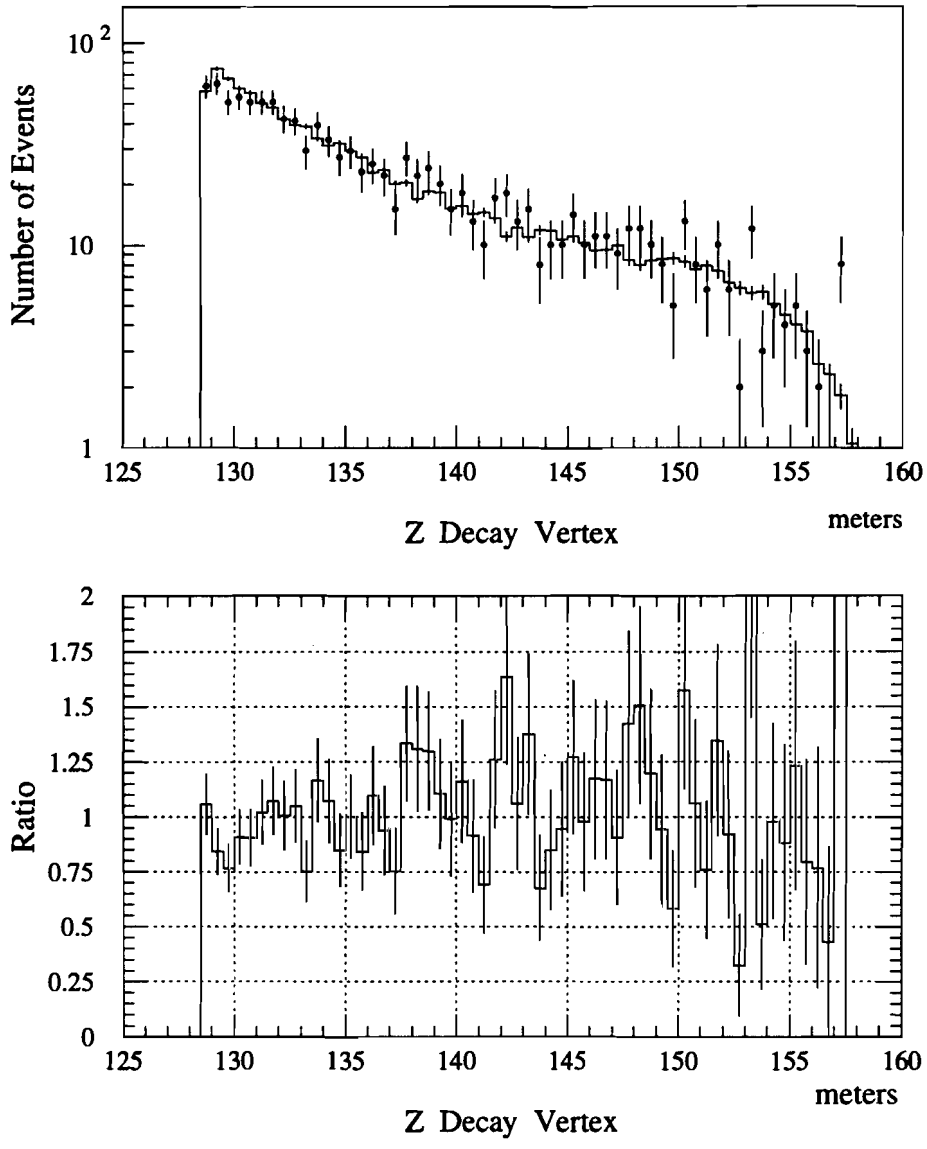

Figure 7.10: The Data-Monte Carlo comparison for $K \rightarrow \pi\pi\gamma$ of the longitudinal kaon decay vertex (DR, Data Set 2). The histogram represents the Monte Carlo, while the data is shown as points.

hodoscopes).

Figure 7.12 shows a comparison of the data and Monte-Carlo kaon energy distributions from the $K \rightarrow \pi^+\pi^-$ decay mode. Figure 7.13 shows the comparison of the data and Monte-Carlo decay vertex distributions from the $K \rightarrow \pi^+\pi^-$ decay mode.

7.5 Accidental Activity

After generation and digitization of a kaon decay, the data could be combined ('overlayed') with that from an accidental event if desired. About 1% of the triggers written to tape were accidentals. This provides a large sample for use in overlays. The effect of accidentals was small, and overlays were done only for special studies.

Accidentals were chosen from the same run being simulated. The trigger bits in the accidental event were examined before the overlay was done. If any signals which were in veto for the trigger being used fired, the accidental was discarded and a new one was read in. This was done to speed up the generation process.

For the drift chambers, the two lists of valid hits were merged. Since the double-pulse resolution of the TDCs was 250 ns, which is longer than the time window for valid hits, the earlier hit was taken in cases were both the generated event and the accidental fired a given wire. This was done before the second level trigger was checked. Accidentals in the chambers

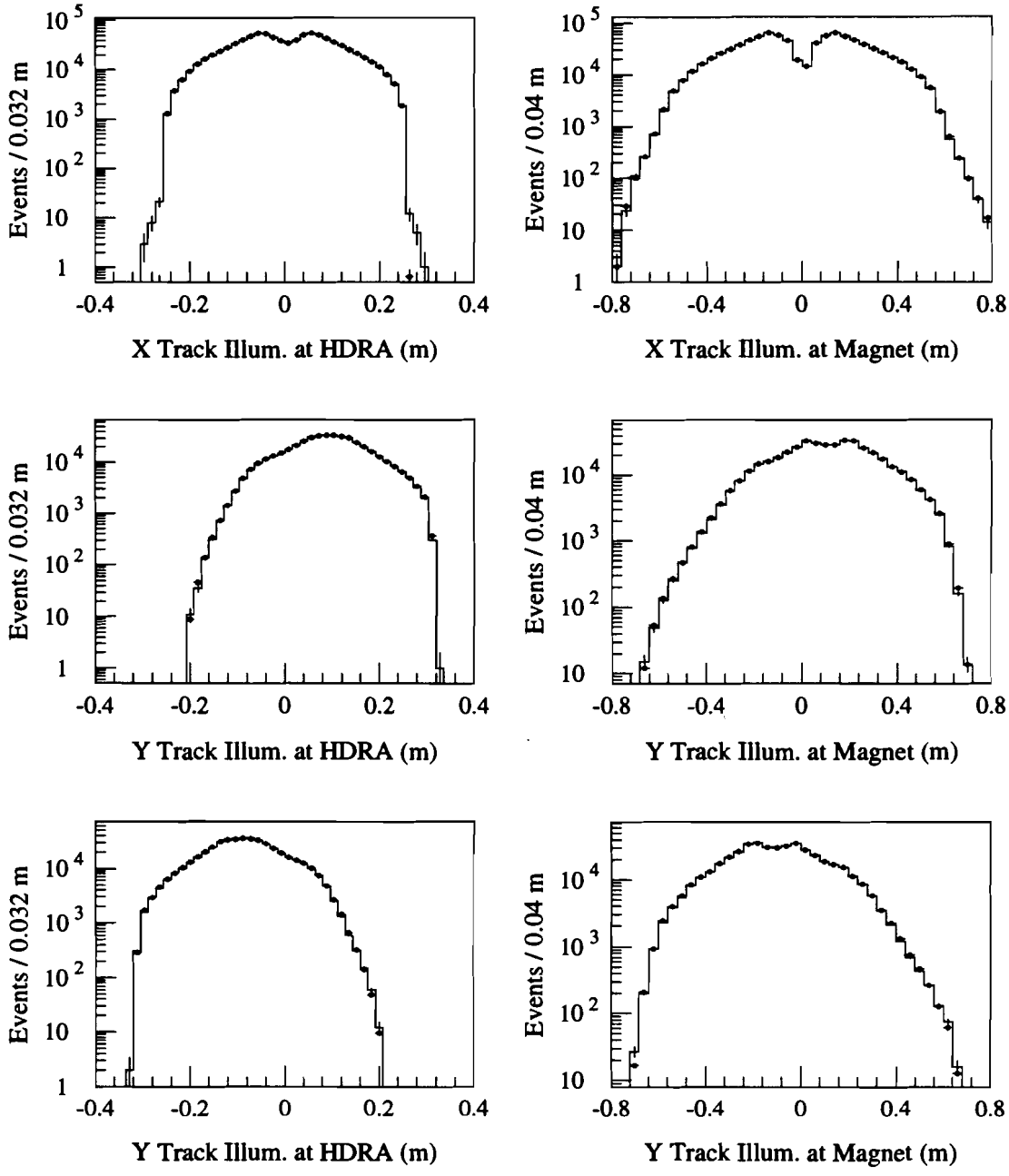

Figure 7.11: Track illuminations for $K \rightarrow \pi^+\pi^-$ from Data Set 1 (with the T&V hodoscopes). The y plots are separated into high and low beams. The data is represented by the histograms, while the dots are Monte Carlo.

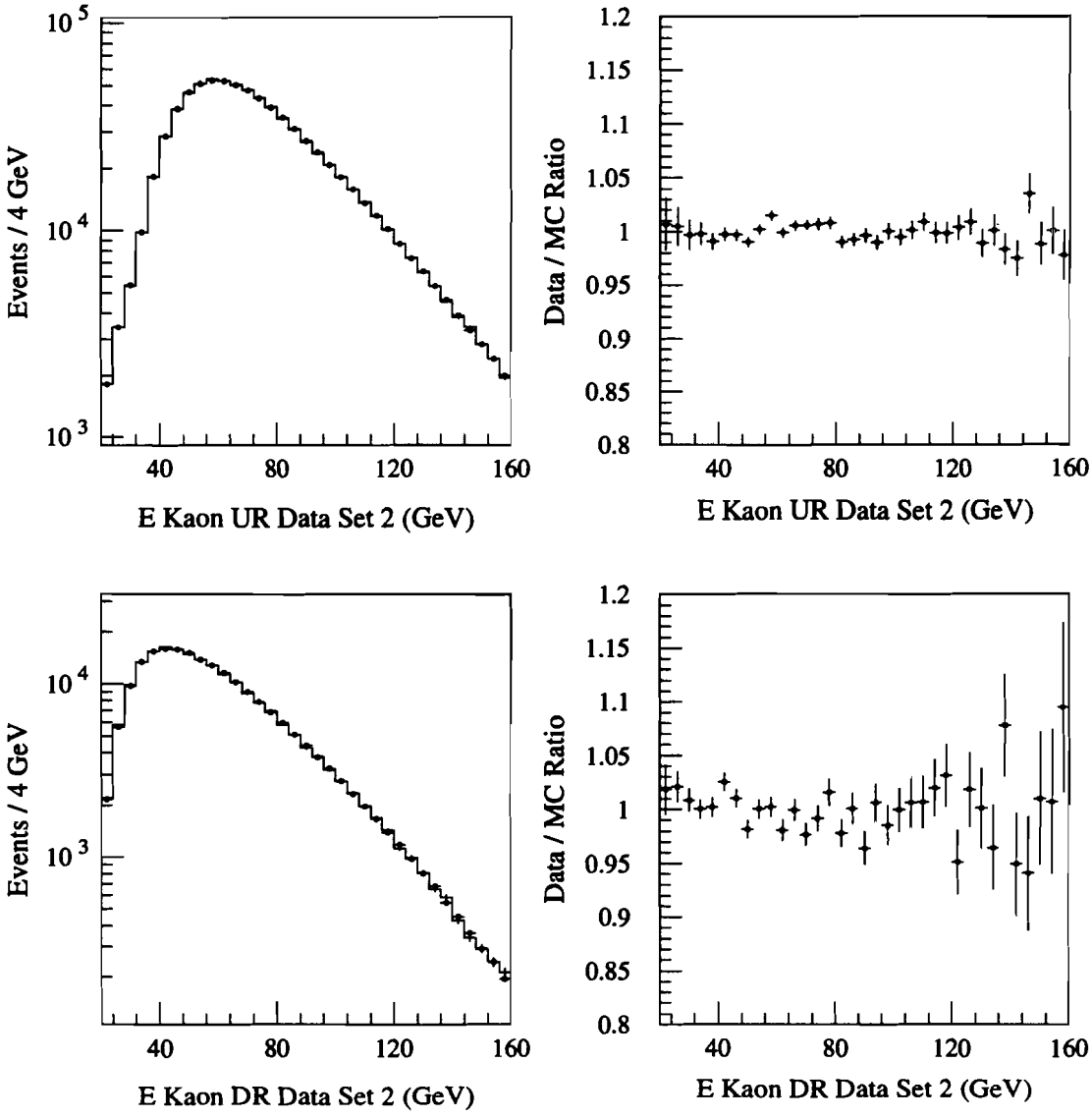

Figure 7.12: A comparison of the data and Monte-Carlo kaon energy distributions for $K \rightarrow \pi^+\pi^-$ decays from Data Set 2 (the second half of the run, without T&V hodoscopes). The histograms are data and the dots are Monte Carlo.

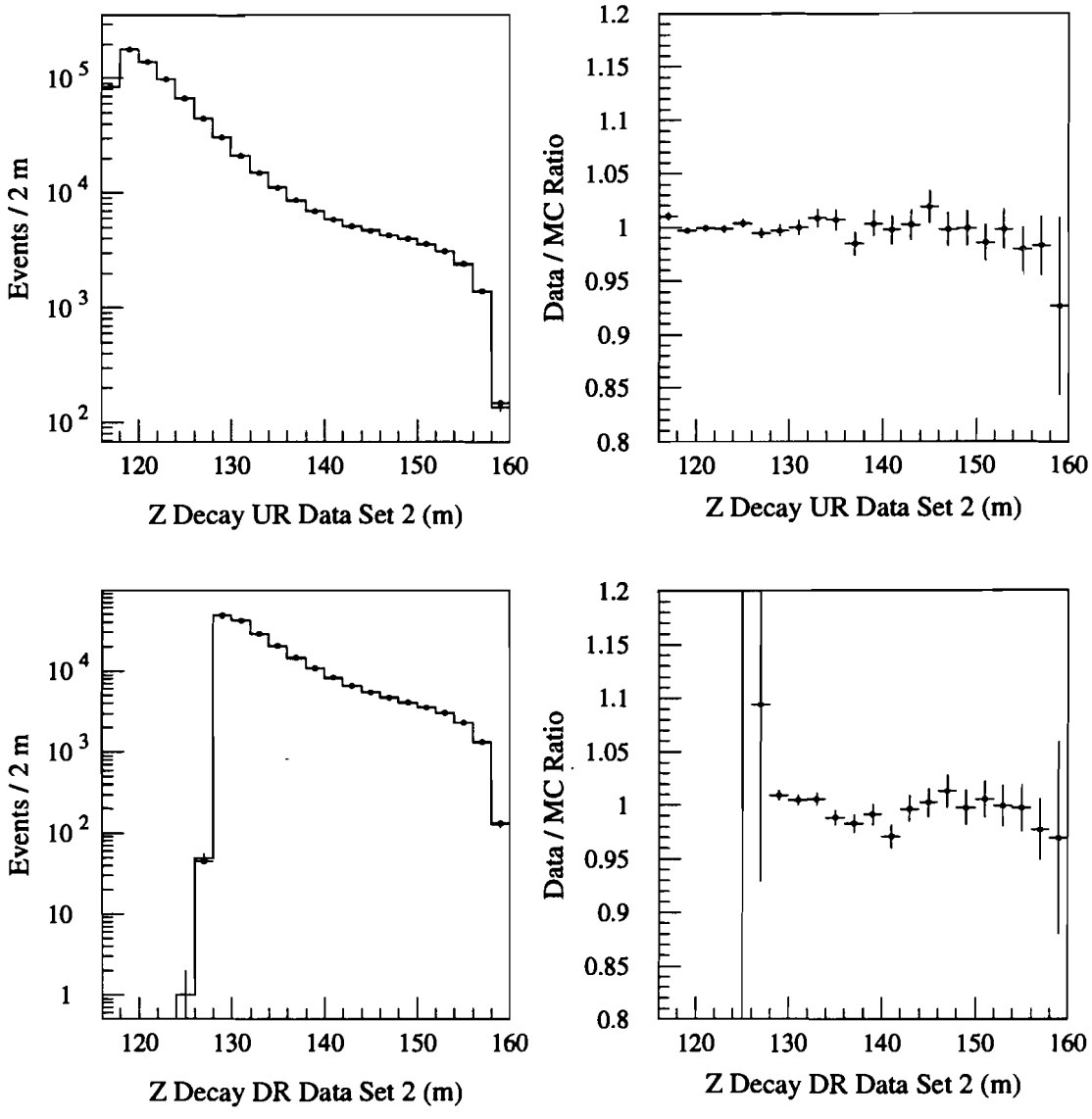

Figure 7.13: A comparison of the data and Monte-Carlo decay vertex distributions for $K \rightarrow \pi^+\pi^-$ decays from Data Set 2 (the second half of the run, without T&V hodoscopes). The histograms are data and the dots are Monte Carlo.

are a possible source of bias. Losses due to inefficiencies caused by out-of-time hits are very small, and are already included (neglecting correlations) in the wire efficiencies used in digitization. More problematic is a possible sensitivity of the tracking algorithm to the presence of extra hits. Since we are extracting only the shape of the decay rate, only p and z dependent biases need worry us.

The counter latches were combined via a logical OR; This was done before the first level trigger was checked. Since trigger elements in veto were already checked, only the B and C hodoscope latches were important. We verify the trigger using only the two reconstructed tracks during the analysis, so no significant effects are expected.

For the lead glass and other ADCs, the number of counts above pedestal in the accidental event were added to the generated event. This was done prior to the application of the relevant readout thresholds. The only portion relevant to the charged analysis is the pattern of energy deposit in the calorimeter, since the clusters are used to match the x and y tracks.

7.6 Summary

We have presented an outline of the Monte-Carlo simulation of our experiment. The simulated data agree well with the actual data collected, and this gives us confidence in our understanding of the detector.

Since the IB and DE components of the $K \to \pi^+\pi^-\gamma$ decay have different decay distributions, the IB being a mixture of K_S and K_L and the DE being

essentially pure K_L, the acceptance was calculated separately for each. The distributions (for the case of the UR beam, the second half of the run) are shown shown in figures 7.14 and 7.15. The average overall acceptance of our detector was 14.6% (9.2%) for IB (DE) decays.

The acceptance determined for $K \rightarrow \pi^+\pi^-$ decays in the UR beam for the second half of the run is shown in figure 7.16.

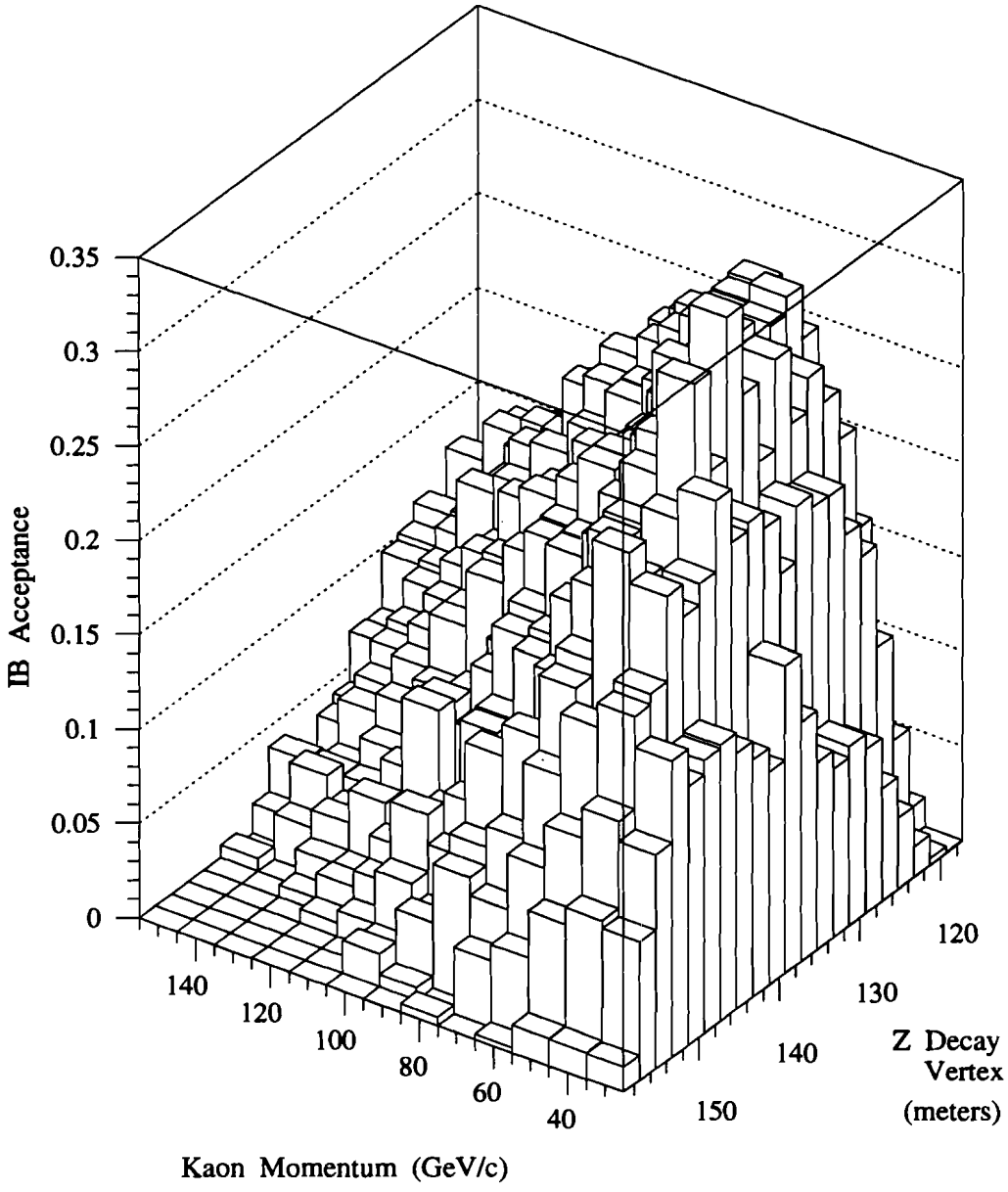

Figure 7.14: The acceptance for IB $K \to \pi^+\pi^-\gamma$ from the UR beam in Data Set 2.

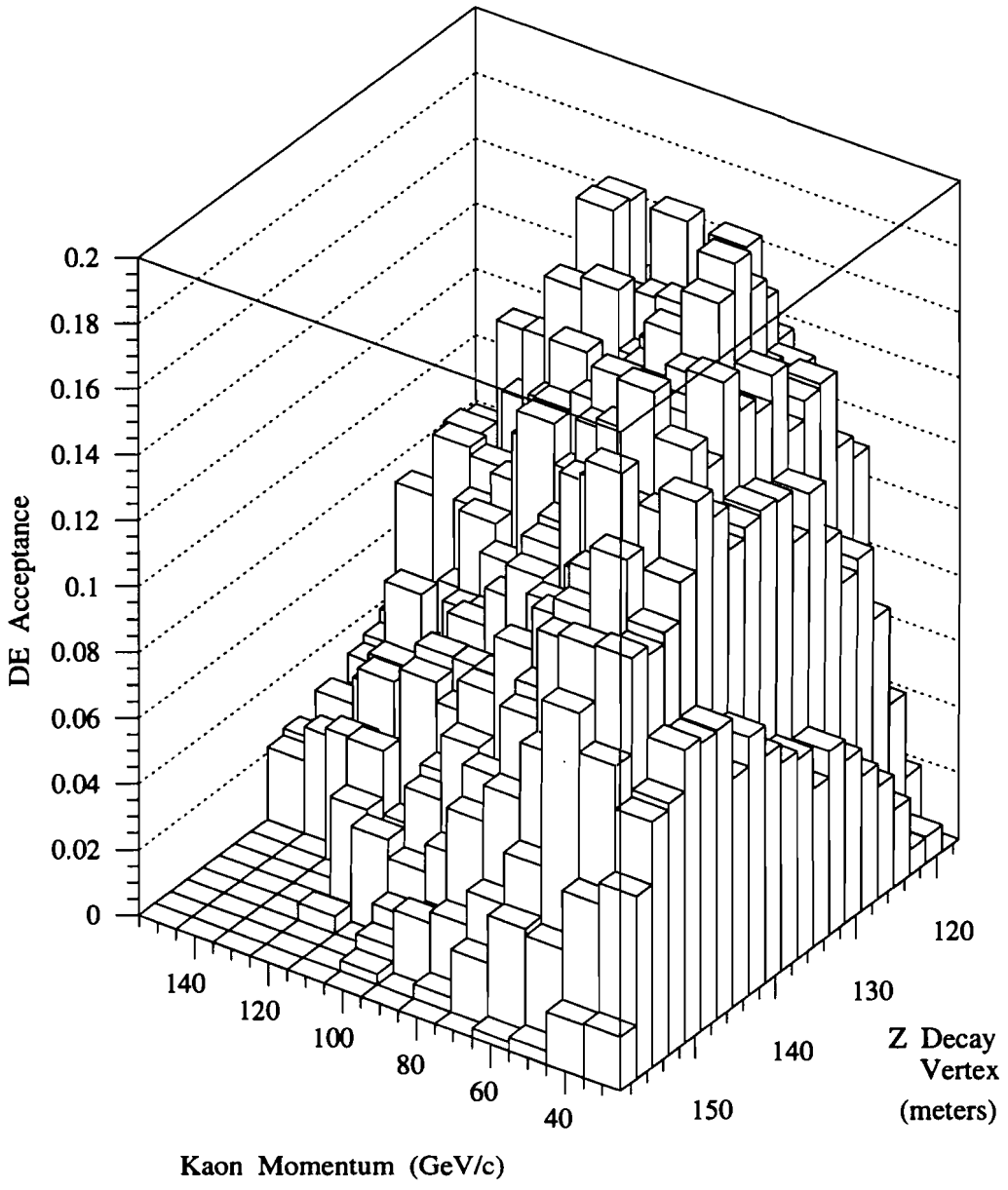

Figure 7.15: The acceptance for DE $K \rightarrow \pi^+\pi^-\gamma$ from the UR beam in Data Set 2.

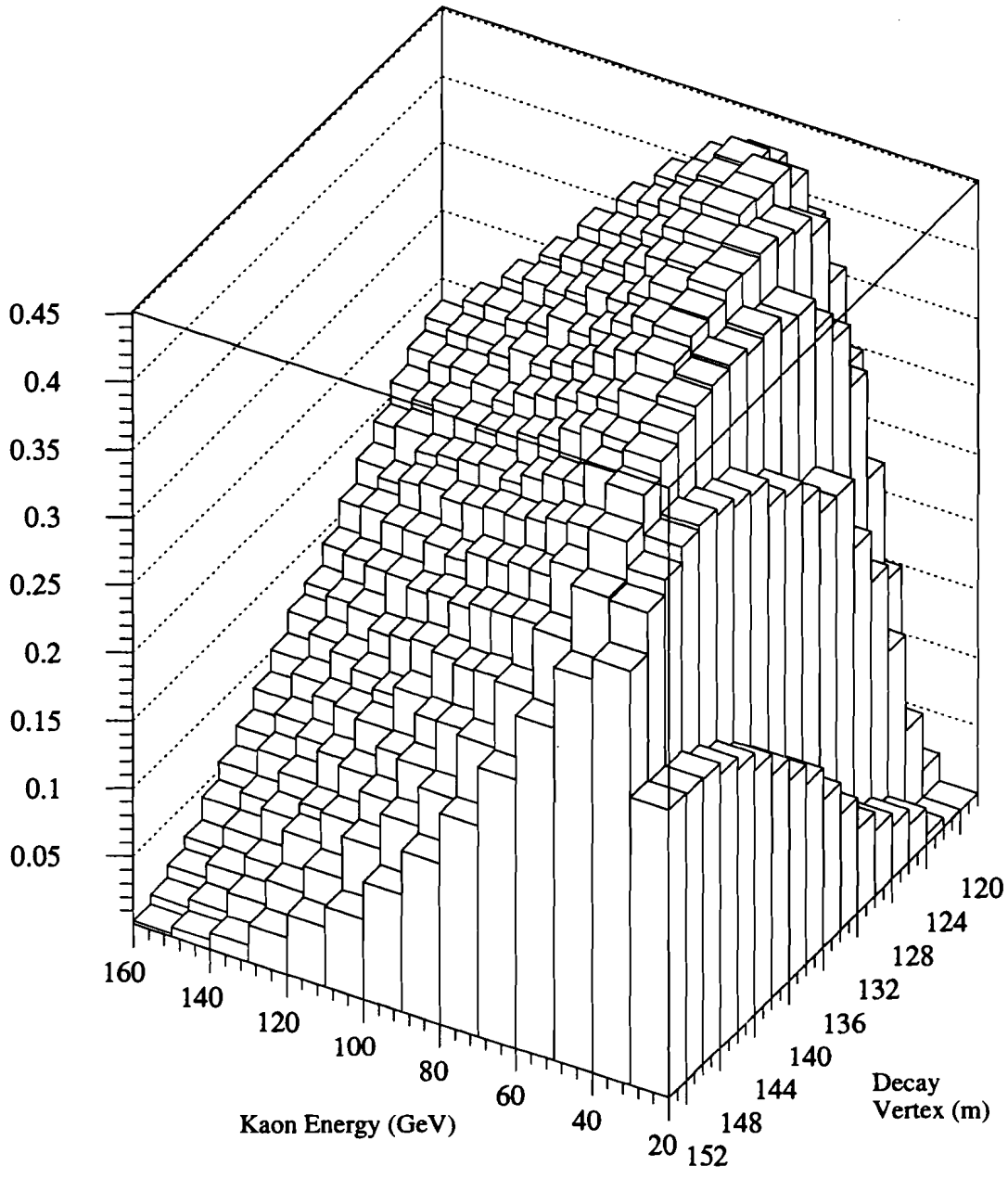

Figure 7.16: The acceptance for $K \rightarrow \pi^+\pi^-$ from the UR beam in Data Set 2.

Chapter 8

The Measurement

Before beginning fitting, we demonstrate the effect of interference between the K_L and K_S amplitudes by showing the proper time distributions of the data and the Monte Carlo simulation. The Monte Carlo events here were generated using $\eta_{+-\gamma} = \eta_{+-}$. Figure 8.1 shows the comparison between data and Monte Carlo from the UR for Data Set 2. The ratio plot, below the overlay, is relatively flat. This means that $\eta_{+-\gamma}$ is not very different from η_{+-}.

Figure 8.2 is the same data, but now the Monte Carlo has the interference term turned off. The Monte Carlo overlay no longer matches the data and the ratio plot, below, clearly shows a "wiggle". It is clear that interference is present in the data. The location of the "wiggle" in proper time provides information on ϕ_η, while the ratio of events at low/high proper time provides information on $|\eta|$.

As mentioned above, actual fitting of the data is not accomplished by fitting the proper time distribution, but by comparing the (p,z) distribution of the data to the prediction function. One of the four (p,z) distributions is shown in figure 8.3.

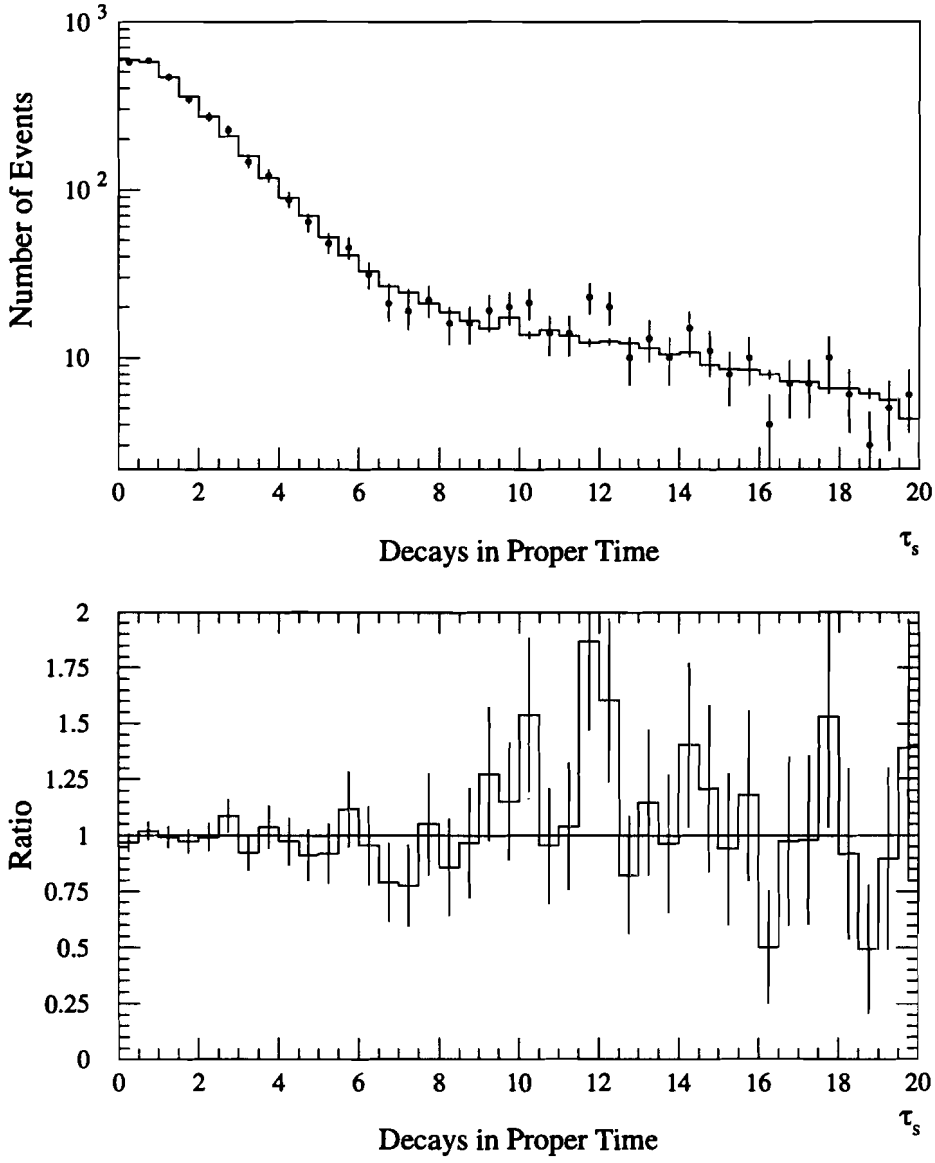

Figure 8.1: Data-Monte Carlo comparisons for $K \rightarrow \pi\pi\gamma$ of the number of decays as a function of proper time. The histogram represents the Monte Carlo, while the data is shown at points. Above, the data is overlayed with the Monte Carlo. Below, the ratio of the data and the Monte Carlo is shown. The data is the the UR and from the the second half of the run (Data Set 2). Neither the data, nor the Monte Carlo in these plots has been acceptance corrected or background subtracted.

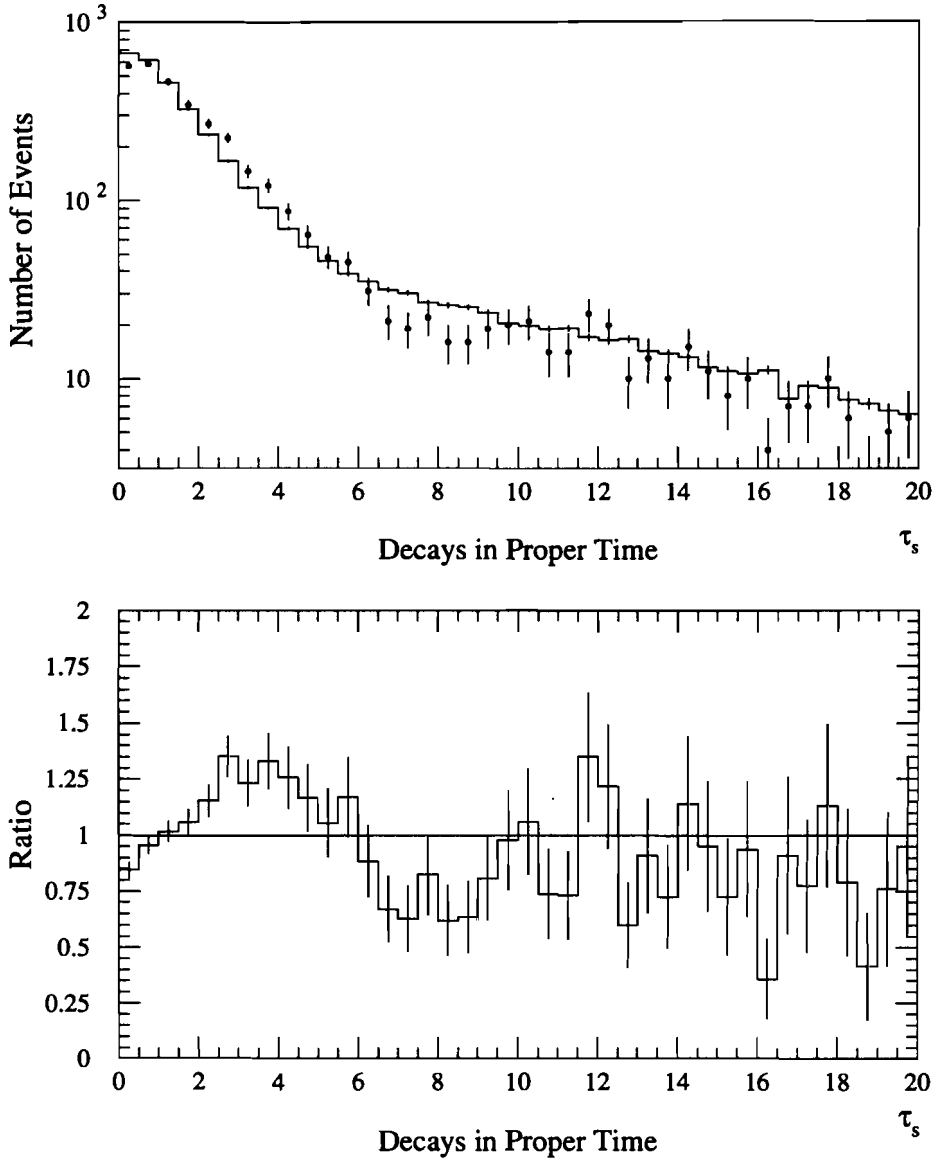

Figure 8.2: Data-Monte Carlo comparisons for $K \rightarrow \pi\pi\gamma$ of the number of decays as a function of proper time. The histogram represents the Monte Carlo, while the data is shown at points. Above, the data is overlayed with the Monte Carlo, now with its interference term turned off. Below, the ratio of the data and the Monte Carlo is shown. The data is the the UR and from the the second half of the run (Data Set 2). Neither the data, nor the Monte Carlo in these plots has been acceptance corrected or background subtracted.

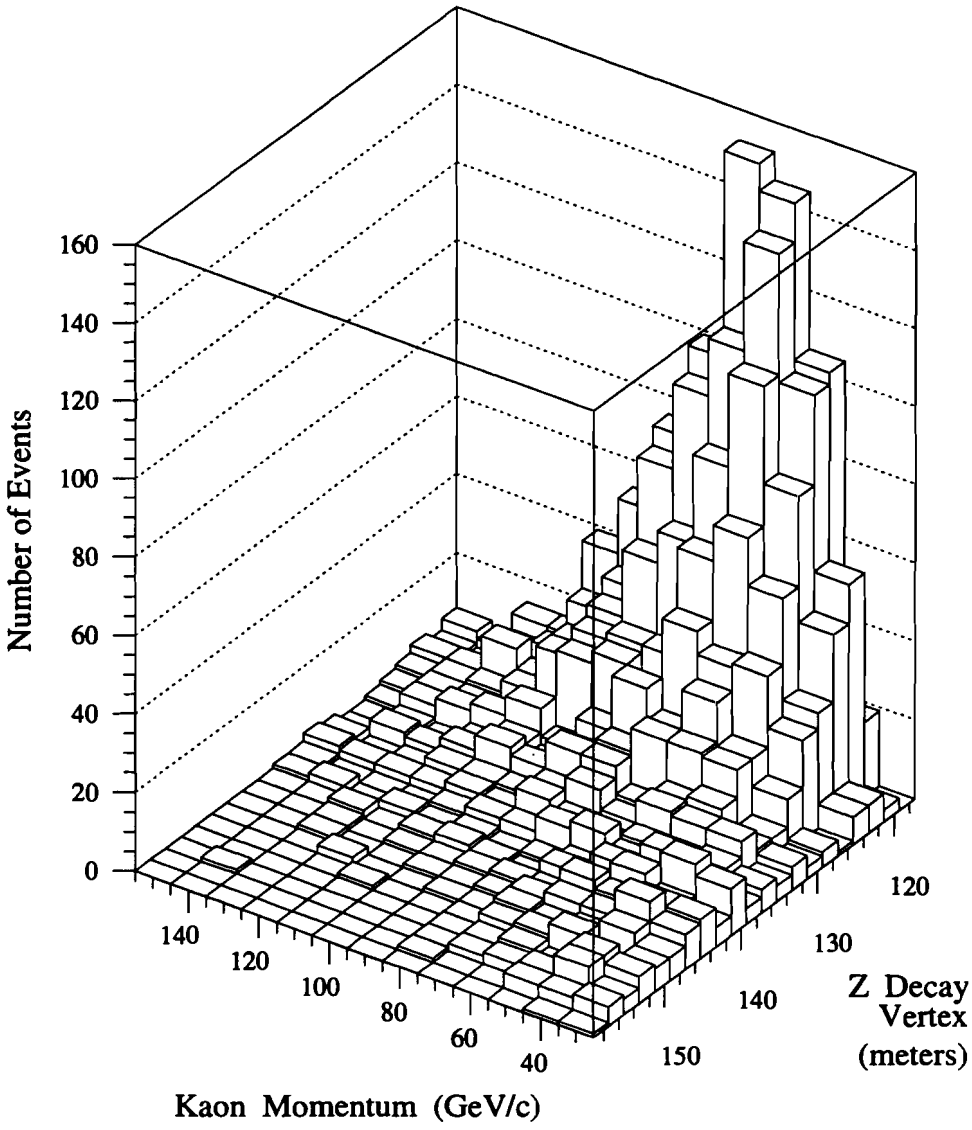

Figure 8.3: The (p,z) distribution of the $K \rightarrow \pi\pi\gamma$ data from the UR, second half of the run. The data in this plot has not been acceptance corrected or background subtracted.

8.1 Normalization to the $\pi^+\pi^-$ Data

The data was fit to the hypothesis of

$$D(p,z) = S(p) \cdot f(p,z) \cdot A(p,z), \tag{8.1}$$

where D is the data, S is the momentum spectrum of the K_S exiting the regenerator, f is the integral of the decay probability (equation 1.20) over the (p,z) bin, and A is the acceptance which was calculated via the Monte Carlo. The determination of f and A have already been described, therefore we turn our attention to $S(p)$.

The spectrum, $S(p)$, was determined from our $\pi^+\pi^-$ data. By using the data, both the shape of the spectrum as well as the absolute normalization (and thereby N_S) were determined. As previously detailed, the $\pi^+\pi^-$ events used the same trigger as the $\pi^+\pi^-\gamma$ data and were collected simultaneously. Also, the analysis of the $\pi^+\pi^-$ data used many of the same cuts as the $\pi^+\pi^-\gamma$ analysis.

Employing equation 8.1 in reverse:

$$S_{\pi\pi}(p) = \frac{\sum_z D_{\pi\pi}(p,z)}{\sum_z A_{\pi\pi}(p,z) \cdot f_{\pi\pi}(p,z)}. \tag{8.2}$$

[It was assumed that the beam incident on the regenerator was purely K_L. The Monte Carlo simulation of the experiment was used to determine the effect of primary (target) K_S decays. The maximum difference was a 3% effect in the low z, high p region where data occupancy is very low. For the UR No T&V data set, these (p,z) bins contain fewer than 10 events.] Fits to the $\pi^+\pi^-$ data were used to provide ϕ_{+-} and ρ. The phase of η_{+-},

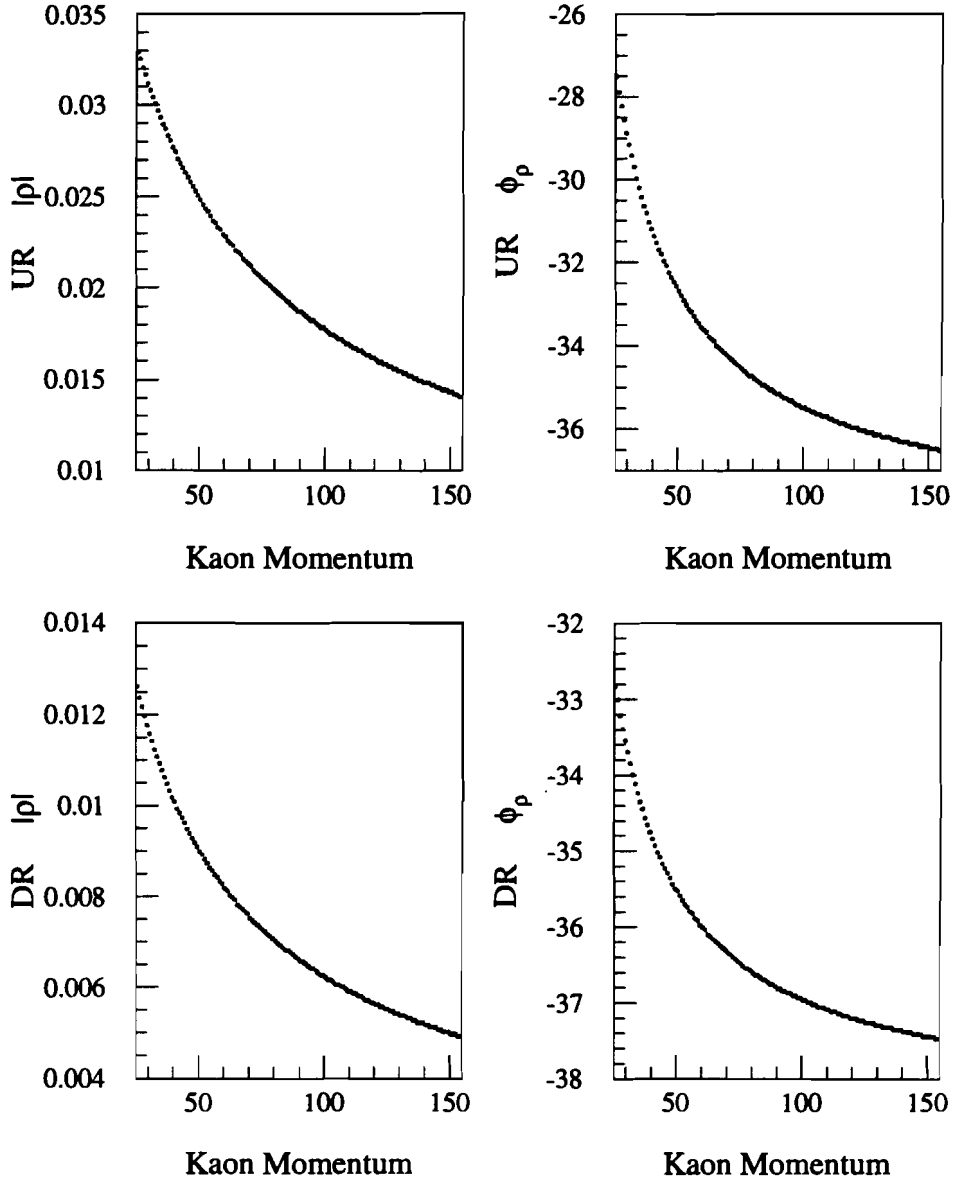

Figure 8.4: The magnitude and phase of regeneration as a function of kaon momentum. Here the kaon momentum is measured in GeV/c and the phase is measured in degrees.

ϕ_{+-}, was fixed at 43.53° ± 0.97°. [7] It was assumed that $\rho \propto (f - \bar{f})/k$ which follows a power law in kaon momentum. Using the $\pi^+\pi^-$ data to fit a single combined (Carbon + Hydrogen) power law for our regenerators ($CH_{1.1}$), it was determined that $|(f - \bar{f})/k| = 1.302 \pm 0.006$ mb at 70 GeV/c and it varies as $p^{-0.574 \pm 0.007}$ The resultant regeneration parameters for the UR and DR are shown in 8.4. [37] The value for Δm used was the combined E731/E773 value of 0.5282 $\times 10^{10} \hbar s^{-1}$. [7] The magnitudes of $|\eta_{+-}|$, B_{+-}, τ_L, and τ_S used were the PDG averages: [10]

$$
\begin{aligned}
|\eta_{+-}| &= (2.269 \pm 0.023) \times 10^{-3}, \\
B_{+-} &= (68.61 \pm 0.28)\%, \\
\tau_L &= (5.17 \pm 0.04) \times 10^{-8}\ s, \text{ and} \\
\tau_S &= (0.8926 \pm 0.0012) \times 10^{-10}\ s.
\end{aligned}
$$

One advantage to making a common choice of input variables (with the $\pi^+\pi^-$ analysis) is that it allows direct comparison to the measurement of ϕ_{+-} above.

As a test, the spectrum was calculated from the data as well as from the Monte Carlo. (See figure 8.5) The two curves differed slightly in shape, but gave similar results when used to fit the $\pi^+\pi^-\gamma$ data. The $\pi^+\pi^-$ data spectrum was used in the final fitting.

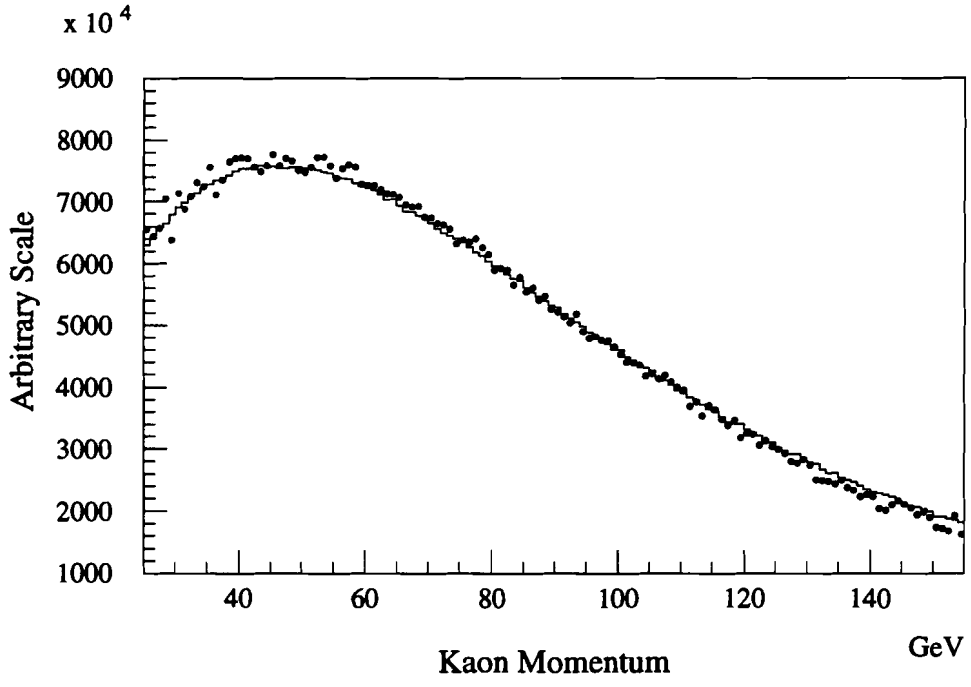

Figure 8.5: The spectrum of K_S exiting the regenerator. The points represent the spectrum of K_S exiting the regenerator as calculated using the $\pi^+\pi^-$ data (as detailed above). The histogram is the curve calculated when using the Monte Carlo events passing the analysis as the data.

8.2 Fitting the Data

With the spectrum in hand, the remaining constants required for fitting are the $K_S \rightarrow \pi^+\pi^-\gamma$ branching ratio, $B_{+-\gamma}$, and r the K_L DE to IB ratio. The least biased way to determine $B_{+-\gamma}$ is by fitting it along with $\eta_{+-\gamma}$ in comparison to the decay probability equation, however this weakens the rest of the fit by increasing the number of parameters fit for. The best previous measurement of $B_{+-\gamma}$ was made by E731. This measurement used all events

in the region downstream of their regenerator (a relatively short 17 m). The K_L DE component was subtracted as background and it was assumed that the K_L IB component was mirrored by the CP violating component in the $\pi^+\pi^-$ decay. The $\pi^+\pi^-\gamma$ branching ratio was then determined by scaling to the number of $\pi^+\pi^-$ decays. It was possible to follow the same procedure in E773, however there would have been only a modest increase in the number of events used (with the shortened z region) and those would have been divided into 4 data subsets. In the end, it was decided to rely on the E731 result. It was impossible for E773 to make a better determination of r than already existed since this measurement requires a pure K_L beam which E773 did not have. In the fit, the values for these were constrained by the E731 measurements, [19]

$$\begin{aligned} B_{+-\gamma} &= (4.87 \pm 0.11) \times 10^{-3} \text{ and} \\ r &= 2.175 \pm 0.16. \end{aligned}$$

Because they were constrained, not fixed, the quality of the fit decreased as they strayed from their measured values.

The data was fit by using the CERN program Minuit to compare the data to the prediction. Each of the four subsets was fit separately and checked for consistency before combining all of the data into one overall fit. The result of a maximum-likelihood fit to all four data sets is:

$$\begin{aligned} |\eta_{+-\gamma}| &= (2.359 \pm 0.062) \cdot 10^{-3}, \text{ and} \\ \phi_{+-\gamma} &= (43.8 \pm 3.5)^\circ. \end{aligned}$$

After the fit was performed a χ^2 was calculated using all data bins which contained more than 5 events. This fit had a χ^2 of 350 for 315 degrees of freedom.

As a consistency check, $|\eta_{+-\gamma}|$ and $\phi_{+-\gamma}$ were then fixed to their measured values. The DE/IB ratio, r, was again constrained to the E731 value. Refitting the data, the branching ratio was determined to be: $B_{+-\gamma} = (4.71 \pm 0.05_{stat}) \cdot 10^{-3}$.

To visually check the relative quality of the fit and to verify that the fit had not wandered into a false solution, the fit and the data were next cut into 10 GeV/c wide momentum slices. The z distributions of these slices were then overlayed and compared. Examples of some of these 52 slices are shown in figures 8.6 and 8.7.

8.3 Systematic Uncertainties

After fitting, the next task was determining the systematic uncertainties associated with the measurement. Many of the inputs to this fit came from the $\pi^+\pi^-$ analysis or from the PDG. Each of these parameters has an associated uncertainty which must be accounted for. In addition, estimates were made along the way in this analysis (such as the background volume and shape) and the effect of these uncertainties had to be assessed.

The systematic uncertainties were estimated by varying each of the elements of the analysis and observing the effect on the fit for $|\eta_{+-\gamma}|$ and $\phi_{+-\gamma}$.

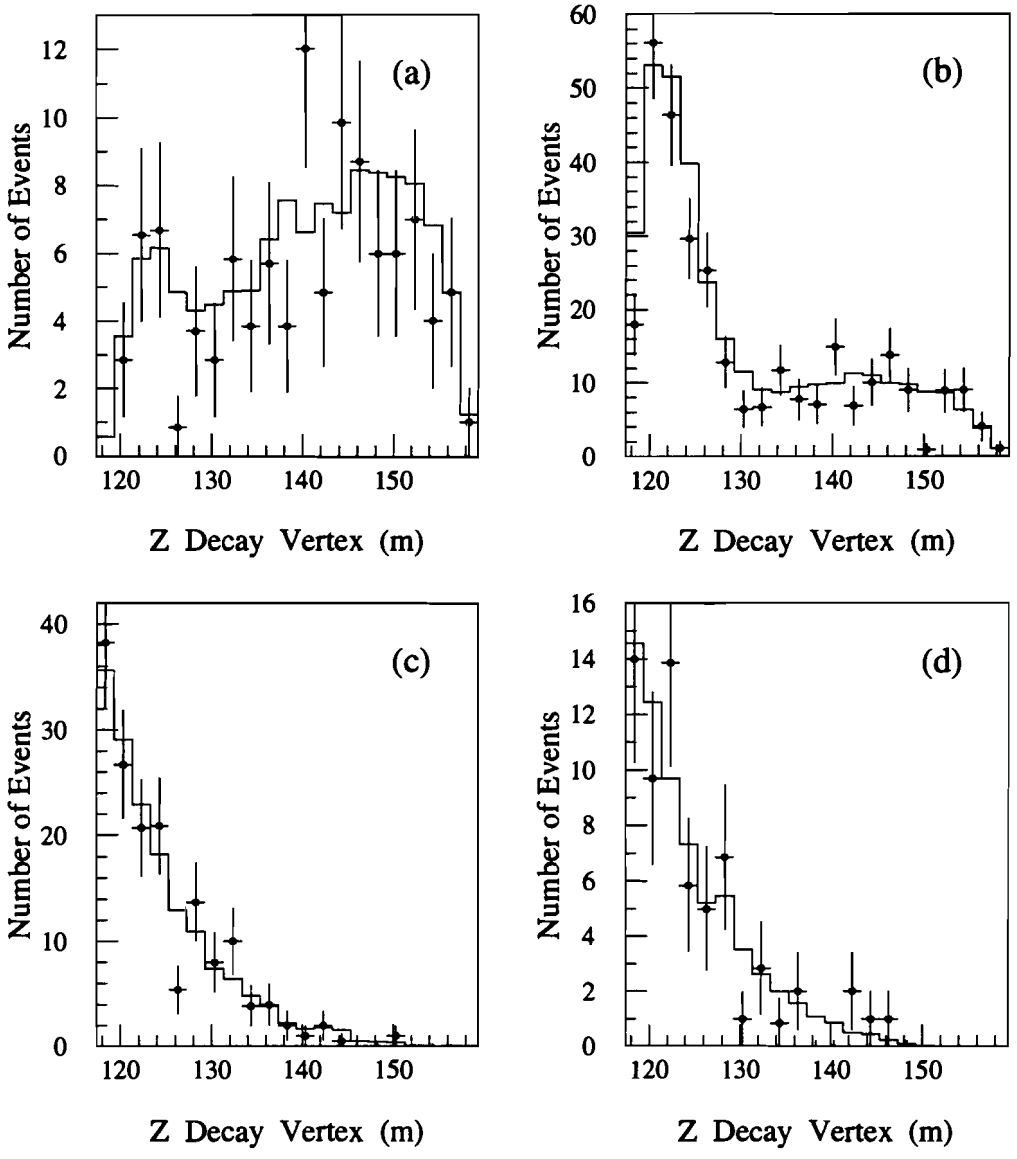

Figure 8.6: Fit-Data comparisons: Decay vertex distributions for momentum slices of the $K \rightarrow \pi\pi\gamma$ fit. The data is shown as the points, while the fit is the overlayed histogram. The data is from the UR, Data Set 2 (without T&V hodoscopes). The momentum slices are (a) $25 < p < 35$ GeV/c, (b) $35 < p < 45$ GeV/c, (c) $105 < p < 115$ GeV/c, and (d) $125 < p < 135$ GeV/c.

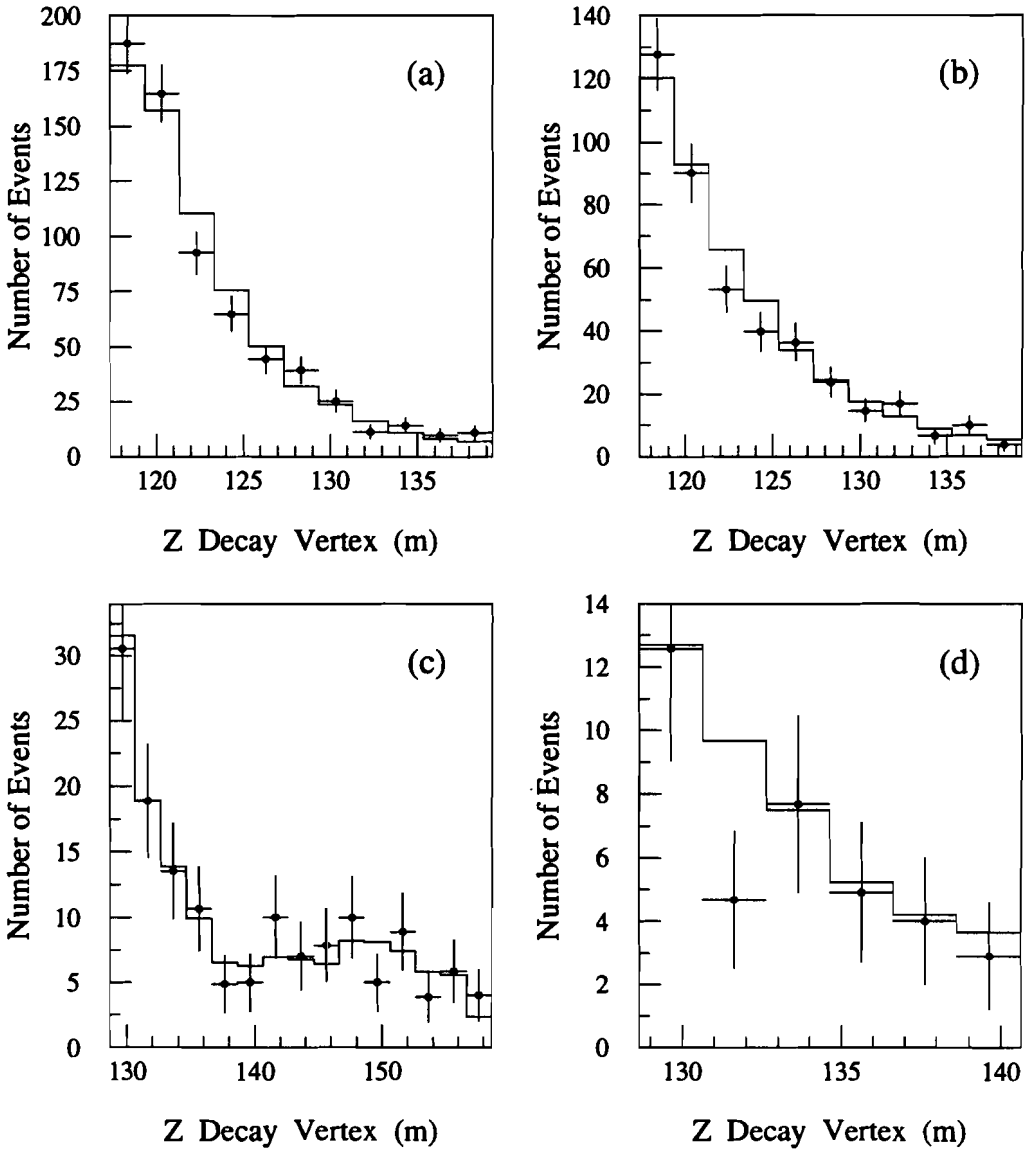

Figure 8.7: Fit-Data comparisons: Decay vertex distributions for momentum slices of the $K \rightarrow \pi\pi\gamma$ fit. The data is shown as the points, while the fit is the overlayed histogram. The momentum slices are (a) UR, Data Set 2, $55 < p < 65$ GeV/c, (b) UR, Data Set 1, $75 < p < 85$ GeV/c, (c) DR, Data Set 2, $25 < p < 35$ GeV/c, and (d) DR, Data Set 1, $85 < p < 95$ GeV/c.

To estimate the effect of the input parameters which were measured elsewhere, it was simply a matter of varying each by 1σ in its own uncertainty and refitting. The effect of the background shape was arrived at by using the (p,z) distribution of events from different locations in the $(M_{+-\gamma},P_T^2)$ plane for the background subtraction.

The uncertainty in normalization comes from several sources, including the differences in the analysis cuts on the data which were later corrected for. However, by far the largest uncertainty in the normalization was the result of not understanding the effects of accidental activity in the detector. Two sets of Monte Carlo events were generated for each the $\pi^+\pi^-$ and $\pi^+\pi^-\gamma$ simulations; one set with accidental activity overlayed and one set without. Each of these data sets was then put through the standard analysis and differences in the ratios of events were calculated to judge the effect of the accidentals.

The systematic uncertainties are listed in table 8.1. The largest contributions to the uncertainty in $|\eta_{+-\gamma}|$ are the result of the uncertainties in the background shape, flux normalization, and $|\eta_{+-}|$. The systematic uncertainty in $\phi_{+-\gamma}$ is dominated by the uncertainties in normalization, ρ (through α), and $|\eta_{+-}|$. All of contributions were added together in quadrature to come up with the final, total, estimate.

It should also be noted that r, the DE/IB ratio, and $B_{+-\gamma}$ are in the fit as constrained parameters. Thus, their uncertainties appear within the statistical uncertainties. With an eye towards future measurements, it is desirable to estimate their contribution to that uncertainty and therefore

Sources of Systematic Uncertainties			
Effect	Amount of Change	Uncertainty in $\lvert\eta_{+-\gamma}\rvert \times 10^3$	Uncertainty in $\phi_{+-\gamma}$ (degrees)
τ_S	0.19 %	0.001	0.19
Δm	0.7 %	0.001	0.39
ϕ_{+-}	2.2 %	0.005	0.43
$\lvert\eta_{+-}\rvert$	1.0 %	0.013	0.87
Power Law, α	2.5 %	0.001	0.92
Normalization	1.6 %	0.021	1.22
Background Volume	16 %	0.008	0.15
Background Shape		0.030	0.17
Data/MC mismatch in P	2×10^{-4}	0.002	0.54
Total		0.040	1.94

Table 8.1: Estimate of the Systematic Uncertainty

$B_{+-\gamma}$ and r Uncertainties			
Effect	Amount of Change	Uncertainty in $\lvert\eta_{+-\gamma}\rvert \times 10^3$	Uncertainty in $\phi_{+-\gamma}$ (degrees)
$B_{+-\gamma}$	2.3 %	0.030	1.76
r = DE/IB	6.0 %	0.050	0.48

Table 8.2: Estimate of the uncertainties associated with $B_{+-\gamma}$ and r.

the effect of knowing them to greater precision. To try to quantify these effects, $|\eta_{+-\gamma}|$ and $\phi_{+-\gamma}$ were first fit with r and $B_{+-\gamma}$ fixed. They were then refit after varying first r, then $B_{+-\gamma}$. The results of this study are in table 8.2.

Chapter 9

Conclusion

9.1 The Result

With the result in hand, it is interesting to compare it to the other relevant measurements. These are shown in table 9.1. This measurement has significantly smaller statistical and systematic uncertainties than the best previous measurement of $\eta_{+-\gamma}$ [5]. This is due to the present experiment having more events, a longer decay region (which better samples the range where the interference term is large), and using $\pi^+\pi^-$ decays for normalization. Further, this result is, within uncertainties, equal to η_{+-}, both in magnitude and phase. The comparisons are shown graphically in figure 9.1.

From the measurement of $\eta_{+-\gamma}$ it is possible to draw conclusions about direct CP violation in the $\pi^+\pi^-\gamma$ decay mode. Equation 1.19 gives:

$$\eta_{+-\gamma} = \epsilon + \epsilon'_{+-\gamma}, \tag{9.1}$$

relating ϵ which represents the CP violation that is due to mixing and $\epsilon'_{+-\gamma}$ which is any "extra" or direct CP violation. Using the fact that ϵ'_{+-} is very

Measurement Comparison			
$K \to \pi^+\pi^-\gamma$ (E773: This Measurement)	$\lvert\eta_{+-\gamma}\rvert$	=	$(2.359 \pm 0.062_{stat} \pm 0.040_{sys}) \cdot 10^{-3}$
	$\phi_{+-\gamma}$	=	$(43.8 \pm 3.5_{stat} \pm 1.9_{sys})^\circ$
$K \to \pi^+\pi^-\gamma$ (E731: Best Previous Measurement)	$\lvert\eta_{+-\gamma}\rvert$	=	$(2.15 \pm 0.26_{stat} \pm 0.20_{sys}) \cdot 10^{-3}$
	$\phi_{+-\gamma}$	=	$(72 \pm 23_{stat} \pm 17_{sys})^\circ$
$K \to \pi^+\pi^-$ (PDG and E773)	$\lvert\eta_{+-}\rvert$	=	$(2.269 \pm 0.023_{stat\ \&\ sys}) \cdot 10^{-3}$
	ϕ_{+-}	=	$(43.19 \pm 0.97_{stat\ \&\ sys})^\circ$

Table 9.1: Comparison of the $K \to \pi^+\pi^-\gamma$ and $\pi^+\pi^-$ measurements.

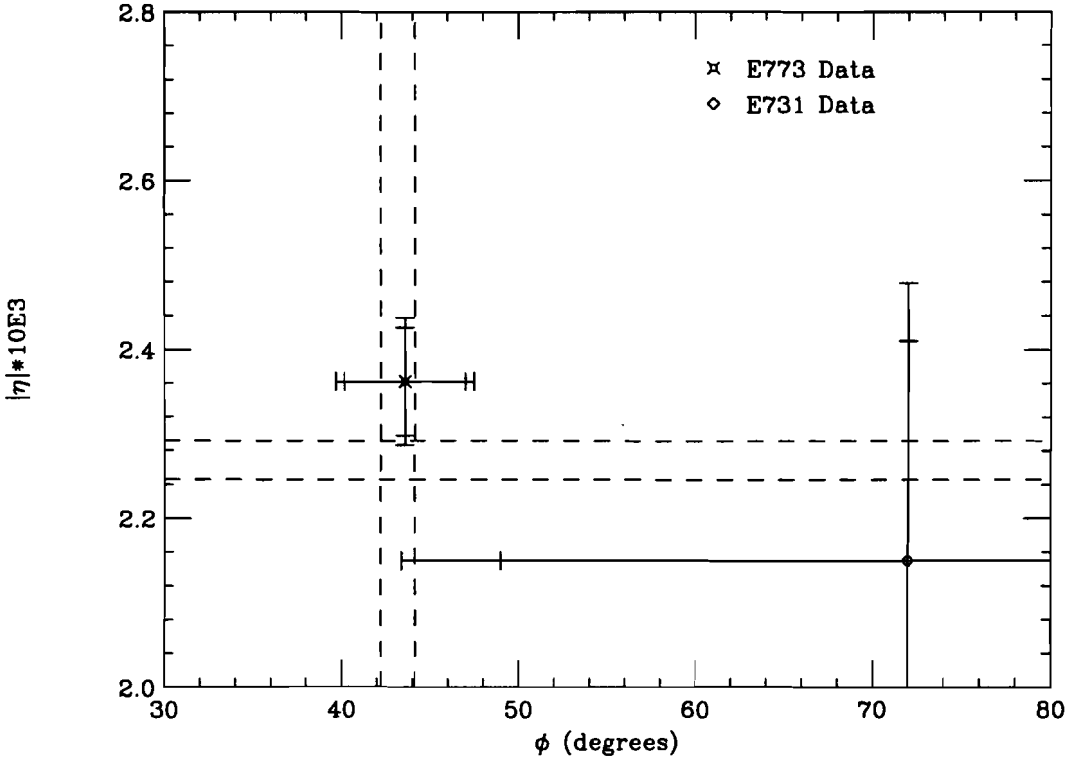

Figure 9.1: Comparison of the measurements of $|\eta|$ and ϕ. The two points with error bars show the E773 and E731 measurements of $\eta_{+-\gamma}$. The first tic mark on the error bars represents the statistical uncertainty only, while the second is the combined statistical and systematic uncertainty. The dashed lines mark the $\pm 1\sigma$ uncertainties on the measurement of η_{+-}.

small (E731 measured $\mathrm{Re}(\epsilon'_{+-}/\epsilon) = (7.4 \pm 5.6) \cdot 10^{-4}$ [6]), one can approximate:

$$\left|\frac{\epsilon'_{+-\gamma}}{\epsilon}\right| \approx \left|\frac{\eta_{+-\gamma} - \eta_{+-}}{\eta_{+-}}\right|. \tag{9.2}$$

This yields

$$\left|\epsilon'_{+-\gamma}/\epsilon\right| = 0.041 \pm 0.035 \tag{9.3}$$

for the E773 measurement of $\eta_{+-\gamma}$ and compares to

$$\left|\epsilon'_{+-\gamma}/\epsilon\right| = 0.49 \pm 0.48 \tag{9.4}$$

for the analogous E731 measurement. Note that the uncertainty of the current measurement is only a factor of 1.5 from the value of the rough estimate by Lin and Valencia. [26]

9.2 The Future

In the next generation experiment, KTeV, the $\mathrm{Re}(\epsilon'_{+-}/\epsilon)$ is expected to be measured to the level of one part in 10^4. To accomplish this, an increase of a factor of 50 in statistics is expected. The significant increase in the number of events will provide the opportunity to make big improvements in the various $K_{S(L)} \to \pi^+\pi^-\gamma$ branching ratios. In particular, a new measurement of $B_{+-\gamma}$, the K_S branching ratio would make a significant reduction in the "statistical uncertainty" attributed to that measurement as detailed in the last chapter. As previously mentioned, perhaps the least biased method of measuring this parameter is by fitting it concurrently with $\eta_{+-\gamma}$, however, an independent measurement might be made following the E731 method with

the additional constraint of using only events out to about $2.5\tau_S$. Since the sum of the interference approximately cancels out by that point, this would act to minimize the effect of interference with the K_L term(s) (See figure 8.2) and therefore reduce the possibility of introducing a bias. KTeV will also have a dedicated K_L beam which will enable it to make a large reduction in the uncertainties in r. These factors should combine to assure that the statistical uncertainties found in this analysis are reduced by perhaps a factor of 7.

The systematic uncertainties should be correspondingly reduced by the measures taken on behalf of the ϵ'_{+-} measurement. In particular, the addition of a flash ADC to the photomultipliers will greatly improve the time resolution of activity in the calorimeter. This will correspondingly reduce the uncertainty in the normalization due to accidental activity in the calorimeter. Also, perhaps a combined simultaneous $\eta_{+-\gamma}$, η_{+-} fit could be made in order to eliminate the double counting of common systematic uncertainties.

The combined improvements in KTeV will enable it to measure $\epsilon'_{+-\gamma}/\epsilon$ with uncertainties of about 0.4% which is the regime where, according to Lin and Valencia, one might observe direct CP violation. Also, as mentioned previously, with the current activity measurement of ϵ'_{+-} and $\epsilon'_{+-\gamma}$ there is hope that a more complete calculation of this effect will be carried out in the near future. [27] Thus, one expects significant improvement, on both the theoretical and experimental fronts, in our understanding of CP violation in the $K \to \pi^+\pi^-\gamma$ decay mode.

Other measurements which could be carried out in KTeV with the $K_L \to$

$\pi^+\pi^-\gamma$ decay include searching for higher order multipole contributions to the decay and measurement of the form factors of the decay. By plotting the angle between the photon and the pions in the center-of-mass it is possible to look for a charge asymmetry or higher order multipole contributions. These would be other signs of direct CP violation in the decay. Meanwhile, detailed analysis of the Dalitz plot should allow a determination of the form factors for this decay.

9.3 Summary

In summary, we have observed the interference between coherently regenerated K_S and transmitted K_L mesons decaying to the $\pi^+\pi^-\gamma$ final state. We collected 8,836 of these decays (with a background of 209 events) and fit their distribution in p and z to obtain precise values for the magnitude and phase of $\eta_{+-\gamma}$. Our result is consistent with the prediction that any direct CP-violating contribution to $\eta_{+-\gamma}$ must be very small. With the next run, the $\pi^+\pi^-\gamma$ decay mode will be in a very good position to begin testing the existing models of direct CP violation.

References

[1] J.H. Christenson, *et al.*, Phys. Rev. Lett. **13**, 138 (1964).

[2] L. Criegee, *et al.*, Phys. Rev. Lett. **17**, 150 (1966). J.-M. Gaillard, *et al.*, Phys. Rev. Lett. **18**, 20 (1967). and J.-M. Gaillard, *et al.*, Nuovo Cimento **59A**, 453 (1969).

[3] S. Bennett, *et al.*, Phys. Rev. Lett. **19**, 993 (1967).

[4] D. Dorfan, *et al.*, Phys. Rev. Lett. **19**, 987 (1967).

[5] E.J. Ramberg, *et al.*, Phys. Rev. Lett. **70**, 2529 (1993).

[6] L.K. Gibbons, *et al.*, Phys. Rev. Lett. **70**, 1199 (1993).

[7] B. Schwingenheuer, R.A. Briere, *et al.*, Phys. Rev. Lett. **74**, 4376(1995). See also B. Schwingenheuer, Ph.D. thesis, University of Chicago, 1995 (unpublished) and R.A. Briere, Ph.D. thesis, University of Chicago, 1995 (unpublished).

[8] T.T. Wu and C.N. Yang, Phys. Rev. Lett., **13**, 380 (1964).

[9] T.J. Devlin and J.D. Dickey, Rev. Mod. Phys., **51**, 237 (1979).

[10] Particle Data Group: L. Montanet, *et. al*, Phys. Rev. D: Review of Particle Properties, **50**, 1544 (1994).

[11] T.D. Lee and C.S. Wu, Ann. Rev. of Nucl. Sci., **16**, 511 (1964).

[12] V. Fitch, *et al.*, Phys. Rev. Lett., **15**, 73 (1965).

[13] V. Fitch, *et al.*, Phys. Rev., **164**, 1711 (1965).

[14] C. Alff-Steinberger, *et al.*, Phys. Lett., **21**, 595 (1966).

[15] R.A. Briere, Internal Memo

[16] A. Gsponer, *et al.*, Phys. Rev. Lett., **42**, 9 (1979).

[17] A. Gsponer, *et al.*, Phys. Rev. Lett., **42**, 13 (1979).

[18] H. Taureg, *et al.*, Phys. Lett., **B65**, 92 (1976).

[19] E.J. Ramberg, *et al.*, Phys. Rev. Lett., **70**, 2525 (1993).

[20] A.S. Carroll, *et al.*, Phys. Rev. Lett., **44**, 529 (1980).

[21] R. Rockmore and T.F. Wong, Phys. Rev. D **7**, 3425 (1973).

[22] C.S. Lai and B.L. Young, Nuovo Cimento **52A**, 83 (1967).

[23] Particle Data Group: M. Aguilar-Benitez, *et. al*, Particle Properties Data Booklet, 36 (1992).

[24] K. Kleinknecht, Ann. Rev. of Nucl. Sci., **26**, 1 (1976).

[25] V.L. Fitch, *et al.*, Phys. Rev. Lett., **15**, 73 (1965).

[26] Y.C.R. Lin and German Valencia, Phys. Rev. D, **37**, 143 (1988). See also Hai-Yang Chang, Phys. Lett. B, **315**, 170 (1993).

[27] German Valencia, Private Communication.

[28] J. Roehrig, *et al.*, Phys. Rev. Lett., **38**, 1116 (1977).

[29] D. Leurs, *et al.*, Phys. Rev., **133**, B1276 (1964).

[30] A.S. Carroll, *et al.*, Phys. Rev. Lett., **44**, 525 (1980).

[31] Particle Data Group: M. Aguilar-Benitez, *et. al*, Particle Properties Data Booklet, 116 (1992).

[32] J.F. Donoghue, B.R. Holstein, and G. Valencia Int. J. Mod. Phys. **A2**, 319 (1987).

[33] A.J. Malensek, Preprint FN-341, FN-341A (errata), FNAL, October 1981.

[34] J.R. Patterson, Ph.D. thesis (The University of Chicago, December, 1990).

[35] L.K. Gibbons, Ph.D. thesis (The University of Chicago, August, 1993).

[36] H.W. Atherton *et al.*, Preprint CERN 80:07, CERN, 1980.

[37] R.A. Briere, Private Communication

Vita

John N. Matthews

[redacted]

1983-85 Undergraduate Research Assistant, The University of Chicago, The Enrico Fermi Institute, High Energy Physics Group; Professor Henry J. Frisch.

1985 A.B. Physics, Math & Economics, The University of Chicago, Chicago, IL.

1985-87 Research Assistant, University of Wisconsin–Madison, Departmentof Physics, High Energy Physics Group; Professor Albert R. Erwin.

1987 M.S. Physics, University of Wisconsin, Madison, WI.

1987-88 Supervisor of Electronics Construction, University of Wisconsin–Madison, Department of Physics, Plasma Physics Group; Professor R.N. Dexter.

1988-90 Graduate Teaching Assistant, Department of Physics and Astronomy, Rutgers University.

1990-95 Graduate Research Assistant, Rutgers University, Department of Physics and Astronomy, High Energy Physics Group; Professor Gordon B. Thomson.

1993 K.S. McFarland *et al.*, A Measurement of the Branching Ratio of $\pi^0 \to e^+e^-$ Using Decays in Flight of $K_L \to \pi^0\pi^0\pi^0$, *Phys. Rev. Lett.* **71** 31, (1993).

1993 D.A. Harris *et al.*, A Limit on the Branching Ratio of $K_L \to \pi^0\mu^+\mu^-$, *Phys. Rev. Lett.* **71** 3914, (1993).

1993 D.A. Harris *et al.*, A Limit on the Branching Ratio of $K_L \rightarrow \pi^0 e^+ e^-$, *Phys. Rev. Lett.* **71** 3918, (1993).

1994 P. Gu *et al.*, Measurement of the Branching Ratio and a Study of the CP for the Leptonic Decay $K_L \rightarrow e^+ e^- e^+ e^-$, *Phys. Rev. Lett.* **72** 3000, (1994).

1994 P. Krolak *et al.*, A Limit on the Lepton-Family Number Violating Process $\pi^0 \rightarrow \mu^\pm e^\mp$, *Phys. Lett.* **B320** 407, (1994).

1994 M. Weaver *et al.*, A Limit on the Branching Ratio of $K_L \rightarrow \pi^0 \nu\bar{\nu}$, *Phys. Rev. Lett.* **72** 3758, (1994).

1994 D. Roberts *et al.*, Search for the Decay $K_L \rightarrow \pi^0\pi^0\gamma$, *Phys. Rev. D* **50**, 1874 (1994).

1994 E.J. Ramberg *et al.*, Polarization of Λ and $\bar{\Lambda}$ Produced by 800-GeV Protons, *Phys. Lett.* **B338** 403, (1994).

1994 T. Nakaya *et al.*, Measurement of the Branching Ratio of $K_L \rightarrow e^+ e^- \gamma\gamma$, *Phys. Rev. Lett.* **73** 2169, (1994).

1995 M. Spencer *et al.*, A Measurement of the Branching Ratio and Form Factors of $K_L \rightarrow \mu\mu\gamma$, *Phys. Rev. Lett.* **74** 3323, (1995).

1995 B. Schwingenheuer and R.A. Briere *et al.*, CPT Tests in the Neutral Kaon System, *Phys. Rev. Lett.* **74** 4376, (1995).

1995 J.N. Matthews *et al.*, Measurement of the CP Violation Parameter $\eta_{+-\gamma}$, *Phys. Rev. Lett.* **75**, 2803 (1995).

1996 Ph.D. Physics, Department of Physics and Astronomy, Rutgers, the State University of New Jersey, New Brunswick, NJ.
* Thesis Topic:
Measurement of the CP Violation Parameter $\eta_{+-\gamma}$.
Advisor: Professor Gordon B. Thomson